Energy Levels in Organic Semiconductors: Tuning and Doping

Ross Warren

Corpus Christi College

University of Oxford

A thesis submitted for the degree of

Doctor of Philosophy

Michaelmas 2019

Acknowledgments

Abstract

The energy level tuning effect, observed when mixing halogenated versions of similar molecules, has recently been identified as a new way to modify the bulk ionisation energy and electron affinity of an organic semiconducting thin film, and increase the open-circuit voltage in organic solar cells. In this thesis, the energy level tuning effect is extended to organic field-effect transistors (OFETs). A method for the fabricating ambipolar devices with balanced hole and electron transport is established. This is achieved by using blends of two host molecules, zinc phthalocyanine (ZnPc) and its eight-times fluorinated derivative (F_8ZnPc), with energy levels that shift based on mixing ratio. The semiconducting behaviour of the bottom-gate bottom-contact OFETs can be tuned continuously from unipolar p-type, through ambipolar, and finally to unipolar n-type. For the ambipolar devices, the optimum balance between the hole and electron mobilities is found for the blend of 1:1.5 weight ratio of ZnPc:F_8ZnPc with hole and electron mobilities of $(8.3 \pm 0.2) \times 10^{-7}\,\mathrm{cm^2V^{-1}s^{-1}}$ and $(5.5 \pm 0.1) \times 10^{-7}\,\mathrm{cm^2V^{-1}s^{-1}}$, respectively. An application of the ambipolar devices in a complementary-like voltage inverter circuit, with performance comparable to an inverter based on separate ZnPc and F_8ZnPc OFETs, is demonstrated.

Next, a p-dopant (F_6-TCNNQ) is introduced into the blend of ZnPc:F_8ZnPc to investigate the impact of the energy level tuning effect on the molecular doping process. The doping efficiency is investigated using photothermal deflection spectroscopy and electron paramagnetic resonance spectroscopy, and is found to depend upon host mixing ratio. The experimentally observed trend is explained with a statistical model that includes both shifts of the host's ionisation energies, and, importantly, the electron affinity of the dopant. The energy level shift in the model is in close agreement with the $0.86\,\mathrm{eV}$ shift in ionisation energy observed experimentally. As further validation, the model reproduces the measured trend at low temperature. The energy level tuning effect therefore has a crucial impact on the molecular doping process. The practice of comparing host and dopant energy levels must consider the long-range electrostatic shifts to consistently explain the doping mechanism in organic semiconductors.

Contents

iv

List of Figures

1.   Introduction

Organic semiconductors promise new applications for electronic devices. The low temperature deposition of organic molecules allows for the use of many substrates unavailable to most inorganic semiconductors, including flexible, lightweight, transparent and inexpensive materials. Furthermore, manufacturing processes such as roll-to-roll printing and vacuum coating, enable large-area deposition which can dramatically reduce the production cost per area. Organic semiconductors have achieved commercial success in organic light-emitting diode (OLED) displays used in smart phones, and are increasingly used in larger displays such as tablets and televisions. The first flexible products have entered the market. Other devices including organic solar cells, field-effect transistors, lasers, photodetectors and bioelectronic sensors, show favourable progress.

Organic electronic devices typically combine a number of organic semiconducting thin films between electrical contacts, for example, a basic organic solar cell as sketched in Figure 1.1a. These solar cells usually have at least three organic layers in a p-i-n-type structure: a hole transporting layer (HTL), an intrinsic photovoltaic layer, and an electron transporting layer (ETL). The ideal energy levels, according to Würfel [1], for this structure are drawn in Figure 1.1b. Ideally, light entering the cell only interacts with the photovoltaic layer, where free charge carriers, holes and electrons, are generated via absorption. The photogenerated charges then travel through highly conductive non-absorbing transport layers (the HTL and ETL) for extraction at the electrodes to an external circuit. Another example of an organic device is the organic field effect transistor (OFET), sketched in Figure 1.1c. An OFET can be thought of as a type of switch, where the current flow between the source and drain,

a

Contact

n | Electron transport layer

i | Photovoltaic layer

p | Hole transport layer

Transparent contact

Light

b

x

p | i | n

EA

IP

c

x

Contact | Contact

Semiconductor (SC)

Dielectric

Gate electrode
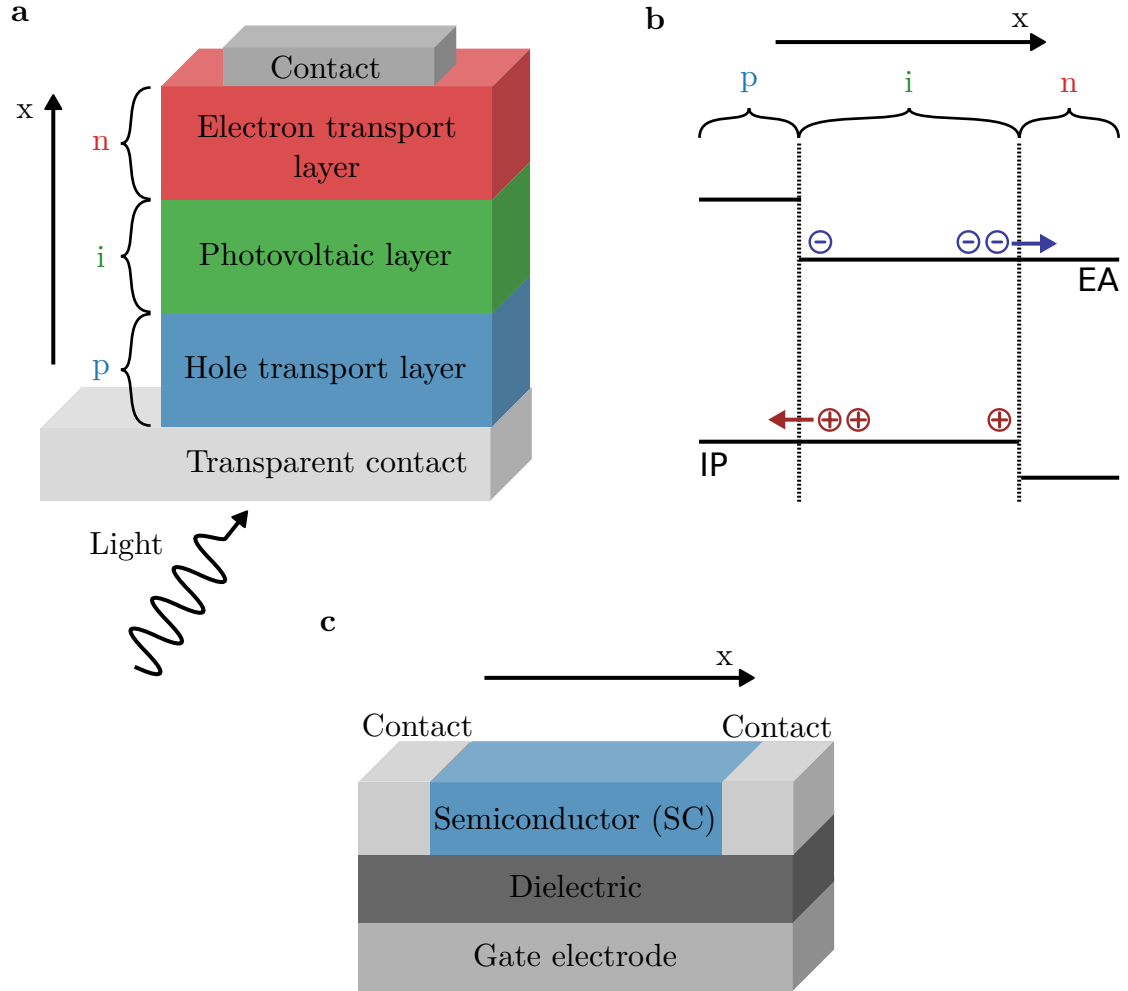
Figure 1.1: Organic device structures and corresponding ideal energy diagrams. (a) Typical *p-i-n* organic solar cell. The three layers are a hole transporting layer (HTL), a photovoltaic layer, and an electron transporting layer (ETL). **(b)** Energy level sketch for an ideal solar cell, independent of material system, according to Würfel [1]. **(c)** Drawing of a bottom-gate bottom-contact (organic) field-effect transistor.

in the x-direction, is modulated by the applied bias at the gate electrode.

In both these devices, efficient operation relies on the energy levels at the interfaces between layers in the stack. A mismatch between energy levels, intentional or otherwise, creates barriers for charge transport between the layers. For organic solar cells, these barriers should be minimised for the majority charge carrier (electrons in to the ETL and holes in to the HTL) passing from the active region to the contacts. At the same time, barriers are required to prevent the injection of minority carriers (holes in to the ETL, electrons in to the HTL), so that no energy is lost through charge recombination at the interface to and in the transport layers. Such semipermeable layers are achieved by selecting materials with suitable energy level offset, as sketched in figure Figure 1.1b. In a similar way for OFETs, the barrier height at the interface between the contacts and the semiconducting layer must be minimised for efficient device operation [2].

This thesis looks at two ways that have been used to manage energetic barriers in organic devices:

1. Energy level tuning

2. Molecular doping

Energy level tuning

For studying energy levels, the ionisation energy (IE) and electron affinity (EA), labelled in Figure 1.1b, are experimentally-accessible parameters closely associated with the transport levels of holes and electrons, respectively [3]. For example, the driving voltage of an OLED can be significantly reduced by selecting an HTL with an IE close to that of the work function of the transparent contact [4]. (In commercially available OLEDs, this method has largely been displaced by using doped transport layers, discussed in the next section.) Achieving good energy level alignment is not straightforward. The IE and EA of a layer depend not only on the constituent organic molecules, but also on the film's morphology [5]. Furthermore, in layers composed of mixtures of molecules, the IE and EA also vary with composition [6, 7].

Tuning IE and EA can be achieved by molecular modification, through means such as halogenation [8, 9]. This method however, is limited to discrete changes in energy. An alternative method to gradually shift the effective IE of a thin film involves the mixing of molecules with different IEs, and has been shown for a number of material systems, including zinc-phthalocyanine (ZnPc) and its fluorinated derivatives F_xZnPc, with $x = 4, 8, 16$ [6, 10, 11]. The tuning is enabled by a relatively long-ranged interaction, extending over a few neighbouring molecules along the π-π-stacking direction, mediated via the molecules' opposing quadrupole moments [12]. For example, the open-circuit voltage of an organic solar cell shifted monotonically to higher values with increasing F_4ZnPc content in the donor blend of ZnPc:F_4ZnPc [10]. Similar tuning effects have yet to be explored in other organic devices.

Molecular doping

Interface barriers can also be addressed via molecular doping. Molecular doping is the introduction of impurities into a semiconductor increasing its electrical conductivity over many orders of magnitude and shifting the Fermi Level towards the transport level. For solar cells [13], OLEDs [14, 15] and OFETs [16, 17], control of molecular doping has proven to be critical for both minimising Ohmic loss across devices, and improving carrier injection at metal-organic contacts [14, 16, 18]. In p-i-n-type organic solar cells, the transport layers make use of molecular doping [13]. Highly conductive transport layers allow for the absorbing layer to be freely positioned in the stack for optimal optical performance, with negligible Ohmic loss [19, 20]. Although doping is key for organic solar cell performance and has enabled the successful commercialisation of OLED displays, the fundamental principles governing efficient doping in organic semiconductors remain a topic of debate and the role of energy levels remains unclear.

1.1 Objectives

The aim of this thesis is to test the extent to which energy levels in molecular semiconductors can be considered tunable and investigate the effect in relation to molecular doping. With this in mind, there are two key objectives:

1. To explore how the energy level tuning effect can be implemented in new devices, here the OFET, and to enable new methods for engineering device performance.

2. To better understand the role of energy levels in the molecular doping process.

1.2 Contributions

This thesis will:

- Provide a brief summary on the physics of organic semiconductors, organic field-effect transistors, and the current understanding of molecular doping (Chapter 2).

- Describe the materials, experimental methods and simulations used here to characterise organic field-effect transistors and study doped organic semiconductors (Chapter 3).

- Explore the energy level tuning effect in OFETs, finding that by mixing ZnPc with F_8ZnPc, the charge transport in the OFETs can be tuned from p-type to ambipolar to n-type dependent on the composition blend (Chapter 4).

- Combine energy level tuning and molecular doping to find that the energy level tuning effect has a critical impact on the dopant's energy level and is therefore an important consideration for understanding the doping mechanism in organic semiconductors (Chapter 5).

- Summarise the main results and offer an outlook for future work (Chapter 6).

2. Background theory

This chapter introduces the physics of organic semiconductors, providing the basis for the discussions of the results in Chapter 4 and Chapter 5. In Section 2.1, semiconductors are introduced and the origin of semiconducting behaviour in organic molecules is reviewed, with particular attention given to understanding molecular orbital energies. Next, in Section 2.2, the current understanding of molecular doping is summarised. Finally, in Section 2.3, organic devices are discussed with a focus on metal-organic contacts and thin film transistors.

2.1 Molecular semiconductors

2.1.1 Introduction to semiconductors

Materials can be broadly categorised as metals, which conduct electricity well, insulators, which allow only very little electrical current to flow, or a third variant called semiconductors. The band structure (schematically shown in Figure 2.1) of semiconductors and insulators differ from metals in two aspects: firstly, there is a region in which no energy bands exist, called the band gap; and secondly, the Fermi level lies within this gap. At absolute zero (T=0 K), electrons fill the lowest available energy bands, with each state supporting two electrons, one spin up and one spin down, in accordance with the Pauli Exclusion Principle. The *Fermi level* is the energy at which the transition from the occupied to the unoccupied states occurs. If there is a state at the Fermi level, it will have an occupation probability of 0.5.

An electric current requires the flow of charge. As the Fermi level of a metal sits within a partially-filled energy band, electrons can move freely between many available states. This allows metals to conduct electricity, even at absolute zero. In
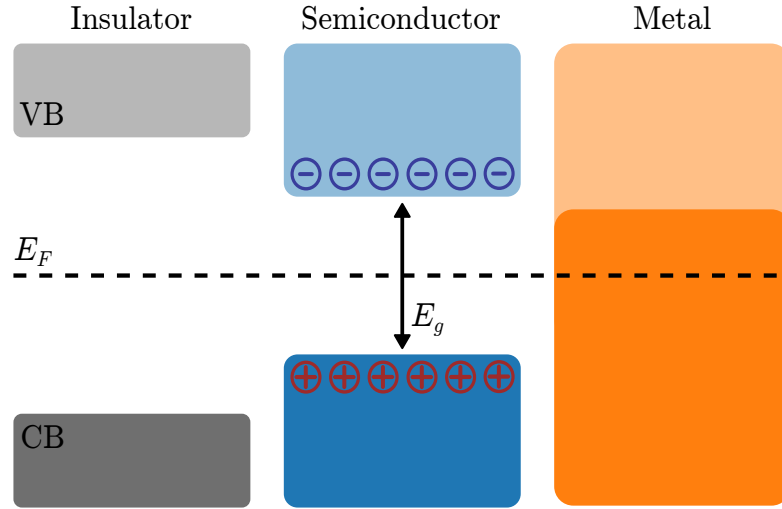
Figure 2.1: Insulators, semiconductors and metals. Energy level schematic showing the difference in band gap E_g between an insulator, semiconductor and a metal at $T = 0\,\mathrm{K}$. The regions of filled colour represent the electronic bands. For insulators and semiconductors, the Fermi level sits between the valence band (VB) and conduction band (CB), within the energy gap where no electron states exist. For a metal, the VB and CB overlap. There are many states around the Fermi level which can be accessed to readily carry a current.

contrast for semiconductors and insulators, the Fermi level is within the band gap. There are no available states and no free charge carriers. Therefore, at absolute zero, semiconductors and insulators have an infinite resistance.

As the temperature increases, some electrons will have enough thermal energy to jump across the band gap, from the occupied valence band to the empty conduction band, where they can then act as charge carriers. The excited electrons leave behind spaces in the valence band called holes, as shown for the semiconductor in Figure 2.1. As the negative charge of electrons is balanced by the positive charge of the nuclei, the absence of an electron creates a net positive charge at the hole's location. Therefore in response to an electric field, holes move in much the same way as electrons (apart from direction), acting as positive charge carriers in the valence band. Holes are relatively mobile, compared to other fixed positive charges like ionised n-type dopants for example, and thus can contribute to the electric current. Consequently for both semiconductors and insulators, the electrical conductivity increases with temperature.

This is in contrast to metals, where an increase in temperature generally leads to more scattering and therefore a decrease in conductivity.

The only difference between a semiconductor and an insulator is the size of the band gap. Generally, materials with large band gaps are insulators, whereas those with smaller band gaps, in the range of $1\,\text{eV}$ to $4\,\text{eV}$, are semiconductors. A clearer distinction can be made in terms of modifying the electrical conductivity of the material. There are several techniques which allow a semiconductor to behave as a conductor, for example:

- Heat it up such that charge carriers may be thermally excited across the band gap.

- Illuminate the semiconductor such that photons can excite charge carriers across the band gap.

- Dope the semiconductor with electrically active impurities.

- Gate the semiconductor with an external electric field.

Doping and gating both generate mobile carriers and cause a shift in the Fermi level. They are particularly important for transistors, a key component of modern electronics, and a focal point of this thesis.

2.1.2 Occupation statistics

As electrons are identical and indistinguishable particles with a half-integer spin, the probability that an electron will have energy E is given by the Fermi-Dirac distribution

$$f(E) = \frac{1}{e^{(E-E_F)/kT} + 1}, \tag{2.1}$$

where k is the Boltzmann constant and T is temperature. As illustrated in Figure 2.2, at $E << E_F$, the probability of a state being occupied is unity, whereas for $E >> E_F$, the probability is zero. The Fermi Level is defined as $f(E_F) = 0.5$, as marked by the grey dashed line. As the temperature increases, a greater number of electrons have
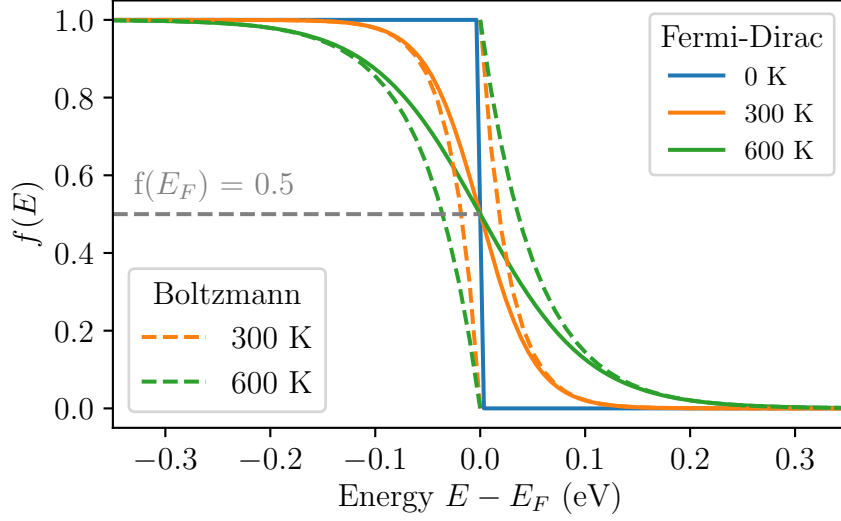
Figure 2.2: Fermi-Dirac occupation statistics for a range of temperatures. The occupation probability at the Fermi Level $f(E_F) = 0.5$ is marked as the grey dashed line. The Boltzmann approximation is also plotted for the higher temperatures.

the thermal energy to occupy higher energy states. Consequently, the Fermi-Dirac distribution is broadened around the transition at E_F with higher temperatures. For $E - E_F > 3kT$, Fermi-Dirac statistics can be well approximated using a Boltzmann distribution, as shown in Figure 2.2. Semiconductors satisfying this condition are called *non-degenerate*.

In thermal equilibrium, the density of free charge carriers in the conduction band n is related to the density of available states $g_c(E)$ and the probability that each of these states is occupied $f(E)$, integrated over all energies in the band:

$$n = \int_{E_c}^{\infty} g_c(E)f(E)\, dE, \tag{2.2}$$

where E_c is the energy of the conduction band. The density of states (DOS) is obtained by solving the time-independent Schrödinger equation. With periodic boundary conditions such that the particle acts as a free electron with constant effective mass m_e^*,

$$E(\mathbf{k}) = \frac{\hbar k^2}{2m_e^*}, \tag{2.3}$$

where $\mathbf{k}$ is any position independent vector, the DOS in the conduction band for an

electron in a uniform potential is

$$g_c(E)\, dE = 4\pi\left(\frac{2m_e^*}{h^2}\right)^{3/2}\sqrt{E - E_c}\, dE. \tag{2.4}$$

Similarly for free holes in the valence band, the number density is:

$$p = \int_{-\infty}^{E_v} g_v(E)[1 - f(E)]\, dE, \tag{2.5}$$

where the valence band energy is E_v. The DOS for holes in the valence band is given by:

$$g_v(E)\, dE = 4\pi\left(\frac{2m_h^*}{h^2}\right)^{3/2}\sqrt{E_v - E}\, dE, \tag{2.6}$$

where m_h^* is the effective mass of holes.

Figure 2.3 illustrates the quantities needed to calculate the density of charge carriers in a semiconductor. The DOS for the conduction and valence bands, the Fermi-Dirac distribution function and the electron and hole densities per unit energy are marked on the figure. The shaded area under the number densities per unit energy, $n(E)$ and $p(E)$, represent the thermal equilibrium carrier densities. From Figure 2.3, it is apparent that an increase in the Fermi Level will cause an increase in the electron density, and a corresponding decrease in hole density.

Analytical solutions to the carrier density integrals, Equation (2.2) and Equation (2.5), exist for non-degenerate semiconductors, where the Fermi-Dirac distribution can be replaced with a Maxwell-Boltzmann distribution (a single exponential). The approximate electron density becomes

$$n = N_c\, e^{-(E_c - E_F)/kT}, \tag{2.7}$$

where $N_c = 2(2\pi m_e^* kT/h^2)^{3/2}$ is the effective density of states for the conduction band. Similarly for holes, the hole density integral can be approximated as

$$p = N_v\, e^{-(E_F - E_v)/kT}, \tag{2.8}$$

where $N_v = 2(2\pi m_h^* kT/h^2)^{3/2}$ is the effective density of states for the valence band.

For a semiconductor in the dark which does not contain any impurities (an intrinsic semiconductor), free holes and electrons only arise from the thermal activation across
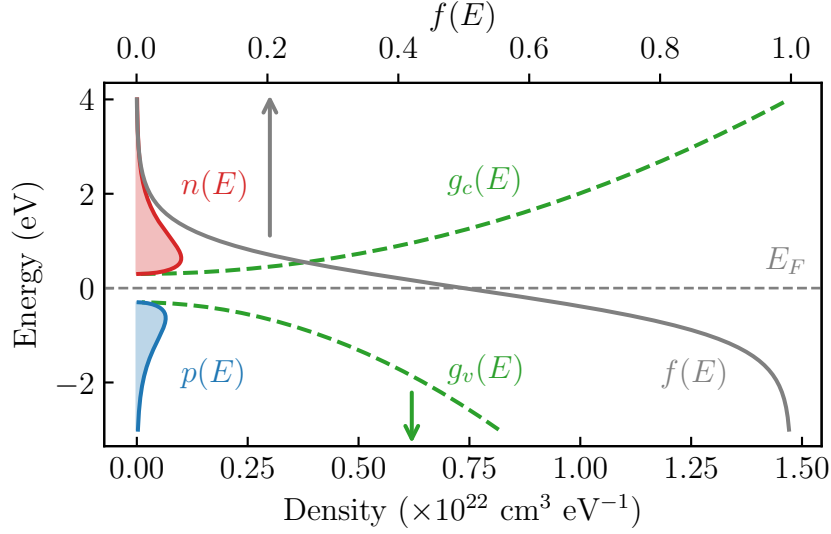
Figure 2.3: Charge carrier densities in the conduction and valence of a semiconductor. The electron $n(E)$ and hole $p(E)$ density per unit energy are marked in red and blue, respectively, with the shaded area under each representing the total density. The corresponding DOS are shown as green dashed lines for the conduction $g_c(E)$ and valence band $g_v(E)$. The occupation probability $f(E)$ and the Fermi Level E_F are marked in grey. The parameters used are: $E_F = 0 \, eV$, $E_c = 0.3 \, eV$, $E_v = -0.3 \, eV$, $T = 6000 \, K$, $m_e^* = 1.08 \, m_e$ and $m_h^* = 0.81 \, m_e$.

the band gap. As holes are generated by the vacancies left when an electron is promoted to the conduction band, their densities are equal

$$np = N_c N_v \, e^{-E_g/kT} = n_i^2. \tag{2.9}$$

For the semiconductors in this thesis with $E_g \approx 2 \, \text{eV}$ and $N_C = N_V = 1.7 \times 10^{21} \, \text{cm}^{-3}$ [21], the intrinsic charge carrier density at room temperature is very low $n_i \approx 10^5$ cm^{-3}. As the conductivity is proportional to the number of charge carriers, intrinsic semiconductors are often poor electrical conductors at room temperature. However, both the Fermi level position and the number density of charge carriers can be altered by the introduction of dopants, which is discussed in Section 2.2.

2.1.3 Organic molecules as semiconductors

Organic semiconductors are so-called as they are materials based primarily on carbon and hydrogen (with a few other heteroatoms such as nitrogen, oxygen and fluorine),

and show properties associated with semiconducting behaviour [22]. They are commonly classified as *small molecules* or *polymers*, broadly distinguished by molecular size and associated processing methods. Polymers are large chain-like molecules containing many repeating single units (monomers), and are typically deposited from solution using techniques such as printing or coating [23, 24]. Small molecules, which form the focus of this thesis, are compounds with relatively lower molar mass, typically $< 1000 \, \mathrm{g/mol}$. Generally, they have greater thermal stability than polymers, allowing for deposition by thermal evaporation in a vacuum. Because of well-defined molecular structures and high levels of material purity, small molecules are well-suited for fundamental studies of the electronic processes in organic semiconductors.

Molecular orbitals

In quantum mechanics, the spatial and energetic properties of electrons bound by the electric field of a nucleus, are considered as discrete energy levels or atomic orbitals. When atoms form molecules, these energy levels mix (or hybridise) to create molecular orbitals. The energy eigenstates and eigenvalues of these molecular orbitals are given by the Schrödinger equation, which, for a complex many-particle system cannot be analytically solved. Instead, the energy eigenstates are approximated, for example, by using a linear combination of the single-atom orbitals (LCAO method) or by density functional theory (DFT).

As organic semiconductors are carbon-based, understanding the electronic states of carbon is particularly important. Carbon has six electrons, which in the ground state configuration reside in the atomic orbitals: $1\,\mathrm{s}^2\,2\,\mathrm{s}^2\,2\,\mathrm{p}_x{}^1\,2\,\mathrm{p}_y{}^1$. To achieve full occupation of the $2\,\mathrm{p}_x$ and $2\,\mathrm{p}_y$ atomic orbitals, carbon could share two electrons with a bonding partner to form a lower-energy molecular bond - a covalent bond. However, carbon forms four covalent bonds as the binding energy gained by doing so, exceeds the energy required to promote an electron from the $2\,\mathrm{s}$ orbital to the empty $2\,\mathrm{p}_z$ state. Consequently, when atoms (e.g. hydrogen) bind with a carbon, the $2\,\mathrm{s}$ and $2\,\mathrm{p}$ orbitals hybridise. As depicted in Figure 2.4, this hybridisation can occur in one of three ways:

Hybridised state
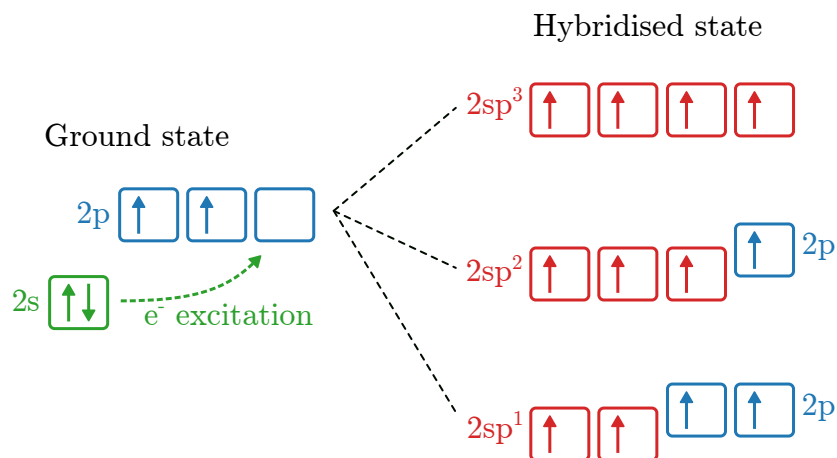
Ground state

Figure 2.4: Molecular orbital hybridisation in carbon. Sketched on the left hand side is the ground state electronic configuration of carbon ($1\,$s orbital not drawn). Prior to hybridisation, an electron is promoted from the $2\,$s orbital to the empty $2\,$p state. On the right hand side, the orbitals hybridise to form the sp^1, sp^2 or sp^3 configurations.

- sp^3-hybridisation - all four orbitals mix to create four equal orbitals that point toward the corners of a tetrahedron with an angle of 109.5° (e.g. ethane).

- sp^2-hybridisation - the $2\,$s orbital mixes with the $2\,p_x$ and $2\,p_y$ orbital to create three sp^2 orbitals and leave a remaining $2\,p_z$ orbital. The three sp^2 orbitals lie in the xy-plane with 120° between them. The $2\,p_z$ orbital is orthogonal to the sp^2 bonds (e.g. ethene).

- sp^1-hybridisation - the $2\,$s orbital mixes with a single $2\,$p orbital to form two hybridised sp^1 states at an angle of 180° to one another (e.g. acetylene).

Sp^2-hybridisation underpins the semiconducting behaviour of organic molecules via π-orbital electrons. The sp^2 orbitals of each carbon atom form three strong bonds localised in the plane of the carbon atoms, called σ-bonds. Above and below the plane of the sigma bonds, the $2\,p_z$ orbital pairs with neighbouring $2\,p_z$ orbitals to form relatively weaker π-bonds, in which the π-electrons can delocalise over many atoms. In the LCAO approach, the atomic orbitals either constructively interfere
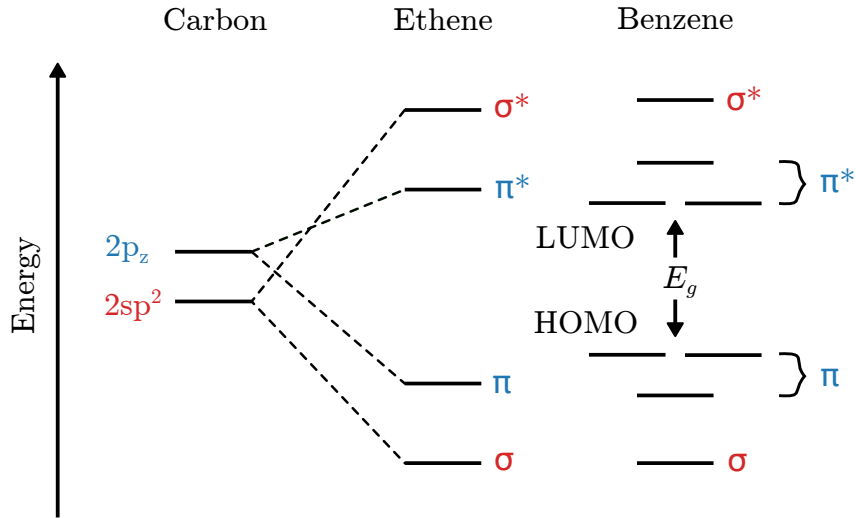
Figure 2.5: Hybridised orbitals in ethene and benzene. Schematic energy level diagram (not to scale) illustrating the splitting of σ and π bonds from the $2\,sp^2$ and $2\,p_z$ orbitals of atomic carbon. The $2\,p_z$ orbitals split into n orbitals, where n is the number of carbon atoms ($2\,sp^2$ splitting not shown for benzene). The highest occupied molecular orbital (HOMO) and lowest unoccupied molecular orbital (LUMO) are marked along with the energy gap E_g. Only the frontier orbitals involved in the carbon-carbon interaction are shown.

with one another, creating *bonding* orbitals, or destructively interfere to create *anti-bonding* orbitals (denoted with a star, e.g. π^*). Figure 2.5 shows the bonding and anti-bonding orbitals for ethene and benzene. The $2\,p_z$ orbitals split into n orbitals, where n is the number of carbon atoms in the molecule. For benzene, with six carbons, this results in three bonding and three anti-bonding π orbitals, with the π-electrons delocalised over the entire ring. In larger molecules, the delocalisation of the π-electrons can extend over many atoms, resulting in high carrier mobilities (e.g. graphene).

Analogously to conventional semiconductors, the molecular energy levels fill according the the Pauli Exclusion Principle, with the *highest occupied molecular orbital* (HOMO) and the *lowest unoccupied molecular orbital* (LUMO) acting as the effective valence band and the conduction band, respectively [25]. The HOMO and LUMO are separated by an energy gap E_g, resulting in an energy level picture similar to that of an inorganic semiconductor. Note, the term band gap is replaced with energy gap

because transport in organic semiconductors does not usually occur through bands, as will be discussed in Section 2.1.5. The energy gap partly depends on the size of the conjugated system and the extent to which the π-electrons delocalise across the molecule. For example, going from benzene to pentacene the energy gap reduces with each additional fused benzene ring [26]. Typically, the energy gap of organic semiconductors is in the range of $1.5\,\mathrm{eV}$ to $3\,\mathrm{eV}$, which means that very few charge carriers have enough thermal energy to cross the energy gap at room temperature. Hence, the conductivity of organic semiconductors primarily depends on injecting charge carriers from external sources, for example, by photo-generation (Section 2.1.6) or doping (Section 2.2) .

IE/EA of a single molecule

The frontier orbitals (the HOMO and LUMO) play a critical role in determining the electronic and optical properties of the semiconductor and are particularly important for the doping process. For a single molecule in isolation, the energy of the HOMO level can be considered equivalent to the vertical *ionisation energy* (IE). That is the energy required to remove an electron and place it at rest, in a vacuum, and infinitely far away from the molecule. Similarly, the *electron affinity* (EA) of a molecule is defined as the energy gained by adding an electron, and is equal to the LUMO level of the molecule [3, 27].

The energy gap between the IE and EA defines the *fundamental gap* and can be measured experimentally for single molecules via a combination of gas-phase ultraviolet photoelectron spectroscopy (UPS) and electron attachment spectroscopy [3]. From a computational standpoint, the fundamental gap is estimated by comparing the difference in ground state energy between the system with N and $N+1$ electrons for EA, and N and $N-1$ electrons for IE [28].

Although often used interchangeably in organic semiconductor literature, there is an important difference between ionisation potential and ionisation energy. In the most simple terms, the ionisation energy is the ionisation potential plus some additional energy that is required to escape the potential from the sample (e.g. the

potential caused by a surface dipole in a thin film). As UPS measurements are referenced in this thesis, only the term ionisation energy (IE) is used. Furthermore, in this thesis, both the EA and IE are defined positively. Therefore, an increase of EA or IE signifies more tightly bound molecular orbitals (a decrease in absolute energy). To avoid confusion, the terms HOMO and LUMO are only used when referring to the energy levels of single molecules in isolation. IE and EA are reserved for discussing thin films, the topic of the next section.

2.1.4 Single molecules to thin films

While the IE and EA are well-defined values for a single or gas-phase molecule, environmental interactions in solid phase make measurements and calculations of such parameters dependent on technique and on molecular organisation of the film. For example, the IE of pentacene was found to be $1.7\,\mathrm{eV}$ smaller in solid phase as compared to gas phase [29]. Furthermore, variations in solid state IE have been reported to exceed $0.6\,\mathrm{eV}$ for films of the same compound but with different molecular orientation (e.g. edge-on vs face-on the substrate) [5, 30]. These findings point towards the role of intermolecular interactions [31, 32].

Figure 2.6 depicts the energy level shifts going from a single molecule (HOMO and LUMO) to a molecular solid (IE and EA). The induction of the surrounding molecules (U_{ind}) act to stabilise the energy levels, with the IE decreasing and the EA increasing. In contrast, the electrostatic interactions arising from permanent charge distributions in the environment (U_{el}) lead to shifts in the IE and EA, with equal magnitude and in the same direction [12, 33, 34]. Altogether, the difference in energy levels can be approximated by the *electrostatic correction* for holes Δ^+ and electrons Δ^-:

$$\Delta^+ = IE - E_{HOMO} = \ -U_{ind} + U_{el} \tag{2.10}$$

$$\Delta^- = EA - E_{LUMO} = \ U_{ind} + U_{el}. \tag{2.11}$$
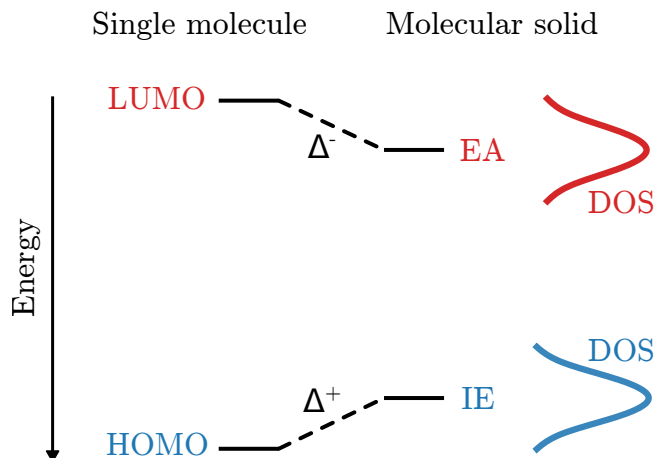
Figure 2.6: Schematic of the energy level shifts from single molecules to solids. The electrostatic correction (Δ^+ and Δ^-), which includes the induction and electrostatic interactions, stabilises the energy levels in a molecular solid with respect to the single molecule values. On the right hand side, a Gaussian approximation for the density of states (DOS) of a molecular solid is sketched.

Induction contributions

When any molecule is placed in a uniform, static electric field, electric multipoles may be induced by distortion of its charge distribution. Following the derivations in reference [31], the induction energy of two identical neutral molecules is dominated by the dipole-permanent dipole interaction, which, when at sufficiently high temperature and averaged over all orientations, is given by

$$\langle U_{ind} \rangle_{\mu\mu} = -\frac{2\alpha\mu^2}{(4\pi\epsilon_0)^2 r^6},\tag{2.12}$$

where α is the static polarisability and μ is the dipole moments of both molecules. The interaction produces an attractive force, stabilising the molecular energy levels, and is inversely proportional to the sixth power of the intermolecular separation r. As organic molecules have large clouds of delocalised π-electrons contributing to the static polarisability, the effect of induction can be significant. Differences between gas-phase IE and thin film IE are typically around $1\,\text{eV}$ to $2\,\text{eV}$ [29]. It should be noted that Equation (2.12) represents only the leading term in a more complicated

expansion. For a more complete treatment that includes higher-order multipoles and more complex charge distributions, the reader is directed to reference [31].

For the case of polar molecules (that is any molecule with a permanent non-zero multipole moment above the monopole), this induction contribution is simultaneously present with an electrostatic contribution.

Permanent electrostatic contributions

Permanent electrostatic interactions arise between molecules with different electric charges (e.g. anion-cation, charge-dipole, dipole-dipole, charge-quadrupole, etc.). Unlike the induction contribution, this permanent interaction takes place with no rearrangement of the electron distribution on either molecule. Again following the derivations in reference [31], the (long-range) electrostatic energy for two molecules with the geometry of Figure 2.7 is

$$
\begin{aligned}
(4\pi\epsilon_0)U_{el} =& \frac{Q'Q}{r} + \frac{1}{r^2}\{Q'\mu\cos\theta_1 - Q\mu'\cos\theta_2\} \\
&+ \frac{\mu\mu'}{r^3}\{2\cos\theta_1\cos\theta_2 - \sin\theta_1\sin\theta_2\cos\phi\} \\
&+ \frac{1}{2r^3}\{Q\Theta'(3\cos^2\theta_2 - 1) + Q'\Theta(3\cos^2\theta_1 - 1)\} \\
&+ ...,
\end{aligned}
\tag{2.13}
$$

where the total charge distribution for the first molecule is written $Q = Q_1 + Q_2$, the dipole moment is $\mu = Q_2 z_2 - Q_1 z_1$, and the quadrupole moment is $\Theta = Q_2 z_2^2 + Q_1 z_1^2$. The same definitions apply for the second molecule, but with a prime on all the variables.

Each term in Equation (2.13) corresponds to the interactions between various multipole moments of the charge distributions (only shown up to the charge-quadrupole interaction). If we consider the interaction between neutral molecules ($Q = Q' = 0$), the monopole interaction (1st term) and charge-dipole (2nd term) are zero, and the leading term becomes the dipole-dipole interaction (3rd term). However, many organic molecules with strong dipole moments tend to stack in a co-planar orientation with alternating dipole alignment [35, 36]. Considering antiparallel alignment of the charge distributions ($\phi = 180°$), and perpendicular orientation to OP ($\theta_1 = \theta_2 =$
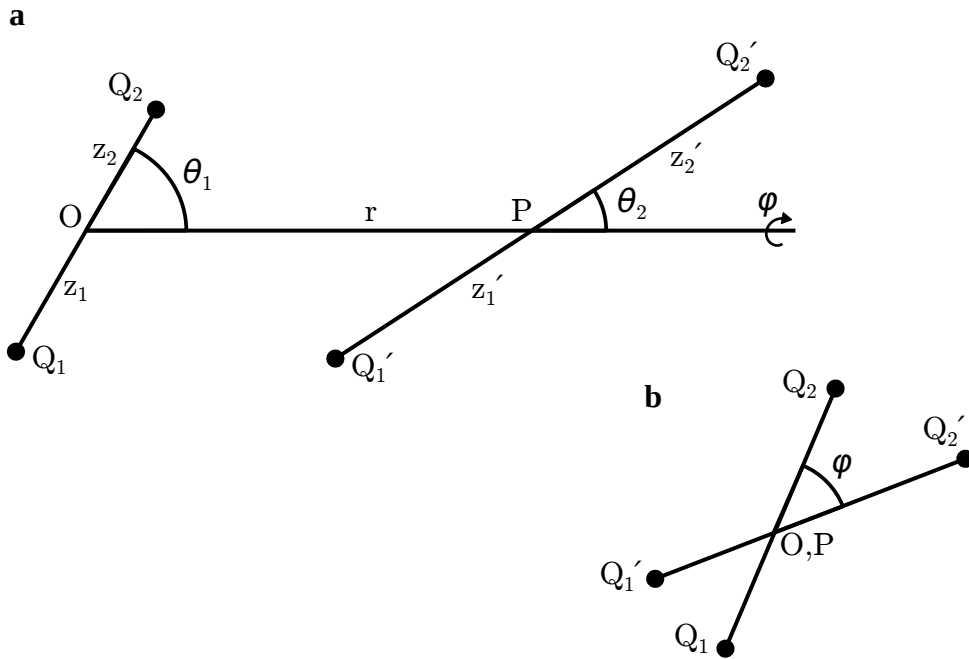
Figure 2.7: Geometry of two interacting molecules with linear charge distributions. (a) The first molecule has a charge distribution Q_1Q_2 and centre of mass O. The second molecule is has charge distribution $Q_1'Q_2'$, and its centre of mass P is separated from O by distance r. The first charge distribution makes an angle of θ_1 with the line OP, and the second charge distribution makes an angle of θ_2 with the same line. **(b)** The view along OP. The relative twist of the two linear distributions make an angle ϕ. Figure adapted from reference [31].

90°), the dipole-dipole term is also zero, and the charge-quadrupole interaction becomes the leading term. The effect of the charge-quadrupole interaction falls of as $1/r^3$, meaning that this interaction only extends to the nearest neighbours. Even so, theoretical calculations of charge-quadrupole energies are of the order of hundreds of meV [37], and can lead to strong shifts of thin film energies measured experimentally [33] and in devices [35].

Recent studies have shown that the charge-quadrupole interaction is a crucial parameter effecting organic device performance, in particular the open-circuit voltage in organic solar cells [10]. In blends of zinc-phthalocyanine (ZnPc) and its fluorinated derivatives (F_xZnPc), shifts in the IE as a function of molecular orientation and the mixing ratio in the ZnPc:F_xZnPc blend, were found to be proportional to the component of the quadrupole moment in the π-π stacking direction [12]. These findings were applied to organic solar cells to tune the charge-transfer state at the donor-acceptor interface, optimising the dissociation barrier for charge generation. As charge carriers recombine via charge-transfer states at the donor-acceptor interface, the open-circuit voltage is directly influenced by the energy of the charge-transfer state [38]. Therefore, the tuning of the charge-transfer state by ZnPc:F_xZnPc mixing ratio enabled shifts in the open-circuit voltage. Although these studies have highlighted the importance of quadrupole moments in solar cells, the energy level tuning effect has yet to be examined in other organic devices.

Dispersion contributions

There is a final intermolecular interaction arising from the continuous motion of charge density in molecules. At any instant a molecule can posses a temporary dipole, which fluctuates as the charge density oscillates. This temporary dipole induces a dipole on a neighbouring molecule, resulting in an attractive energy called the dispersion energy. The dipole-dipole dispersion energy is the first term in the mulitpole expansion, and is inversely proportional to the sixth power of the intermolecular separation.

Energetic disorder

The energy shift that molecules experience, due to the interactions with the environment, strongly depend on the distance and mutual orientation of the molecules in the solid. In a disordered solid, these parameters are randomly distributed, producing energy shifts which are also randomly distributed. The central limit theorem states that the sum of a group of random independent variables tends towards a normal distribution, even if the variables do not follow a normal distribution themselves. Therefore, the resulting spread of energy values, called the density of states (DOS), can be described with a Gaussian function centred around the mean value E_0:

$$g(E) = \frac{1}{\sqrt{2\pi}\sigma} \exp\left(-\frac{(E - E_0)^2}{2\sigma^2}\right), \tag{2.14}$$

where σ is the standard deviation of the distribution and is often referred to as the *disorder parameter*. Energetic disorder not only arises from intermolecular effects but also from on-site variations. Changes in conjugation length, configuration, conformation and the presence of chemical defects, all contribute to greater disorder in the DOS [39–41].

2.1.5 Charge transport

Highly crystalline organic semiconductors can achieve coherent band-like transport with charge carrier mobilities that decrease with increasing temperature, similar to inorganic semiconductors [42, 43]. However, in most organic semiconductors under device relevant conditions, transport is rate-limited by intermolecular charge transfer between weakly coupled electronic states, via thermally activated *hops*. Charge carriers are strongly localised due to the molecular reconfiguration of bond lengths and bond angles. Therefore, a charge making a hop is accompanied by a lattice distortion, which is collectively termed a *polaron*.

Marcus theory for electron transfer

One important model that can be used to describe hopping transport in molecular solids is *Marcus theory*, originally proposed to describe oxidation reactions between
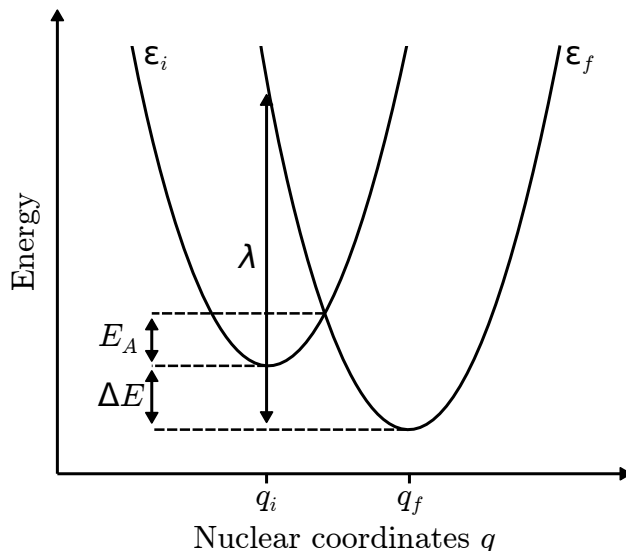
Figure 2.8: Illustration of Marcus theory for electron transfer between two molecules. Electron transfer occurs at the crossover point between the potential energy surfaces for the initial ϵ_i and final ϵ_f states of the two molecule system. The difference between the equilibrium state energies of the initial and final states is marked as ΔE. The reorganisation energy is λ and the activation energy is E_A. Adapted from J. Nelson's PE-CDT lecture slides [44].

molecules in solution [45, 46]. For a hop to occur, the molecules and their surrounding environment must reorganise, from their initial equilibrium position, through an unstable distorted state, to a final equilibrium position. Figure 2.8 shows an illustration of the changes in energy during electron transfer between two molecules, with non-interacting (non-adiabatic) electronic wave functions for the initial state $\phi_i(q)$, with energy $\epsilon_i(q)$, and the final state, with wave function $\phi_f(q)$ and energy $\epsilon_f(q)$. The minima of the potential energy surfaces $\epsilon_i(q)$ and $\epsilon_f(q)$ are separated by a free energy difference ΔE, and are approximated as identically parabolic functions of nuclear coordinate q, assumed invariant during the charge transfer (Franck Condon Principle). By conservation of energy, charge transfer can only occur when the nuclear coordinates of the initial and final states are identical. Thus, the activation energy E_A for charge transfer is defined by the intersection point of the two parabolas. The energy cost associated with the changes in nuclear positions and the dielectric configuration when distorting the molecules to accommodate the transfer of charge is called the

22

reorganisation energy λ. Graphically, λ represents the 'sharpness' of the parabola, that is the combination of the curvature and separation of the initial and final states. In the high temperature limit where vibrational modes can be treated classically, Marcus theory yields an electron transfer rate for the weak coupling regime of

$$\Gamma_{if} = \frac{2\pi}{\hbar} |J_{if}^2| \frac{1}{\sqrt{4\pi\lambda kT}} \exp\frac{-(\Delta E + \lambda)^2}{4\lambda kT}, \tag{2.15}$$

where J_{if} is the *transfer integral*, representing the electronic coupling strength between the states.

Charge carrier mobility

Considering a linear chain of identical states under a constant applied electric field, Equation (2.15) yields an expression for the charge carrier mobility

$$\mu = \frac{|J_{if}|^2}{\hbar} \sqrt{\frac{\pi}{\lambda kT}} \exp\left(\frac{-\lambda}{4kT}\right) \frac{ea^2}{kT}, \tag{2.16}$$

where a is the hopping distance between intermolecular sites [44]. The mobility μ quantifies how fast a charge moves in response to an electric field F, and is an key parameter for electronic devices. For example, the switching speed of a field-effect transistor is dependent on mobility [47]. Using typical values of $J \approx 0.01$ eV, $\lambda \approx 0.5\,\text{eV}$ and $a \approx 10^{-9}\,\text{m}$ in Equation (2.16), the mobility is around $\mu \approx 6.5 \times 10^{-3}\,\text{cm}^2\text{V}^{-1}\text{s}^{-1}$, which, in general, is far lower than inorganic semiconductors. The mobility shows an Arrhenius-type temperature dependence at device relevant temperatures, as the exponential term in Equation (2.16) dominates.

Experimental measurements of mobility in organic semiconductors can give very different results depending on many factors, including the measurement technique [48], the device geometry [49], and the sample preparation conditions [50]. Comparisons of mobility between experimental studies is therefore difficult. Even 'identical' measurements using the same samples have been found to depend on the lab they're measured in [51].
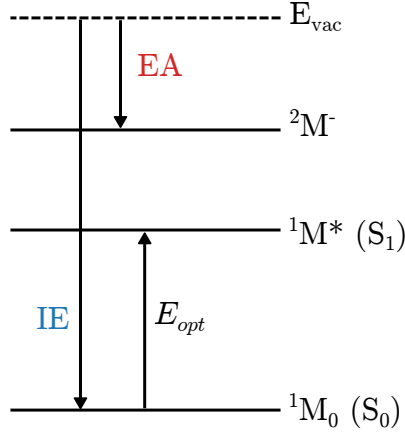
Figure 2.9: Illustration of single molecule gap energies. Optical gap E_{opt} is defined between the transition of the (singlet) electronic ground state $^1M_0$ (S_0) and the lowest (singlet) excited state $^1M^*$ (S_1), considered here to be accessible by absorption of a photon. The ionisation energy (IE) is marked between the vacuum level E_{vac} and $^1M_0$ (S_0), and the electron affinity (EA) is from E_{vac} to the charged state $^2M^-$. For simplicity, the vibronic levels are not shown.

2.1.6 Interaction with light

The absorption of a photon can induce a transition of an electron from the electronic ground state S_0 of a molecule to the lowest excited state S_1. The *optical gap* E_{opt} is defined as the difference in energy between S_1 and S_0, as illustrated in Figure 2.9. The photogenerated electron-hole pair are Coulombically bound, and collectively called an *exciton*.

The interaction of molecules with light is highly relevant for solar cells and light emitting diodes. Interested readers are referred to references [22, 52, 53]. In this thesis, the only devices presented are thin film transistors which, in this case, do not emit visible light and are measured in the dark. There are however absorption measurements presented in Chapter 5, which are used to identify ionised molecular species via a characteristic absorption peak.

2.2 Molecular doping

2.2.1 Introduction to doping

Doping is the controlled introduction of impurities, with the aim of increasing the electrical conductivity and shifting the Fermi level toward the transport level, enabling energy-level alignment of electronic levels at interfaces and minimising Ohmic loss across devices [14, 16, 18]. For the latter, doping can improve the electrical conductivity σ of a semiconductor

$$\sigma = e \cdot \mu \cdot p, \tag{2.17}$$

through an increase in the density of charge carriers p, and/or through enhancement of the mobility μ.

For inorganic semiconductors, the dopants replace atoms in the highly-pure and crystalline lattice of the host material. The covalently bonded dopants create states in the the fundamental gap of the host material which either donate an electron to the conduction band (n-type) or accept an electron from the valence band (p-type doping). These defect states are usually designed to be less than $25\,\text{meV}$ from the band edges thus by Fermi-Dirac statistics (see section Section 2.2.3) close to all dopants are ionised at room temperature. The high efficiency of this ionisation process means that low impurity concentrations are sufficient for doping, and typical ratios are around 10^{-6} to 10^{-3}. Consequently, the crystalline lattice of the host semiconductor is largely unperturbed, which is critical for operation as the electronic scattering associated with the dopant sites is minimised.

For organic electronic devices, such as solar cells [13], light emitting diodes (OLEDs) [14, 15] and field-effect transistors [16, 17], the use of controlled doping has substantially improved device performance. Although commercially successful in OLED displays, the fundamental principles governing efficient doping in organic semiconductors remain a topic of debate. In this section, the current understanding of doping is summarised, and is largely based on existing reviews [17, 54]. Only p-type doping is

used in this thesis, and thus forms the focus of this section. For discussion of n-type doping, interested readers are referred to references [55–57].

Brief history of p-doping

Early experiments to dope organic semiconductors involved using elemental species e.g. metals or gases, following the development of doping in inorganic semiconductors. In 1954, Akamatu et al. observed the conductivity of perylene increase by 22 orders of magnitude when exposed to bromine vapour [58]. Subsequent studies confirmed the role of halogen gasses as p-type dopants, often using phthalocyanines as the host semiconductor [59–61]. The range of p-type dopants has since expanded to include metal halides (such as CuI [62] and $FeCl_3$ [63]) and metal oxides (e.g. MoO_x [64] and WoO_3 [65]). Although these methods involving ions and small compounds as dopants were successful in increasing the conductivity of thin films, their use in device fabrication has been limited due to the issue of dopant diffusion [16, 66]. Firstly, the tendency for dopants to move through a film prevents accurate tuning of the doping concentration [67]. Furthermore, dopant diffusion can degrade device performance, for example in OLEDs - through quenching of excitons in the emission layer [68], and in solar cells - where dopants can hinder charge carrier collection [69, 70].

The problem of dopant diffusion is alleviated by using larger species with greater mass, such as molecular dopants. A common example of a molecular p-type dopant is F_4-TCNQ[1] which has been used to successfully p-dope a range of organic hole transporting materials, and improve the performance of organic devices [14, 16, 71]. However F_4-TCNQ is generally unsuitable for use in vacuum deposition processing as it has a high vapour pressure and tends to evaporate at low temperature under vacuum, leading to unintentional doping in the deposition of subsequent organic layers [72, 73]. Despite its molecular weight, F_4TCNQ still faces issues of diffusion through organic layers [73]. To reduce diffusion and mitigate the contamination issues, F_6-TCNNQ[2] was developed with a greater molecular mass than F_4-TCNQ, and has

---

[1]2,3,5,6-tetrafluoro-7,7,8,8-tetracyanoquinodimethane
[2]2,2'-(perfluoronaphthalene-2,6-diylidene)dimalononitrile

p-doped a range of hole transporting organic layers [74–76]. Other than F_6-TCNNQ, p-type dopants suitable for vacuum deposition include $Mo(tfd)_3$[3] [77], CN_6-CP[4] [15, 78] and $C_{60}F_{36}$ [72].

2.2.2 Mobile charge carrier generation

The process by which a molecular dopant generates mobile carriers, can be simplified as: (1) initial charge transfer between host and dopant, followed by (2) charge dissociation. Following carrier generation, the charge must avoid trap states to remain a mobile carrier.

Charge transfer: Integer vs partial charge transfer

The prevailing practice for selecting host and dopant combinations is based on securing a favourable offset between the host and dopant's energy levels, typically measured independently from one another. For p-doping, this involves introducing a dopant with an electron affinity (EA) larger than the ionisation energy (IE) of the host semiconductor. Electron transfer is then thought to take place from the host to the dopant, as drawn in Figure 2.10a. The charge transfer results in an acceptor anion (the ionised dopant) and a donor cation (the host semiconductor), collectively known as an *integer charge transfer complex* (ICTC). Analogously for n-type doping, electron transfer takes place from the HOMO of the dopant to the LUMO of the host. Overall, this mechanism is described as *integer charge transfer* or *ion-pair formation* [54, 79, 80].

The efficiency of integer charge transfer depends primarily upon the relative position of the host and dopant energy levels. In Figure 2.10a, the p-type doping is termed as *strong*, because the EA of the dopant is greater than the IE of the host, typically measured independently in pristine films of each material. In this scenario, charge transfer is largely independent of temperature [81]. Strong p-type dopants generally require EA's in the range of $5\,\mathrm{eV}$ to $6\,\mathrm{eV}$ below the vacuum level to dope typical hole

---

[3]molybdenum tris[1,2-bis(trifluoromethyl-)ethane-1,2-dithiolene
[4]hexacyano-trimethylene-cyclopropane

a Integer charge transfer (ICT)   **b** Charge transfer complex (CTC)
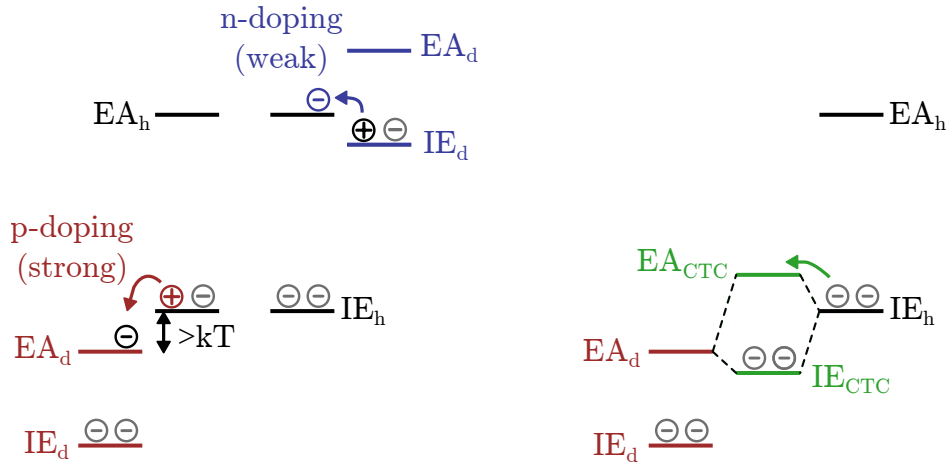
Figure 2.10: Schematic energy level diagram of charge transfer doping models. **(a)** Integer charge transfer (ICT) for p-type dopant, here shown as an example of a *strong* p-dopant with the acceptor level of the dopant below the IE of the host. Also shown is *weak* n-type doping, where charge transfer must overcome an energy offset between the donor level of the dopant and EA of the host. The ICT model assumes weak overlap between the frontier molecular orbitals of the host and dopant, and is characterised by complete transfer of a single electron (marked by the red a blue arrows). **(b)** The hybridisation model assumes a strong coupling between the frontier molecular orbitals of the host and dopant, such that they form a charge transfer complex with new electronic levels (marked in green). The antibonding orbital of the charge transfer complex EA_{CTC} then acts as the acceptor level for generating holes in the host semiconductor. For clarity, only the electron affinities EA and ionisation energies IE are marked.

transporting layers (HTLs) [82]. Analogously, strong n-type dopants must have an IE smaller than the EA of the host, which, for electron transporting layers in solar cells, generally means around $3.5\,\text{eV}$ below the vacuum level or lower [22]. The case of a *weak* n-type dopant is illustrated in Figure 2.10a, where the IE_d sits above the EA_h, resulting in an energy barrier for charge transfer. Consequently, charge transfer is thermally activated with a strong dependence on the relative offset between EA_h and IE_d.

An alternative hybridisation model, involving the formation of a ground-state *charge-transfer complex* (CTC), has been proposed [80, 83–85]. In the CTC, the frontier molecular orbitals of the host and dopant are strongly coupled and form hybridised energy levels with an occupied bonding orbital and an empty antibonding orbital, as sketched in Figure 2.10b. The antibonding orbital of the CTC then acts as the acceptor level for charge transfer with a host molecule.

In this hybridisation model, the CTC energy levels can be described using a Hückel-type model [54]. The two-site Hamiltonian can be constructed using the energies of the orbitals, marked EA_d for the acceptor level of the dopant and IE_h for the donor level of the host, as well as the transfer integral between them J_{dh}:

$$\hat{H} = \begin{pmatrix} EA_d & J_{dh} \\ J_{dh} & IE_h \end{pmatrix}. \tag{2.18}$$

Solving this Hamiltonian yields the eigenvalues, which are the energy levels of the hybridised states (marked as EA_{CTC} and IE_{CTC} in Figure 2.10b). The associated eigenvectors represent the relative contribution of the host and dopant orbitals to the hybridised states, and determine the amount of charge transfer in the CTC. As this can give non-integer values, the hybridisation model is sometimes referred to as *partial charge transfer*.

With the Hückel-type model, the antibonding orbital of the CTC has an energy greater than the IE of the surrounding host molecules ($EA_{CTC} > IE_h$), regardless of the initial host and dopant energy states. This leads to an energy barrier for charge transfer from the host to the CTC. Consequently, the formation of CTCs in the doping process always produces weak dopants. The energy barrier can be

minimised by selecting host and dopants with similar HOMO and LUMO energies, and by reducing the electronic coupling between the frontier orbitals [54].

Besides the relative energy levels and the charge transfer mechanism, an unfavourable morphology in which dopants are not homogeneously dispersed can reduce the charge transfer efficiency [86]. Pure dopant crystal phases in the mixed films can form, particularly at high doping concentrations, which further inhibit charge transfer [87].

Charge dissociation

Following charge transfer, the hole on the host semiconductor must dissociate from the ionised dopant or complex, in order to become a mobile carrier. This is illustrated for ICT in Figure 2.11a. The binding energy E_b of the ion pair can be approximated considering the Coulomb interaction between them (ignoring polarisation effects)

$$E_b(r) = \frac{e^2}{4\pi\epsilon_0\epsilon_r}\frac{1}{r} \tag{2.19}$$

where r is the distance of separation. Taking a typical static dielectric constant of $\epsilon_r \approx 3$ for organic semiconductors [88] and an intermolecular distance of $r \approx 1\,\mathrm{nm}$, yields a binding energy $E_b \approx 0.5\,\mathrm{eV}$. As this approximate binding energy far exceeds the thermal energy at room temperature ($kT = 25\,\mathrm{meV}$), only a very small fraction of charges are expected to dissociate. However, this simple model neglects other effects which may reduce the barrier to dissociation, such as Coulomb potential overlap, [89] energetic disorder [81] or charge-quadrupole interactions [12].

Avoiding trap states

Once generated and separated, the charge carriers must avoid trap states to contribute to the electric current. Figure 2.11b illustrates a hole trap at energy E_t in the band gap of the host semiconductor. In disordered organic semiconductors, it is useful to define an effective transport level, below which electronic states tend to hinder hopping transport [90, 91]. These trap states can arise from impurities and/or molecular defects in the semiconductor material [92–94].

a Charge dissociation **b** Charge trapping
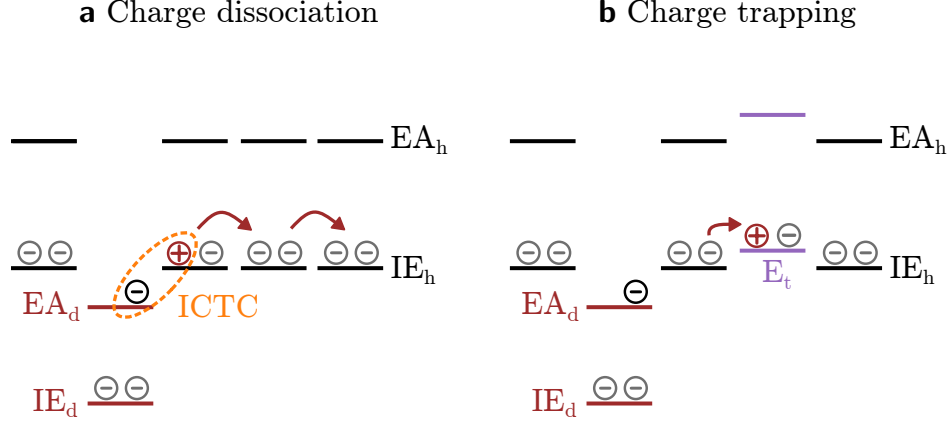
Figure 2.11: Illustrations of doped charge dissociation and trapping. (a) Charge dissociation from an integer charge transfer complex (ICTC). To become a mobile carrier, the hole on the host semiconductor must escape the Coulombic interaction with the dopant anion. **(b)** Charges must avoid trap states E_t within the host band gap to remain mobile carriers. The trapping of extrinsic charges lowers the doping efficiency. For clarity, only the electron affinities EA and ionisation energies IE are marked.

Overall doping efficiency

Overall, the p-doping process for host H and dopant D can be written as:

$$\text{DHHH}_t \rightleftharpoons \underbrace{[D^-H^+]}_{\text{CTC}} HH_t \rightleftharpoons \underbrace{D^-HH^+H_t}_{\text{mobile carrier}} \rightleftharpoons \underbrace{D^-HHH_t^+}_{\text{trapped carrier}} \qquad (2.20)$$

where H_t is a trap state in the host semiconductor and $[D^-H^+]$ is the charge transfer complex (integer or partial). Dopant and host combinations are carefully chosen, such that the equilibrium position of the initial charge transfer step lies towards the CTC side. However, because of the large binding energy, the equilibrium position of the charge dissociation step tends toward the CTC rather than the mobile carrier side. The density of mobile charge carriers is in thermal equilibrium with the density of trapped charges. The mobile carrier doping efficiency η_{mob} is then the ratio of mobile charge carriers to the dopants in the film:

$$\eta_{mob} = \frac{p_{mob}}{N_A} \qquad (2.21)$$

and is typically low for organic semiconductors [17, 81]. Consequently, the doping concentrations relevant for organic devices (usually in the range of 1-10 dopants per 100

host molecules) are comparatively higher than their inorganic counterparts (roughly 1 dopant per million hosts) [95].

2.2.3 Occupation statistics of doped semiconductors

Mathematically, the description of doped organic semiconductors largely follows that of inorganic semiconductors. Therefore, we return to the ideas in Section 2.1.2 and reintroduce the Fermi level E_F and valence and conduction band energies E_v and E_c. Considering only single-value (δ-type) energy levels, that is no disorder, E_v and E_c can be though of as the host material's IE and EA, respectively. The ionisation of a p-dopant can be described by thermal activation of an electron from the valence band of the host to the acceptor level E_A of the dopant [96, 97]. The number density of ionised acceptors N_A^-, in thermal equilibrium, follows Fermi-Dirac statistics

$$N_A^- = \frac{N_A}{e^{(E_A - E_F)/kT} + 1},$$

(2.22)

where N_A is the density of acceptor states or dopants. The position of E_A relative to the Fermi level E_F, and the temperature T, dictates the likelihood of dopant ionisation. At room temperature, when E_A lies far below E_F, as shown in Figure 2.12a, the p-dopant is referred to as a *shallow* dopant (or often a *strong* dopant in organic semiconductor literature). Electron transfer from the host to dopant is very likely, therefore the free carrier density p is approximately equal to the dopant density

$$p = N_A^- = N_A.$$

(2.23)

For the case of a shallow dopant, the free charge carrier density increases linearly with dopant concentration.

For the case of a *deep* (or weak) dopant, shown in Figure 2.12b, E_A is above E_F and only a small proportion of dopants ionise, dependent on the temperature. At high temperatures, the thermal activation energy of a deep acceptor state is given by

$$\Delta E = \frac{E_A - E_v}{2}$$

(2.24)

a Shallow acceptor   **b** Deep acceptor
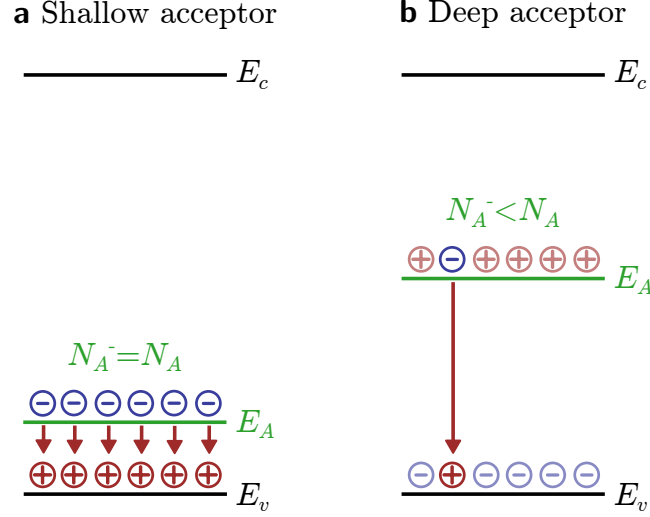
Figure 2.12: Schematic energy level diagram of shallow and deep acceptor states. (a) Shallow acceptor states where the dopant acceptor level E_A is below the Fermi level E_F. All dopants are ionised $N_A^- = N_A$. **(b)** Deep acceptor states where E_A is above E_F. The number of ionised dopants is temperature dependent.
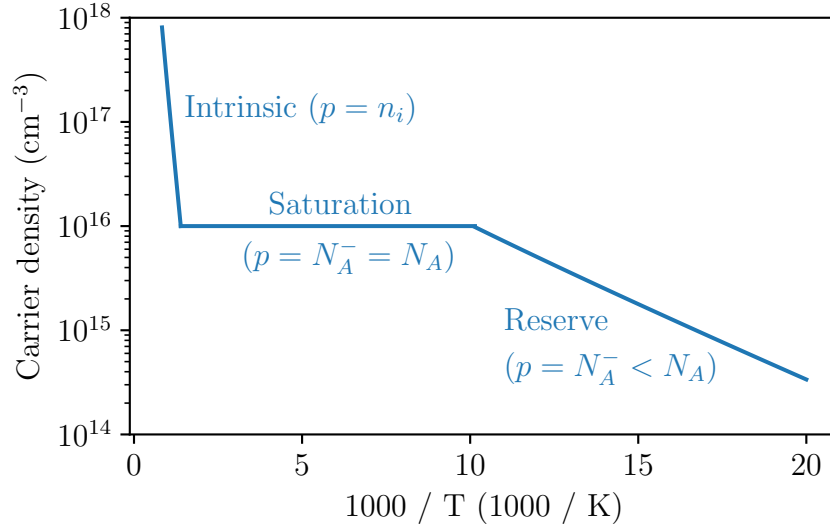
Figure 2.13: Temperature dependence of charge carrier density. Log plot of charge carrier density against inverse temperature, showing the intrinsic $p = n_i$, dopant saturation $p = N_A^- = N_A$ and dopant reserve $p = N_A^- < N_A$ regimes. The parameters for the simulation are: $N_A = 10^{16}\,\mathrm{cm}^{-3}$ and $E_A - E_v = 50\,\mathrm{meV}$.

with the number of free charges approximated with the Fermi integral (combining Equation (2.8) and Equation (2.22)):

$$p(T) \simeq \sqrt{N_A N_v} e^{-\Delta E/kT}. \tag{2.25}$$

The distinction between shallow and deep acceptor levels depends upon the temperature. Figure 2.13 shows the charge carrier density against inverse temperature for a semiconductor at a fixed dopant concentration N_A. At low temperatures, dopants with an acceptor level higher in energy than the valence band of the host semiconductor only partially ionise ($p = N_A^- < N_A$). This corresponds to the situation of a deep acceptor level, and is called the dopant reserve or freeze-out regime. By increasing the temperature, acceptor states far above the valence band become thermally accessible until all the dopants are ionised. This regime is marked as dopant saturation on Figure 2.13 and corresponds to the shallow acceptor level case ($p = N_A^- = N_A$). At very high temperatures, the contribution of intrinsic carriers (thermally excited across the host band gap) exceeds those generated by the dopant, and the charge carrier density is determined by the law of mass action (Equation (2.9)).

2.3 Organic devices

2.3.1 Contacts

When a semiconductor comes into contact with metal, the electrical contact between them is said to be either non-rectifying (Ohmic) or rectifying (Schottky contact). For most devices, unhindered Ohmic injection is desirable. Figure 2.14a shows the energy level diagram for a metal-semiconductor interface before contact. The metal work function Φ_m, that is the energy required to remove an electron from the metal surface to the vacuum level E_{vac}, is less than the Fermi level E_F of the semiconductor. After contact, sketched in Figure 2.14b, holes jump from the semiconductor to the metal, creating a depletion region and barrier on the semiconductor side of the interface. The barrier height Φ_b as seen by the majority carriers, holes in this example, coming from the metal is given by

$$q\Phi_b = (q\chi + E_g) - q\Phi_m \tag{2.26}$$

where E_g is the electronic band gap of the semiconductor and χ is its electron affinity. This barrier as seen from the semiconductor-side, called the junction potential or built-in voltage V_{bi}, is given by

$$qV_{bi} = q(\Phi_s - \Phi_m) \tag{2.27}$$

where Φ_s is the Fermi level depth relative to E_{vac}. Assuming an abrupt end to the depletion region in the semiconductor of permittivity ϵ, the depletion width w can be calculated using Poisson's equation

$$\frac{d^2V(x)}{dx^2} = -\frac{\rho(x)}{\epsilon} \tag{2.28}$$

with the boundary conditions $V(\infty) = 0$, $E(\infty) = 0$, for a rectangular charge distribution $\rho(x) = -qN_A$ for $0 \leq x \leq W$. Charge neutrality is maintained by an infinitesimal layer of positive charge in the metal at $x = 0$. Integrating twice and considering an external bias $V(x = 0) = V_{bi} - V$, the extent of the depletion width is
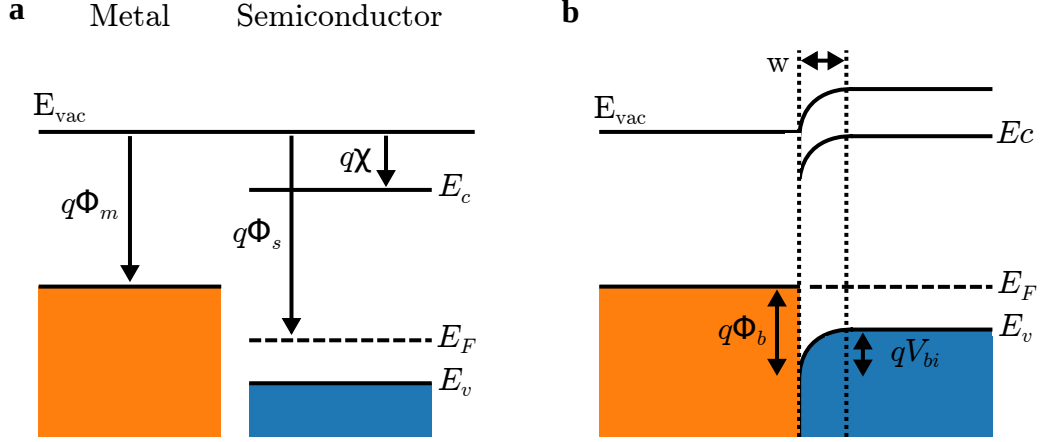
Figure 2.14: Schematic energy level diagram before and after contact at a metal-semiconductor interface. (a) Schematic before contact showing a metal with work function Φ_m and semiconductor with E_F at different potentials. **(b)** In equilibrium after contact, the metal work function and semiconductor Fermi level equilibrate, creating a barrier for majority carriers from the metal side of Φ_b and a barrier from the semiconductor side of V_{bi}.

given by

$$W(V) = \sqrt{\frac{2\epsilon(V_{bi} - V)}{qN_A}}, \tag{2.29}$$

for applied voltages below the built-in voltage $V < V_{bi}$. This equation highlights two practical ways of avoiding rectifying contacts at metal-semiconductor interfaces: by matching work functions to minimise V_{bi}, and increasing charge density, which, for example, can be achieved by doping.

2.3.2 Field-effect transistors

Field-effect transistors come in many varieties, however organic transistors predominately fall under the heading of thin film transistors (TFTs). Commercially available TFTs are employed as the pixel switching elements in active matrix displays, however these TFTs are mostly based on amorphous silicon. Switching to organic transistors offers an important advantage over their inorganic counterparts in that they can be processed at low temperatures. Low temperature processing has unlocked the use of a greater range of low-cost substrates including flexible plastics [98] and paper [99].
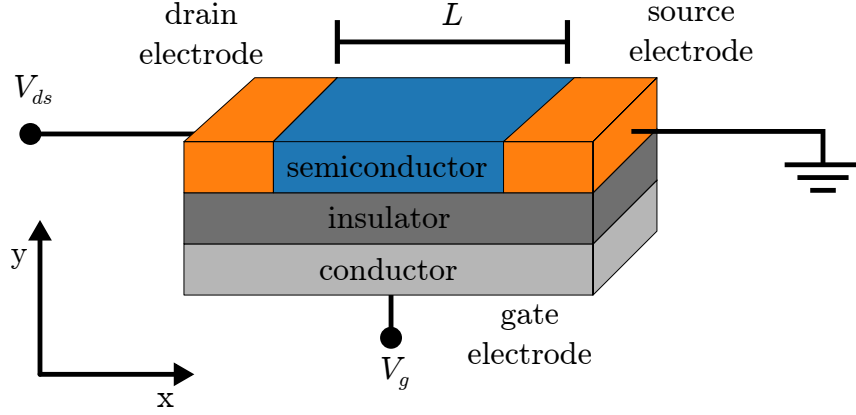
Figure 2.15: Schematic diagram of a TFT device. Schematic showing a bottom-contact bottom-gate TFT, with channel length L. The gate voltage V_g and source-drain voltage V_{ds} are given with respect to the source electrode, which is grounded.

In Figure 2.15, the geometry a bottom-gate bottom-contact TFT is sketched with a channel width W and length L. The following analysis treats the device purely in two-dimensions, as outlined in reference [100], and assumes the *gradual channel approximation*. The gradual channel approximation is based on two assumptions: (1) that the transverse electric field from the gate is much larger than the longitudinal source-drain electric field, and (2) the mobility is independent of the charge carrier density [96, 101]. To begin, the transistor is treated as a simple parallel plate capacitor, such that all charge is situated at the interface on either side of the dielectric layer. The charge in the device is directly proportional to the potential difference across the insulator

$$\rho(x) = C_{ox}[V(x) - V_g] \tag{2.30}$$

where $\rho(x)$ is the charge density at position x, C_{ox} is the capacitance of the insulating layer, $V(x)$ is the potential in the device and V_g is the potential at the gate, both with respect to the source electrode. Neglecting diffusion, the current at position x in the channel is given by Ohm's Law

$$I(x) = -qp(x)\mu W \frac{dV(x)}{dx} \tag{2.31}$$

37

where $qp(x)$ is the free charge carrier density (assuming no traps or doping), μ is the charge carrier mobility, and the last term is the electric field. Integrating Equation (2.31) over the length of the channel with boundary conditions at the contacts ($V(0) = 0$ and $V(L) = V_{ds}$), the total current is

$$I_{ds} = \mu C_{ox} \frac{W}{L}((V_g - V_t)V_{ds} - \frac{1}{2}V_{ds}^2) \tag{2.32}$$

where V_t is the threshold voltage, which is introduced to address any immobile charge in the device (trap states or ionised dopants). When the potential at the drain electrode is equal to the gate bias $V_{ds} = V_g$, there is no voltage drop and therefore no charge at the contact. At this point, the channel is said to be pinched-off and the current remains constant at a saturation value of

$$I_{ds}^{sat}(V_g) = \mu C_{ox} \frac{W}{L} \frac{1}{2}(V_g - V_t)^2 \tag{2.33}$$

For $V_{ds} << V_g$, Equation (2.31) can be approximated by

$$I_{ds}^{lin}(V_g, V_{ds}) = \mu C_{ox} \frac{W}{L}(V_g - V_t)V_{ds} \tag{2.34}$$

giving two methods for measuring the field-effect mobility via the derivative of the transfer curve. Figure 2.16 shows a simulation on a n-type OFET using the above, idealised equations. The thin lines represent the linear regime simulated using Equation (2.31) and the thick lines are the saturation regime using Equation (2.33).

OFET devices are referred to as either being p- or n-type depending on if the majority carriers through the semiconductor are holes or electrons, respectively. This terminology has been lifted from the metal-oxide-semiconductor field-effect transistor (MOSFET) literature where the type of doping of the inorganic semiconductor dictates whether the majority carriers are hole or electrons. For OFETs, the organic semiconductor is often not intentionally doped and so the reference to p- or n-type does not relate to doping. Instead, p-type means that the device shows unipolar hole transporting behaviour, and n-type means unipolar electron transporting behaviour, and this has been shown to depend on the contact metals used [102, 103].
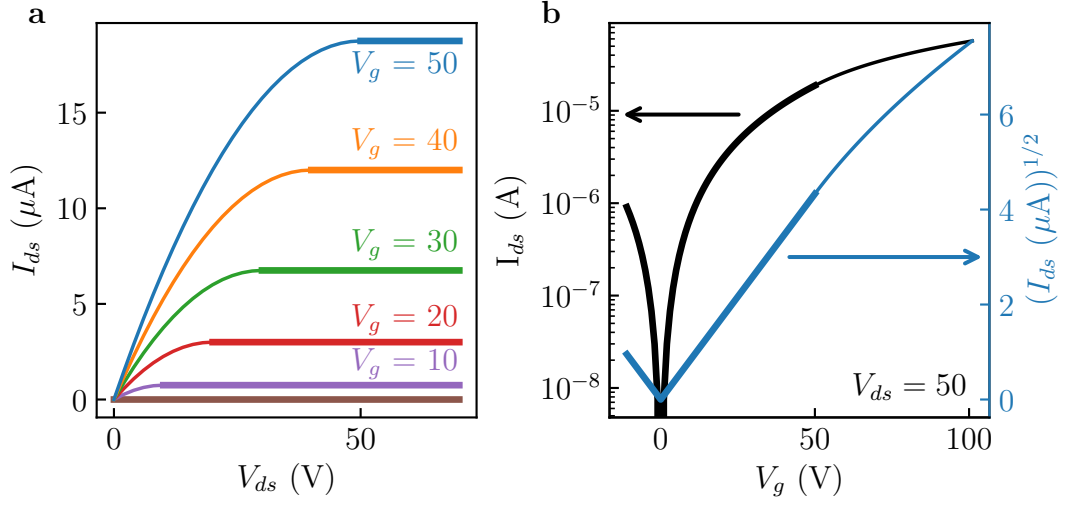
Figure 2.16: Ideal OFET output and transfer curves. Simulations of a n-type OFET with **(a)** output characteristics (V_{ds} sweep at constant V_g) and **(b)** transfer characteristics (V_g sweep at constant $V_{ds} = 50$ V). The thin lines represent the linear regime simulated using Equation (2.31) and thick lines represent the saturation regime simulated using Equation (2.33). Parameters are: $C_{ox} = 1.5 \times 10^{-4}$ F/m^2, $W = 10$ mm, $L = 10$ µm, $V_t = 0$ V and $\mu = 1 \times 10^5$ cm^2/Vs.

Although the gradual channel approximation illustrates the basic principles of TFTs, real devices show behaviour that deviates from Figure 2.16. The main reasons for non-ideal behaviour include: insulator leakage currents, contact effects, and parallel conductance. In the following section, we address the issue of non-ideal contacts, which can result in resistance across the contact, and/or a Schottky barrier [100, 104, 105].

Contact effects

During sample fabrication, contact resistance can arise when the source and drain electrodes are not in contact with the accumulation channel of the OFET. This can occur for OFETs with bottom-gate top-contact geometry, where the semiconductor separates the accumulation channel from the contacts, and for bottom-gate bottom-contact geometry, when the deposition method does not form a continuous layer along the interface, creating a gap next to the contact. The OFET can be modelled with resistors R at each contact, as shown in the inset of Figure 2.17a. The effect of contact resistance modelled in this way is that the output curves pinch together.

With increasing I_{ds}, the voltage drop across the contact resistors increases. This reduces the voltage between the OFET source and drain, and across the insulator, so that I_{ds} decreases. For very large values of resistor, I_{ds} becomes independent of V_g, as the majority of the voltage is dropped across the resistors.

Contacts are often thought to form Schottky barriers as the Fermi level of the semiconductor shifts to match the work function of the metal electrodes. This can be modelled as anti-parallel Schottky diodes at the contacts, as shown in the inset to Figure 2.17b. The anti-parallel diodes have a current-voltage relation given by

$$I = 2I_0 \sinh(\frac{qV}{nkT}) \tag{2.35}$$

where I_0 is the reverse-bias saturation current and n is the ideality factor. Figure 2.17b shows simulations of an OFET with diodes at the contacts. The only apparent change from the ideal case occurs at low V_{ds}, where the output curve becomes non-linear. Although this model recreates the effects seen around the origin for real OFETs, the physical reasons for this remain unclear [100].

The transmission line method (TLM) offers an experimental way to measure the contact resistance [102, 106–108]. Assuming that the resistance at the contacts is independent of the channel voltage, the contact resistance can be estimated by plotting the total channel resistance as a function of channel length and extrapolating to a channel length of zero. Although this method of determining the contact resistance is widely-used, there is often a large degree of uncertainty in the extracted values of resistance, arising from the device-to-device parameter variations in OFET mobility and threshold voltage (particularly for OFETs fabricated on bare or untreated SiO_2, with significant trapping at the interface) [2]. The extraction accuracy can be improved using a modified-TLM (M-TLM) method involving a linear fit on a plot of $R_{tot}W/L$ against inverse channel length $1/L$ [109]. In this approach, which is used in Chapter 4, the gradient of the fit is determined by the contact resistance rather than the channel resistance. As the contact resistance generally shows less device-to-device variation than the channel resistance, linear fits can be made with less associated uncertainty.
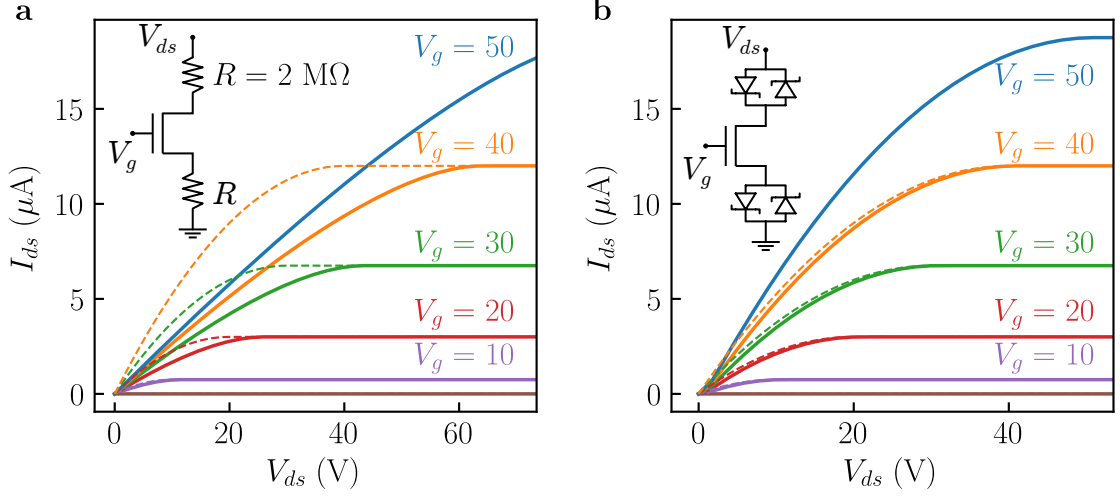
Figure 2.17: Contact effects in OFETs. (a) Simulated output curve of a n-type OFET with resistors R at both contacts as shown in the inset. Parameters are: $R = 2\,\text{M}\Omega$, $C_{ox} = 1.5 \times 10^{-4}\,\text{F/m}^2$, $W = 10\,\text{mm}$, $L = 10\,\mu\text{m}$, $V_t = 0\,\text{V}$ and $\mu = 1 \times 10^5\,\text{cm}^2/\text{Vs}$. **(b)** Simulated output curve of a n-type OFET with anti-parallel Schottky diodes at the contacts, with additional parameters $I_0 = 10^{-14}\,\text{A}$ and $nT = 300\,\text{K}$. The ideal cases up to $V_g = 40\,\text{V}$ are shown for comparison as dashed lines.

Threshold voltage

The threshold voltage V_T is often used as an evaluation parameter for OFETs, as it is closely linked to the operational and shelf lifetime of the device [110]. From the threshold voltage, it is common practice to extract information about the impurity concentration [111], traps [112] and interface states [113]. These immobile charged species require an extra bias at the gate, that is the threshold voltage, so that they are compensated for. The accumulation channel then becomes open for majority carrier transport. As before, treating the device as a parallel plate capacitor (see Equation (2.30)), the threshold voltage can be written as

$$V_T = \frac{-qN_T^+}{C_{ox}} \tag{2.36}$$

where N_T^+ refers to immobile positive trapped charges. These must be compensated for before the holes accumulating at the interface can form a conductive channel through the semiconductor.

2.3.3 Logic gates

Current digital electronics is based upon the idea that there are only two states possible in a circuit at any point (e.g. a transistor is either in saturation or is non-conducting). Each state is associated with a nominal voltage and a valid range over which it is interpreted, with the levels called `HIGH` and `LOW` (or `1` and `0` or `TRUE` and `FALSE`). Logic operations are performed with *gates*, whose basic forms are `AND`, `OR` and `NOT` (also called the voltage inverter).

Figure 2.18a shows the graphical representation and truth table for a voltage inverter. The inverter outputs the complement of the input, `HIGH` becomes `LOW` and vice versa. Typical voltage transfer characteristics are shown in Figure 2.18b. The noise margin represents the range of values which the digital circuit will recognize as the `HIGH` or `LOW` state, and is important for allowing for manufacturing spread, variations of the circuit with temperature, loading, supply voltages and many other sources of electrical noise [114]. The noise margin (maximum equal criterion) for an inverter can be calculated by mirroring the input and output voltages in the transfer characteristics and determining the maximum size square that fits between the original and mirrored curves (dotted square in Figure 2.18b.) Finally, for use in large scale integrated circuits, the inverter often requires a gain $\Delta V_{out}/\Delta V_{in} > 1$.

Logic families

The voltage inverter can be constructed in one of several different designs (also called logic families). Each family has specific characteristics (supply voltage, voltage tolerance, speed etc.), meaning that logic functions of different families are often incompatible. In Figure 2.19, three logic families are shown; unipolar, complementary and complementary-like. For the unipolar inverter, when V_{in} is `HIGH`, the n-type transistor is on and V_{out} is pulled to ground. When V_{in} is `LOW`, the voltage drop across the resistor is small compared to the drop across the transistor, and the output is pulled to the rail voltage V_{dd}. While unipolar logic offers simple fabrication (only one semiconductor and one contact material needed), the designs suffer from high power
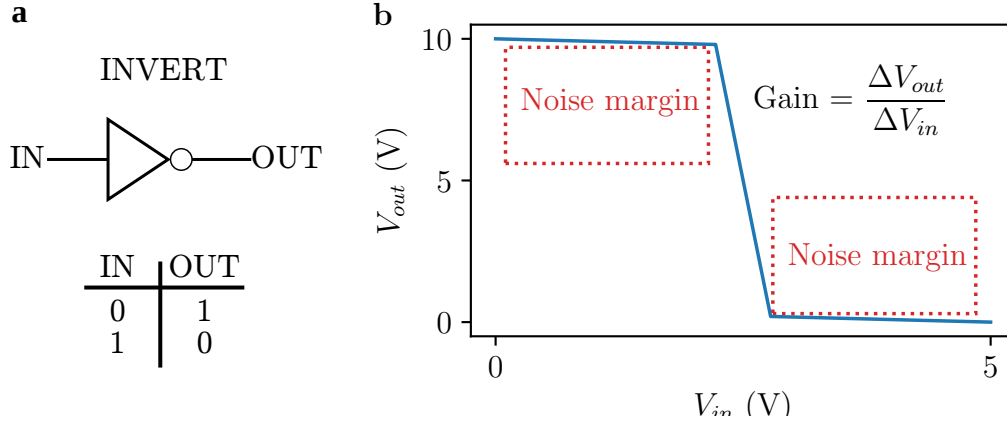
Figure 2.18: Inverter (NOT gate) symbol, truth table and transfer characteristics. (a) Standard graphic symbol and truth table. **(b)** Drawing of the transfer characteristics showing V_{in} against V_{out} for a typical voltage inverter. The gain is defined as the $\Delta V_{out}/\Delta V_{in}$ and the noise margin marked represents the threshold for which the signals will register as HIGH and LOW.
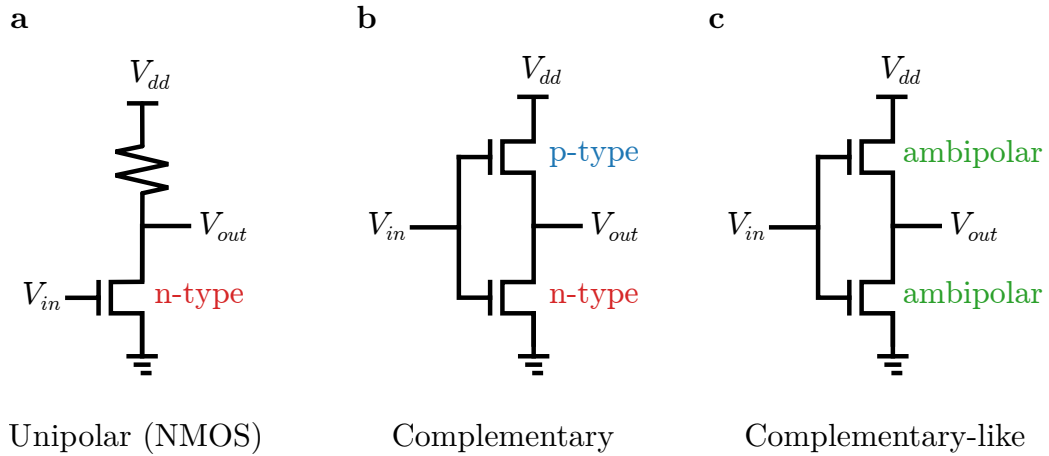
Figure 2.19: Logic families demonstrated in a voltage inverter. (a) Unipolar logic demonstrated using a single n-type metal-oxide-semiconductor (NMOS) transistor, **(b)** complementary logic, also referred to as complementary metal-oxide-semiconductor (CMOS), and **(c)** complementary-like, or ambipolar, logic, to construct a voltage inverter.

consumption and poor noise margin. Whenever the output is LOW, a direct current flows through the gate leading to static power dissipation.

Modern integrated circuits predominately make use of complementary metal-oxide-semiconductor (CMOS) logic, which offers far lower static power dissipation than unipolar designs. Complementary inverters dissipate power only when transitioning between logic states, although very low static power dissipation may occur from gate leakage currents in the individual transistors. Furthermore, complementary logic offers higher gain, better noise margins and a greater achievable density of logic functions on a chip. However, the drawback of using two transistors is that fabrication is more complex, with additional processing steps needed to deposit different n- and p-type semiconductors and two electrode materials.

The final logic family displayed in Figure 2.19c is that based on ambipolar transistors, referred to as complementary-like logic. Ambipolar semiconductors allow for both polarities of charge to be induced in the device, such that transistors based on these materials can replace both the p- and n-type transistors in complementary logic, thus circumventing the advanced patterning techniques necessary to deposit two separate materials, simplifying the fabrication process. The electron and hole mobilities in these ambipolar devices must be balanced in order for the resulting logic gates to have symmetrical outputs [115].

Organic logic

To build fully organic integrated circuits based on complementary logic, high performance n-type materials are required. However, n-type organic semiconductors that have been reported stable at ambient conditions remain comparatively rare [110, 116]. As ambipolar behaviour has been reported for a range of organic semiconductors, complementary-like logic appears an attractive alternative. Phthalocyanines have demonstrated both p-type semiconducting behaviour and n-type behaviour depending on the attached side groups [50, 117]. Nénon et al. [118] achieved ambipolar behaviour by fabricating heterojunctions of copper phthalocyanine (CuPc) and its fully-fluorinated derivative $F_{16}CuPc$. They reported that OFETs based on stacked

44

bi-layers of the different CuPc derivatives gave better performance as compared to a blend of the two semiconductors mixed at a weight ratio of 1:1. Recent improvements towards balanced ambipolar transport in OFETs has come from Jiang et al. [119] who proposed a method of molecular crystal engineering to tune zinc phthalocyanine (ZnPc) films from p-type to n-type by replacing the hydrogen on the outer rings with fluorine F_xZnPc ($x = 0, 4, 8, 16$). The step-like shift in ionisation energy by fluorination resulted in a smaller Schottky barrier for electron injection at the organic-gold contacts such that ambipolar behaviour was observed for F_4ZnPc and n-type behaviour for both F_8ZnPc and F_{16}ZnPc. However, achieving balanced hole and electron mobility is difficult with only step-like shifts. In Chapter 4 of this thesis, continuous shifts in IE by mixing molecules with different degrees of fluorination are used to overcome the discrete energy steps given by molecular substitution.

3. Materials and methods

This chapter provides a brief description of the materials, methods and techniques used in this thesis. Section 3.1 gives details about the organic small molecules and the supplier information, with a summary of the material parameters in Table 3.1. Sample preparation takes place in a vacuum chamber by thermal sublimation, the details of which are described in Section 3.2. Section 3.3 outlines the experimental characterisation, and, finally, Section 3.4 gives details of the theoretical methods.

3.1 Materials

ZnPc

Zinc-phthalocyanine (ZnPc) is commonly used as a donor material in organic solar cells [13, 120, 121]. It is an intensely coloured blue-green powder, used as a pigment in the textile and paper industry. ZnPc is a cyclic compound of four pyrole-like subunits which surround a zinc ion, as drawn in Figure 3.1a. At least one of the lone pairs on the inner nitrogen atoms is shared with the metal ion. The ionisation energy (ionisation energy) of ZnPc, as measured with ultraviolet photoelectron spectroscopy (UPS), is $5.10\,\text{eV}$ [10]. ZnPc has been used in organic solar cells [122, 123], light-emitting diodes [14] and field-effect transistors [8]. The density for ZnPc varies in the literature between $1.55\,\text{g/cm}^3$ to $1.63\,\text{g/cm}^3$ [124, 125]. In this thesis the density was taken as $1.55\,\text{g/cm}^3$. The ZnPc for this study was purchased in sublimed grade from Lumtec Corp. (Taiwan) and used as received.
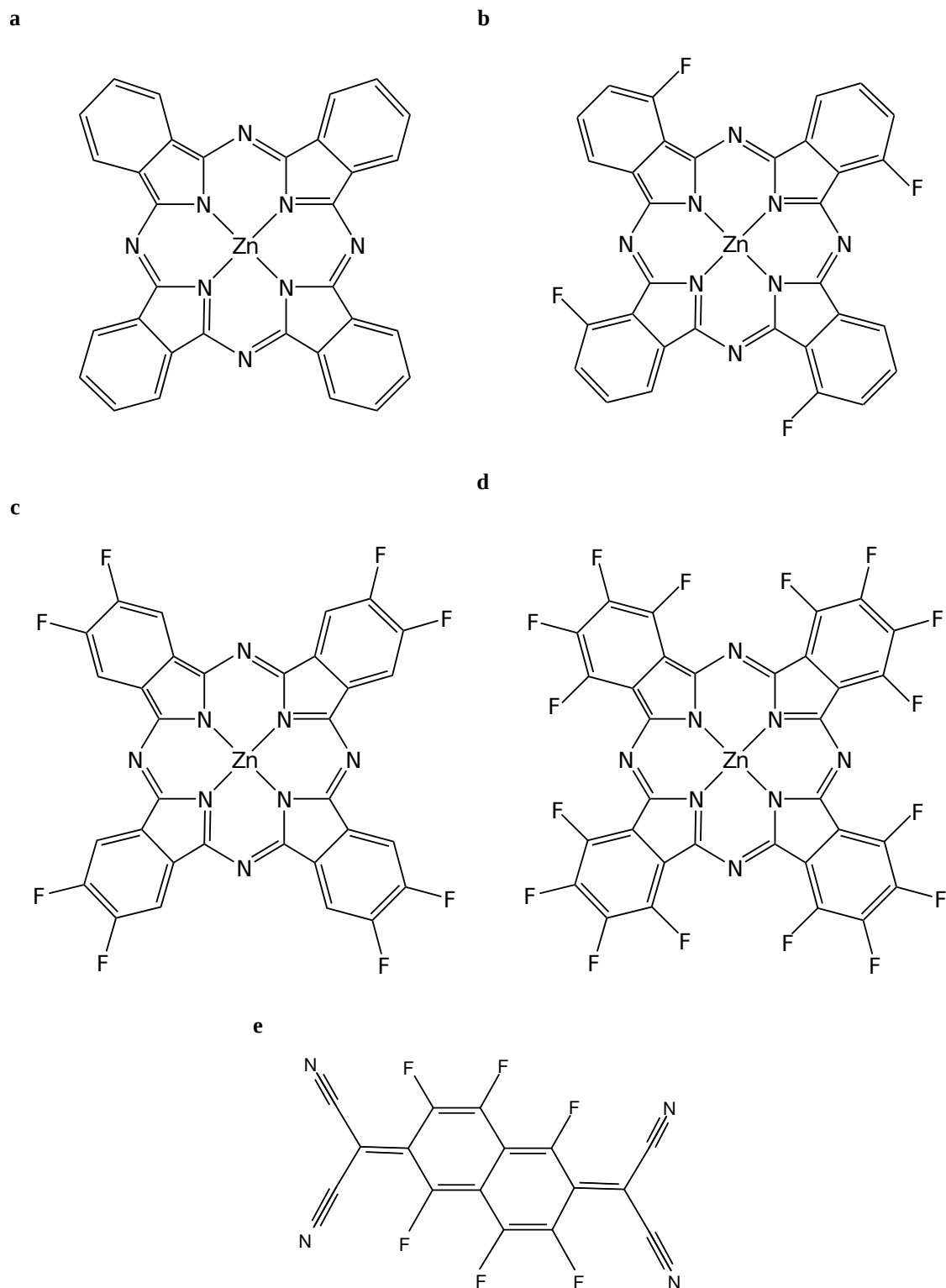
Figure 3.1: Chemical formulae of the molecular semiconductors of this thesis. Chemical structures of **(a)** ZnPc, **(b)** F_4ZnPc, **(c)** F_8ZnPc, **(d)** F_{16}ZnPc, and **(e)** F_6-TCNNQ.

F$_4$ZnPc

F$_4$ZnPc is the quadruply fluorinated derivative of ZnPc. The chemical structure of one of its isomers is displayed in Figure 3.1b. Other isomers exist with the fluorine atoms located at different positions on the outer rings. As fluorine has a large electronegativity, the fluorine atoms act to stabilise the molecular orbitals. Compared to ZnPc, F$_4$ZnPc has a larger IE at 5.80 eV (a mixture of isomers) [10]. With F$_4$ZnPc, higher open circuit voltages in organic solar cells have been achieved, when used in combination with C$_{60}$ as the acceptor [126]. The density of F$_4$ZnPc was assumed to be equal to that of ZnPc. The F$_4$ZnPc for this study was purchased in sublimed grade from Lumtec Corp. (Taiwan) containing a mixture of the isomers, and used as received.

F$_8$ZnPc

F$_8$ZnPc is the octuply fluorinated derivative of ZnPc. Its chemical structure is displayed in Figure 3.1c. With the addition of further fluorine atoms, the IE is larger than both ZnPc and F$_4$ZnPc, at 6.30 eV [10]. In an organic solar cells, F$_8$ZnPc has produced higher open circuit voltages than both ZnPc and F$_4$ZnPc, in combination with C$_{60}$ as the acceptor, however an insufficient energetic offset at the donor-acceptor interface has been reported to limit charge dissociation and, therefore, the short circuit current [129]. The density of F$_8$ZnPc was assumed to be equal to that of ZnPc. The F$_8$ZnPc for this study was purchased in sublimed grade from Lumtec Corp. (Taiwan) and used as received.

F$_{16}$ZnPc

F$_{16}$ZnPc is the sexdecuply fluorinated derivative of ZnPc. Its chemical structure is displayed in Figure 3.1d. F$_{16}$ZnPc has the largest IE of these derivatives, at 6.75 eV [10]. The large IE results in limited performance in combination with C$_{60}$ in organic solar cells [129]. The density of F$_{16}$ZnPc was assumed to be equal to that of ZnPc. The F$_{16}$ZnPc for this study was purchased in sublimed grade from Lumtec Corp. (Taiwan) and used as received.

	Molar mass (g/mol)	Density (g/cm^3)	IE (eV)	EA (eV)
ZnPc	577.9	1.55	5.10 [10]	3.34 [71]
F$_4$ZnPc	649.9	1.55	5.46 [127]	-
F$_8$ZnPc	721.8	1.55	6.30 [10]	-
F$_{16}$ZnPc	865.8	1.55	6.75 [10]	-
F$_6$-TCNNQ	362.2	1.55	-	5.5 [128]

Table 3.1: Summary of the material parameters. The material parameters used for molar mass, density, ionisation energy (IE) and electron affinity (EA) in this study. The IEs/EAs are all measured by UPS/IPES, with the references adjacent to the values.

F$_6$-TCNNQ

The chemical structure of the p-type dopant F$_6$-TCNNQ[1] is displayed in Figure 3.1e. The electron affinity (EA) of F$_6$-TCNNQ is around 5.5 eV [128], as measured with inverse photoelectron spectroscopy (IPES), and it has been shown to successfully p-dope ZnPc [81, 125, 130, 131]. The density of F$_6$-TCNNQ is unpublished and, given the high cost of the dopant, fabricating a sample to measure the density was not possible. However, at low doping concentrations, it is expected that the dopant molecules replace host molecules, preserving the overall density of the film [132]. The dopant was purchased from Novaled GmbH, and used as received.

3.2 Sample preparation

Vacuum deposition

The Evaporation CHamber Oxford 1 (ECHO1), built by CreaPhys GmbH (Dresden, Germany), was used to fabricate all samples in this thesis. Typically, it takes one hour (depending on out-gassing) for the roughing pump (ACP15, Pfeiffer GmbH) and the turbomolecular (HiPace 700, Pfeiffer GmbH) to reach a base pressure of 5×10^{-6} mbar suitable for thin film deposition. Figure 3.2 shows a sketch of co-evaporation from two sources in ECHO1. The substrate sits approximately 50 cm above the sources.

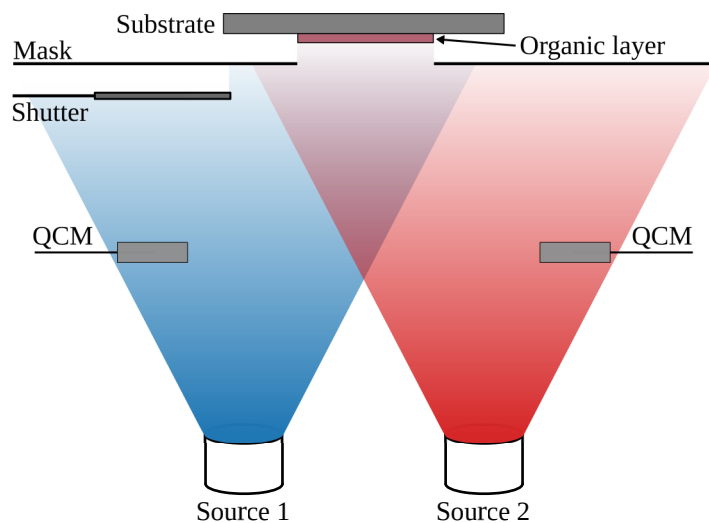[1]2,2'-(perfluoronaphthalene-2,6-diylidene)dimalononitrile

Figure 3.2: Illustration of vacuum deposition in ECHO1. Two materials are thermally sublimed from two individual sources, passing through a mask and deposited onto a substrate. Quartz crystal microbalances, positioned between the sources and the shutter, measure the rate of deposition of each material.

Located between the substrate and the sources are the masks, which allow for deposition of different layers for devices, and the substrate shutter. The substrate shutter prevents deposition on the substrate whilst the source temperatures are increased to reach the required evaporation rates and when the desired film thickness has been reached. Each organic material is placed in a ceramic crucible, which is heated by a tungsten coil to sublimation temperature, and this in turn is enclosed within a water-cooled copper shield. A thermocouple type K (MEP CreaPhys) in contact with the bottom of the crucible along with a PID controller (Eurotherm 3216), which regulates the temperature of the organic source. The sublimation temperature of small organic molecules typically lies within the range of 80 °C to 450 °C. The thickness of the film layers and the deposition rates are monitored using quartz crystal microbalances (QCMs) which are located between the sources and the shutter.

The QCMs oscillate at a specific frequency when an alternating current is applied at the electrodes. During the evaporation, the material deposited on the QCM affects the resonance resulting in a decrease of the oscillation frequency. The change in frequency can be correlated to the mass change of the crystal via the Sauerbrey equation [133] and this in turn relates to the deposition thickness using the material's

density. The deposition controller (SQC-310, Inficon) provides an interface for the QCMs, with the manufacturer stating a 5 % error in the displayed deposition rates. Typical rates used in this investigation are between $0.01\,\text{Å/s}$ to $0.40\,\text{Å/s}$. Material consumption is low (but not cheap) with $100\,\text{mg}$ of host material equating to roughly a few hundred nanometres of deposited film thickness.

Doping and mixing concentrations

Doping and mixing are performed by co-evaporating materials simultaneously from separate crucibles within ECHO1, as illustrated in Figure 3.2. In the blends, the relative content of each organic semiconductor can be expressed in terms of weight (wt%) , volume (vol%) or number of molecules (mol%). Alternatively, these measures can be written as ratios, for example, the doping concentration in molar ratio (MR) is defined as

$$\text{conc. in MR} = \frac{n_d}{n_h}, \tag{3.1}$$

where n_d is the number density of dopant molecules, and n_h is the number density of host molecules. With the assumption that the dopant replaces host molecules preserving the overall density of the film $\rho_{dopant} = \rho_{host}$, the MR can be directly calculated from the deposition rate (or thickness) measured by the QCM:

$$\text{MR} = \frac{\Gamma_d}{\Gamma_h}\frac{M_h}{M_d}, \tag{3.2}$$

where Γ_d and Γ_h are the deposition rates of the host and dopant, respectively, and M_d and M_h are the molar masses of the host and dopant, respectively. To convert MR to mol%, the following formula can be applied

$$\text{mol\%} = \frac{\text{MR}}{\text{MR} + 1} \cdot 100\%. \tag{3.3}$$

And for the conversion of MR to wt%, the formula is

$$\text{wt\%} = \left(1 + \frac{M_h}{M_d} \cdot \frac{1}{MR}\right)^{-1} \cdot 100\%. \tag{3.4}$$

Finally, it should be noted that more accurate ways of determining blend composition exist. For example, x-ray photoelectron spectroscopy (XPS) can be used to post-calibrate the concentration [67, 124], but this method was not available for the samples made in this thesis.

Undoped OFET device fabrication

Devices are fabricated in ECHO1 using pre-patterned bottom-gate bottom-contact generation 4 OFET substrates (Fraunhofer IPMS, Germany) consisting of a highly conductive n-doped silicon gate-electrode covered with 230 nm dielectric layer of thermally grown SiO_2. The gold interdigitated source-drain contacts have a thickness of 30 nm, width of 10 mm and channel lengths of 2.5, 5, 10 and 20 µm. Prior to vacuum deposition, the substrates are cleaned in an ultrasonic bath for 10 min in 2.5% Hellmanex solution, DI water, acetone and finally ethanol. The substrates are treated with O_2 plasma for 10 min prior to deposition. Films are evaporated at a base pressure of 10^{-6} mbar with a total deposition rate between 0.30 Å/s to 0.40 Å/s to achieve thicknesses around 21 nm. The samples are transferred to a nitrogen glovebox, without exposure to air, for characterisation.

Doped thin film preparation for GIWAXS, EPR, PDS

The samples are prepared in ECHO1, by triple co-evaporation of the two host materials and dopant. For these samples, the doping concentration is fixed at 0.05 MR whilst the fraction between the two host molecules ZnPc and F_8ZnPc is varied. The total deposition rate of the host semiconductor(s) is kept constant at (0.40 ± 0.02) Å/s. Prior to deposition, all the substrates are cleaned for 10 minutes in an ultrasonic bath of 2.5% Hellmanex solution, followed by DI water, acetone and finally isopropyl alcohol. The substrates are treated with O_2 plasma for 10 minutes before being loaded into the vacuum chamber.

3.3 Experimental characterisation

OFET characterisation

The electrical measurements of the OFETs are made using a Keithley 2636B (Tektronix, US) source measurement unit (SMU), as shown in the circuit diagram of Figure 3.3. The substrates are contacted using an OFET Measurement Adapter (Fraunhofer IPMS, Germany). The SMU is controlled by software developed as part of this thesis, and is available under an MIT licence online [134].

GIWAXS

X-ray diffraction experiments provide information on the structural arrangement of a film, through elastic scattering of the incident beam by the atoms of the sample. Atomic or molecular planes in the sample cause diffraction of the incident beam, with constructive interference of reflections leading to bright spots of high intensity on the detector. The angle at which diffraction occurs relates to the plane spacing, while the direction of the diffracted beam relates to the plane orientation [135]. The scattering vector magnitude is given by

$$q = \left(\frac{4\pi}{\lambda}\right)\sin\theta, \tag{3.5}$$

where λ is the wavelength of the incident X-rays and 2θ is the scattering angle. The spacing between the planes $d_{h,k,l}$, labelled with the Miller indices h, k, l, is obtained via the Bragg condition

$$q = q_B = \frac{2\pi}{d_{h,k,l}}, \tag{3.6}$$

which applies when the scattering vector is orthogonal to the lattice planes $q = q_B$.

A typical diffraction experiment is shown in Figure 3.4. The scattering vector normal to the sample is labelled Q_z, and represents the periodicity out of the substrate plane. Q_{xy} is the scattering vector along the sample plane, and represents planes perpendicular to the sample plane. Typically in grazing incidence wide-angle X-ray scattering (GIWAXS), the sample to detector ratio L is between $0.3\,\mathrm{m}$ to $1\,\mathrm{m}$, corresponding to angles approximately $1°$ to $45°$ and size scales of $0.5\,\mathrm{nm}$ to $10\,\mathrm{nm}$ [135].
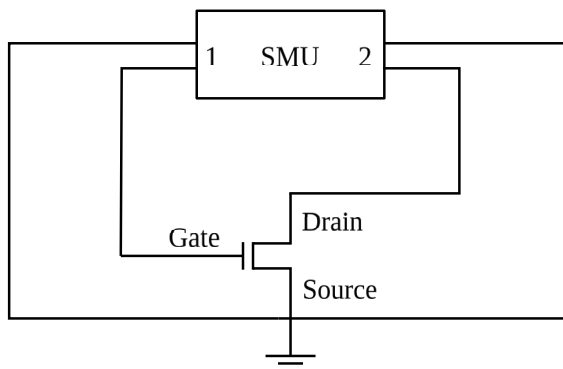
Figure 3.3: Circuit diagram of OFET characterisation. A two channel source measurement unit (SMU) is connected to the three-terminal organic field-effect transistor. The two channels share a non-floating common ground, with one channel setting the gate voltage, and the other controlling the voltage across the source and drain.
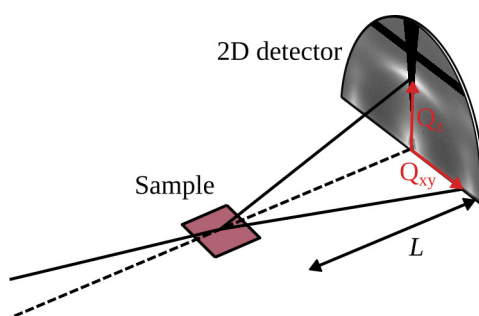

Figure 3.4: Schematic for grazing incident wide-angle X-ray scattering. For GIWAXS imaging of organic thin films, the sample to detector distance is typically $L \approx 0.3\,\mathrm{m}$ to $1\,\mathrm{m}$. Schematic adapted from reference [135].

GIWAXS studies are carried out at the Surface and Interface Diffraction beamline (I07) at the Diamond Light Source (DLS) using a beam energy of 20 keV (0.62 Å) and a Pilatus2M area detector. The samples are probed while inside a vacuum deposition chamber at a pressure of around 10^{-3} mbar with the MINERVA setup [136]. The sample-to-detector distance was 42.1 cm as determined via AgBeh calibration. Images are converted to 2D reciprocal space using the DAWN software package with an applied polarisation and solid angle correction. For further information on the image conversion, the interested reader is referred to reference [137]. In Chapter 4 and Chapter 5, the GIWAXS measurements are performed in collaboration with Dr Josue F. Martinez Hardigree and Mr Andreas E. Lauritzen (University of Oxford, UK).

Electron paramagnetic resonance spectroscopy

Electron paramagnetic resonance (EPR) is a spectroscopic technique used to study unpaired electronic spins, via the *Zeeman effect*. In the presence of an external magnetic field B_0, the magnetic moment of an unpaired electron will either align itself parallel ($m_s = -1/2$) or antiparallel ($m_s = +1/2$) to the field. Each state ($m_s = \pm 1/2$) has a specific energy, with the difference between them given by

$$\Delta E = g\mu_b B_0 = h\nu, \tag{3.7}$$

where g is the electron g-factor and μ_b is the Bohr magneton. This energy difference can be probed using electromagnetic radiation, usually in the range of microwaves. The resonance condition is fulfilled when a photon has an energy $h\nu$ equal to the splitting caused by the Zeeman effect. In this case, the photon is absorbed, as shown in Figure 3.5. Experimentally, the frequency of the microwave radiation is kept constant and the external magnetic field strength is varied. The first derivative of the absorption spectrum is typically reported, with an example shown in the lower part of Figure 3.5.

EPR measurements are made on thin films of 50 nm thickness deposited on microscope cover glass, cut to a width of 3 mm with a diamond tipped glass cutter. The samples are placed in quartz EPR tubes which are sealed in a nitrogen glovebox,
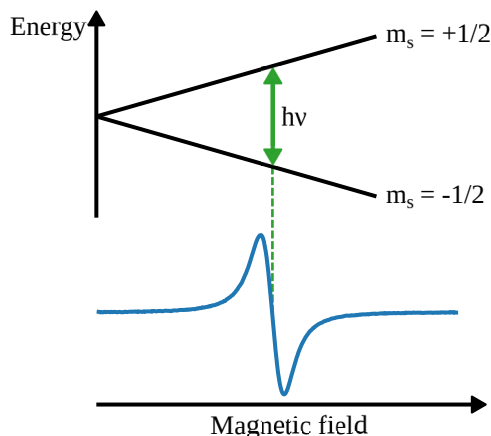
Figure 3.5: Zeeman splitting and the EPR spectrum. Energy level diagram for an $S = 1/2$ paramagnetic species as a function of applied magnetic field, and the corresponding first-derivative of the EPR spectrum in response to the resonance field. Diagram inspired from reference [138].

such that all EPR measurements are made without air exposure. The continuous wave EPR spectra are recorded on a Bruker Elexsys E680 X-band spectrometer with a nitrogen gas-flow cryostat for sample temperature control. The experimental parameters were set with an amplitude modulation $= 1\,\mathrm{G}$ and microwave power $= 0.2\,\mathrm{mW}$ ($30\,\mathrm{dB}$ attenuation). Spectral simulations are performed using routines of Easyspin [139]. The EPR measurements are performed at the Centre for Advanced ESR (CAESR), located in the Department of Chemistry of the University of Oxford, in collaboration with Dr Alberto Privitera (University of Oxford, UK).

Photothermal deflection spectroscopy

Photothermal deflection spectroscopy (PDS) is based on illuminating a sample that sits in a cuvette containing a liquid whose refractive index depends on temperature. The monochromatic light heats the sample and creates a temperature gradient in the liquid. This heating results in a refractive index gradient, causing the deflection of a probe laser passing through the cuvette. A photodetector measures the amount of deflection, which is proportional to the amount of absorbed light and therefore the absorptance of the sample. The absorption coefficient may then be obtained, if the film thickness is known. A schematic drawing of a typical PDS setup is shown in
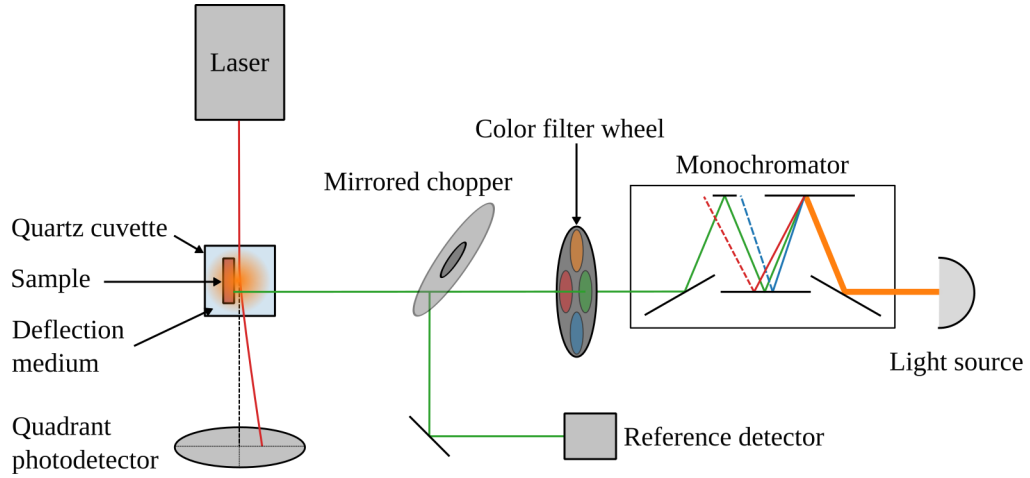
Figure 3.6: Schematic of a typical PDS setup. The sample is emersed in a deflection medium within a quartz cuvette, and illuminated by monochromatic light. A quadrant photodetector measures the deflection of the probe laser. Schematic redrawn from reference [140].

Figure 3.6.

PDS measurements have a much greater dynamic range than normal transmission-reflection measurements, such as UV-vis absorption. In a UV-vis measurement, the absorptance a of a semiconductor film is determined through measurements of the transmittance T and reflectance R,

$$a(E) = 1 - T(E) - R(E), \qquad (3.8)$$

as a function of photon energy (E). For films of low absorptance and/or measurements within an energy gap, the sum of the reflectance and transmittance will be close to one. Errors in either of these measurements leads to a large degree of uncertainty in calculating the absorptance. PDS overcomes this limitation by measuring the absorption directly.

For the PDS measurements in Chapter 5, the samples are $40\,\mathrm{nm}$ thick and are deposited on quartz substrates, mounted in a cuvette containing the liquid CCl_4. The PDS data is compared and scaled using transmission-reflection measurements, in the energy range of strong absorption (the first Q-band peak of the zinc-phthalocyanine). The PDS measurements are made by Mr Oliver Thimm (Forschungszentrum Jülich, Germany).

3.4 Theoretical methods

Density functional theory

Density functional theory (DFT) is a computational technique for solving the many body Schrödinger equation, to evaluate a molecule's electronic structure, and predict material properties. In this thesis, DFT calculations were performed using the quantum chemical package Gaussian 09, [141] with the Becke, three-parameter, Lee-Yang-Parr (B3LYP) exchange correlation functional [142–145], and the 6-311g+(d,p) basis set [146, 147].

Statistical model

The statistical model presented in Chapter 5 is written in python3 and is available online [148].

4. Energy level tuning in OFETs

4.1 Introduction

Most organic devices rely upon energy level alignment at the interfaces between layers, particularly for achieving Ohmic injection at the contacts. In this chapter, the effect of a semiconductor's energy levels on charge transport in organic field-effect transistors (OFETs) is investigated. Devices are fabricated based on zinc-phthalocyanine (ZnPc) and its fluorinated derivatives (F_xZnPc, $x = 4, 8, 16$), with the ionisation energy (IE) of the films increasing with greater fluorination [8, 149]. First, pristine (unmixed) films are investigated in Section 4.2. ZnPc and F_4ZnPc show p-type behaviour, whilst F_8ZnPc and F_{16}ZnPc show n-type behaviour. The charge carrier mobility in the films tend to decrease with increasing fluorination, which can be partly attribute to changes in morphology and to contact resistances at the source and drain electrodes.

In Section 4.3, the effects of energy level tuning in ZnPc:F_8ZnPc blends is extended to OFETs. The semiconducting behaviour of the blends can be tuned continuously from unipolar p-type, to ambipolar, and finally to unipolar n-type depending on the composition ratio. Using this mixing technique, a balance between the hole and electron mobilities is struck. Balanced transport enables fabrication of complementary logic based on the deposition of only one semiconductor. A voltage inverter circuit is shown as an example in Section 4.4. This section is published as Warren P. R. *et al.* Tuning the ambipolar behaviour of organic field effect transistors via band engineering. *AIP Advances* **9,** 035202 (2019).

4.2 Pristine ZnPc and F_xZnPc OFETs

Figure 4.1 shows the output and transfer characteristics of the OFETs fabricated in bottom-contact, bottom-gate geometry, with the substrate held at room temperature during deposition and measurements. Both the ZnPc and F_4ZnPc show unipolar hole transporting behaviour, which is termed *p-type*. At negative gate voltages V_g, holes accumulate at the semiconductor/SiO$_2$ interface, creating a conductive channel along which a source-drain current I_{ds} flows. In contrast, with a positive V_g, holes are repelled from the interface and I_{ds} drops by several orders of magnitude. For F_8ZnPc, the majority carriers across the semiconducting channel are electrons. Therefore the opposite (*n-type*) behaviour is observed in the output and transfer curves - the devices switch off at negative V_g, and on at positive V_g. For F_{16}ZnPc a larger current is measured for positive V_g than negative, suggesting n-type behaviour. However there is also an appreciable hole current at negative V_g. Thus F_{16}ZnPc shows ambipolar behaviour, that is the conduction of both holes and electrons. It should however be noted that these ambipolar currents in F_{16}ZnPc are small as compared to the other devices, particularly the hole current in the range of tens of nanoamps.

The field-effect mobilities μ for the devices as a function of the number of fluorine atoms x in F_xZnPc are shown in Figure 4.2. The mobilities are calculated in both the linear and saturation regimes. In the saturation regime, the measured hole mobilities for ZnPc and F_4ZnPc are $(1.5 \pm 0.3) \times 10^{-4}\,\mathrm{cm^2V^{-1}s^{-1}}$ and $(2.4 \pm 0.8) \times 10^{-4}$ $\mathrm{cm^2V^{-1}s^{-1}}$, respectively, which are in good agreement with measurements made using a similar geometry in literature [10, 120]. The charge carrier mobility decreases by an order of magnitude from F_8ZnPc, which has an electron mobility of $(1.1 \pm 0.2) \times 10^{-4}$ $\mathrm{cm^2V^{-1}s^{-1}}$, to F_{16}ZnPc, with an electron mobility of $(1.3 \pm 0.4) \times 10^{-5}\,\mathrm{cm^2V^{-1}s^{-1}}$, again in good agreement with literature [117]. Overall, there appears to be decreasing trend in charge carrier mobility as the level of fluorination increases. However with the uncertainty, estimated as the standard deviation over eight measurements (forward and reverse scans) on 4 individual devices fabricated in the same deposition run, the charge carrier mobility of ZnPc, F_4ZnPc and F_8ZnPc are similar, only the
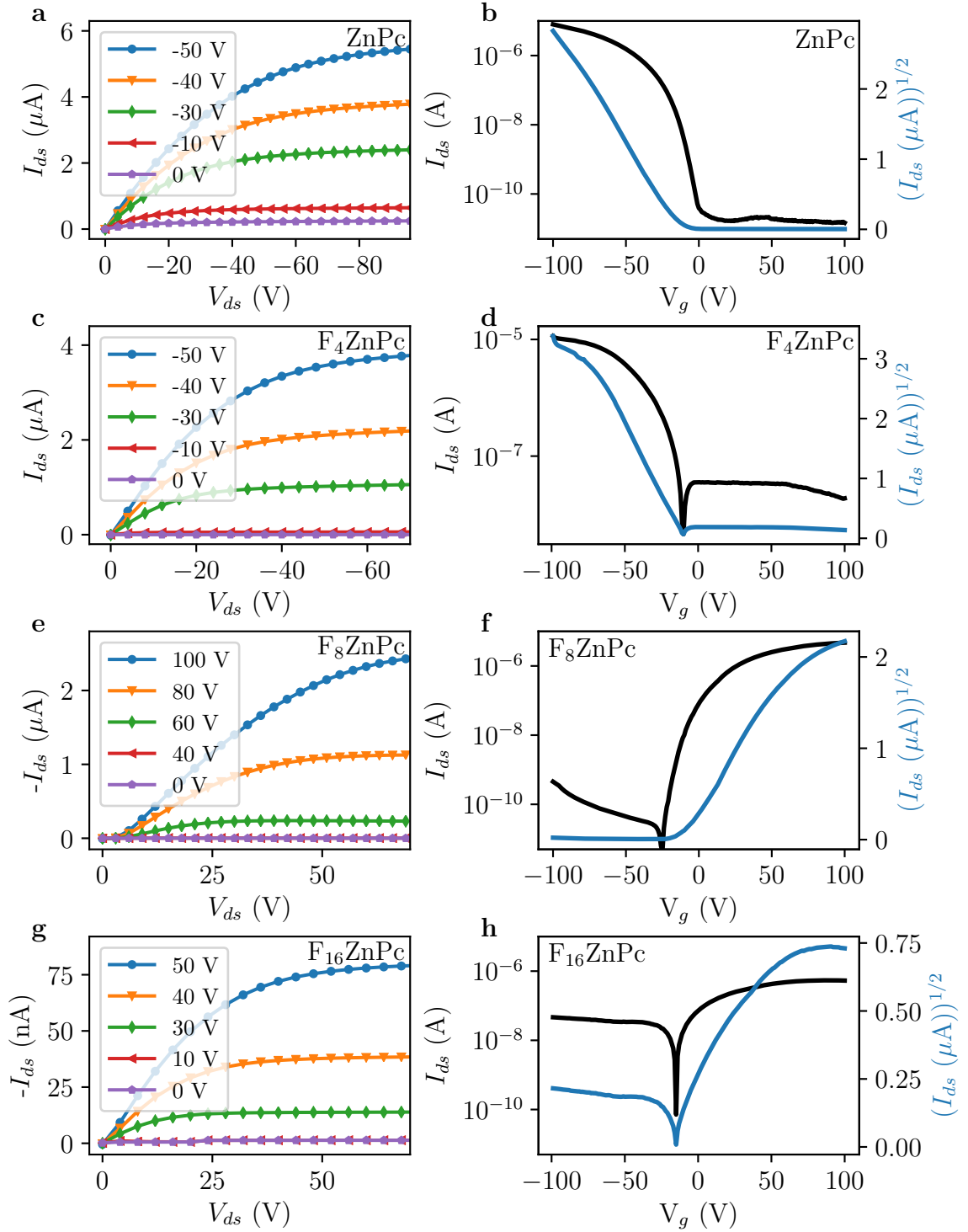
Figure 4.1: Output and transfer sweeps of blends of pristine OFET devices.
(a, c, e, g) Output (I_{ds} against V_{ds}) for a range of gate voltages V_g and **(b, d, f, h)** transfer characteristics (I_{ds} and $\sqrt{I_{ds}}$ against V_g, with $V_{ds} = -50\,\text{V}$) of pristine **(a, b)** ZnPc, **(c, d)** F_4ZnPc, **(e, f)** F_8ZnPc and **(g, h)** F_{16}ZnPc, all with channel length $10\,\mu\text{m}$.
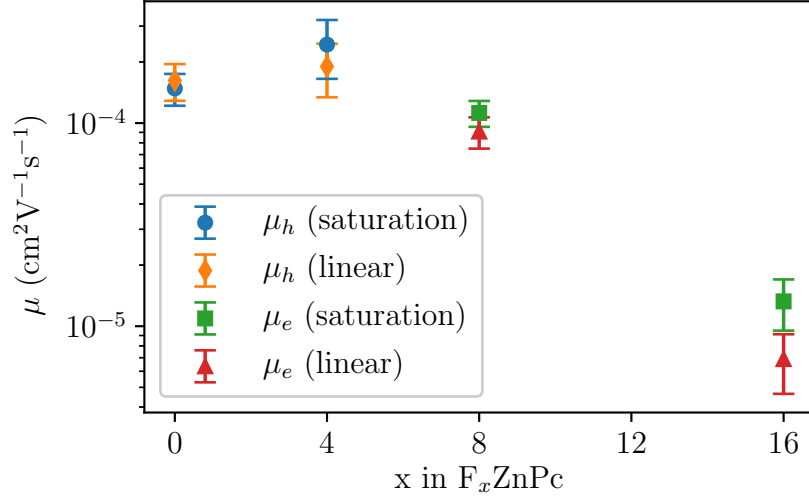
Figure 4.2: Field-effect mobility of the pristine OFETs. Field-effect mobility μ extracted in the OFET saturation and linear regimes with channel length of 10 µm, plotted against the number of fluorine atoms x in F_xZnPc. Error bars given represent the standard deviation of mobilities measured over four devices, scanned in both directions, from the same deposition run.

electron mobility of F_{16}ZnPc shows a significant deviation of a one order of magnitude decrease.

4.2.1 Contact effects

Variations in OFET mobility are often attributed to charge injection and charge transport through the semiconductor. Here, the height of the Schottky barrier at the interface between the gold contacts and semiconducting material depends upon fluorination of the ZnPc. With increasing fluorination, the ionisation energy (IE) and electron affinity (EA) of the semiconductor increase in magnitude [149]. The energy levels are sketched in Figure 4.3, with the values for IE and EA (for ZnPc only) taken from the references as per Table 3.1 in the methods section. For the fluorinated phthalocyanines, the EAs are estimated as the IE plus a fundamental gap approximated to be equal to that measured for ZnPc. Therefore, the Schottky barrier for hole injection, estimated as $\phi_h = IE - W_f$, increases with increasing fluorination. In contrast, the barrier for electron injection $\phi_e = W_f - EA$ decreases. The estimated barriers are summarised in Table 4.1. From these values, it appears that a barrier

height of 0.6 eV or less allows for hole injection in ZnPc and F_4ZnPc, and electron injection in F_8ZnPc and F_{16}ZnPc.

The barrier for hole injection in F_4ZnPc is larger than that for ZnPc. Similarly, the barrier for electron injection in F_8ZnPc is larger than that for F_{16}ZnPc. The larger barrier is evident in the output characteristics of F_8ZnPc, particularly at lower channel channel lengths as shown in Figure 4.4. As the channel length decreases ($L = 20$, 10, 5 and 2.5 μm), contact effects play a greater role and nonlinear behaviour around the origin becomes more pronounced. The nonlinear behaviour around the origin can be reproduced by considering anti-parallel Schottky diodes at both electrodes (see Section 2.3.2).

The contact resistance is experimentally determined via the transmission line method (TLM) using the transfer characteristics of devices with different channel lengths. With the assumption that the resistance at the source and drain contacts is independent of the potential drop across the device, the contact resistance can be estimated using a linear regression analysis on the total device resistance R_{tot}, defined in the linear regime as

$$R_{tot} = \left.\frac{\partial V_{ds}}{\partial I_{ds}}\right|_{V_{ds}}^{V_g} = \frac{L}{\mu C_{ox} W (V_g - V_T)} + R_c^{TLM} \tag{4.1}$$

where R_c^{TLM} is the total contact resistance, that is the source resistance plus the drain resistance. Figure 4.5a shows F_{16}ZnPc as an example of the data used for estimating the (electron) contact resistance, over a range of V_g in the linear regime (small V_{ds}). The gradient of the straight line fit gives the channel resistance per channel length, and the intercept at channel length $L = 0$ provides the estimate of contact resistance. Figure 4.5b and Figure 4.5c show the gate-voltage dependence of the contact resistance, as estimated from the linear and saturation regime, respectively. This dependence has also been observed in a number of previous reports [109, 151, 152]. As V_g increases, a greater number of charge carriers accumulate at the dielectric-semiconductor interface, including adjacent to the contacts. In a rectifying Schottky contact, the increase in charge carrier density leads to a decrease in the depletion width. Thus, the contact resistance is expected to decrease with increasing
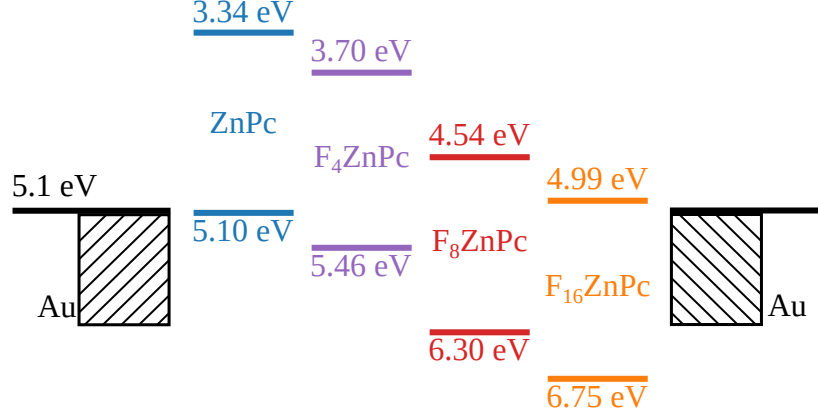
Figure 4.3: Schematic energy level diagram of the ZnPc and F_xZnPc OFETs. The IE values are taken from UPS measurements on thin films with edge-on orientation from reference [10]. The EA of ZnPc was measured by IPES in reference [71]. The EA's of the fluorinated phthalocyanines are estimated by adding a fundamental gap, which is approximated as equal to that measured for ZnPc. The gold work function W_f was measured in [150].

	ϕ_h (eV)	ϕ_e (eV)	$R_c^{TLM} W$ (MΩ cm)	$R_c^{M\text{-}TLM} W$ (MΩ cm)
ZnPc	0.0	1.8	-8.6 ± 5.0	-3.1 ± 2.4
F$_4$ZnPc	0.4	1.4	0.6 ± 1.3	-1.2 ± 1.2
F$_8$ZnPc	1.2	0.6	17000 ± 4000	16000 ± 3000
F$_{16}$ZnPc	1.7	0.1	260 ± 100	170 ± 40

Table 4.1: Estimated Schottky barriers and contact resistances. A table summarising the estimated Schottky barriers for hole $\phi_h = IE - W_f$ and electron injection $\phi_e = W_f - EA$, alongside the contact resistance R_c^{TLM} as measured using the transmission line method (TLM) and the modified-TLM $R_c^{M\text{-}TLM}$ in the linear regime, with $|V_{ds}| = 4\,\text{V}$ and $|V_g| = 40\,\text{V}$. The contact resistance refers to holes for the p-type devices, and electrons for the n-type.
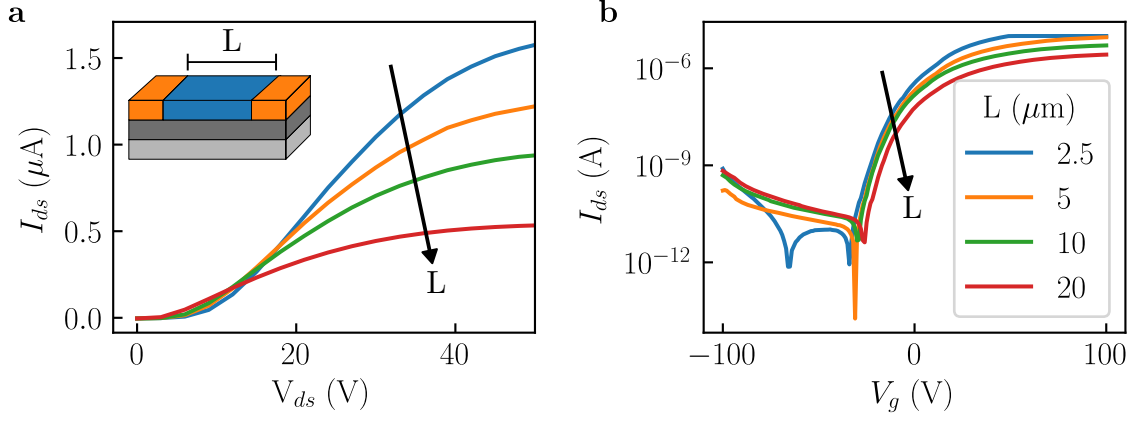
Figure 4.4: Channel length effect in the output and transfer curves. The output **(a)** and transfer **(b)** curves of an F_8ZnPc TFT with different channel lengths L (dimension shown in inset) from $2.5\,\mu m$ to $20\,\mu m$.
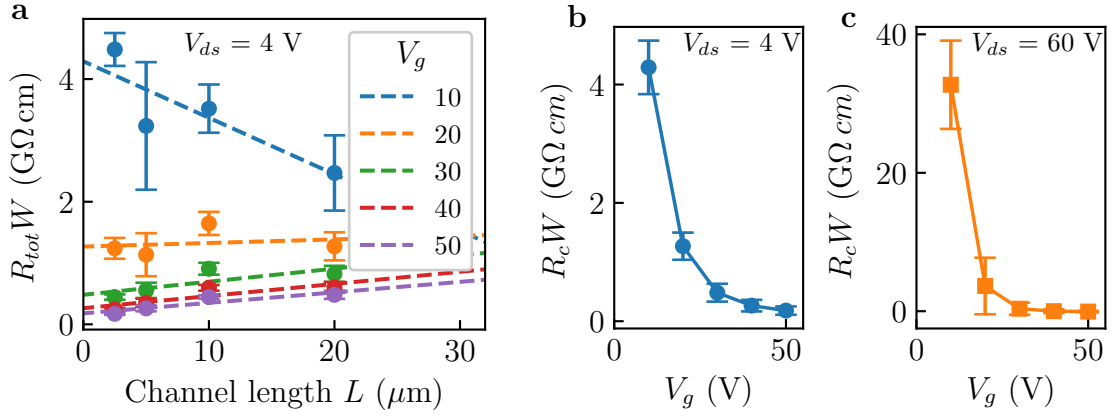

Figure 4.5: OFET contact resistance. **(a)** Total device resistance per channel width $R_{tot}W$ versus the channel length L at various gate voltages V_g and fixed source drain voltage $V_{ds} = 4\,V$ for $F_{16}ZnPc$ OFETs. The error bars represent the standard deviation over four devices. **(b)** The contact resistance as estimated from the linear regime ($V_{ds} = 4\,V$) plotted against V_g. **(c)** The contact resistance as estimated from the saturation regime ($V_{ds} = 60\,V$) plotted against V_g.

V_g. Also worth noting is that the standard deviation of the contact resistance over four devices increases at lower V_g. This is symptomatic of measurements and analysis performed at low V_g (typically around the threshold voltage $V_g \approx V_T$) which tends to have greater sensitivity to parameter dispersion in μ, C_{ox} and V_T, from device to device [109]. Finally, the contact resistance is an order of magnitude larger when estimated from the saturation regime. This is likely due to the separation of the conductive channel from the drain electrode caused by channel pinch-off [108].

The contact resistances R_c^{TLM} for ZnPc, F_4ZnPc, F_8ZnPc and F_{16}ZnPc in the linear regime with $|V_{ds}| = 4\,\mathrm{V}$ and $|V_g| = 40\,\mathrm{V}$ are summarised in Table 4.1. The estimated values vary over several orders of magnitude with large associated uncertainties. A similarly broad range of contact resistances was also observed by Bürgi et al. when examining polymer OFETs with different electrode materials [102]. The decrease in contact resistance from F_8ZnPc to F_{16}ZnPc correlates with the change in injection barrier height, however for the case of ZnPc to F_4ZnPc, the negative contact resistance found for ZnPc limits the analysis. Other than the large uncertainty involved in extrapolating the linear fits, another possible reason for finding a negative contact resistance includes underestimation of the effective channel length, which is a well-known issue in the CMOS community [153, 154]. Readers interested in measuring the effective channel length are referred to reference [155].

To reduce the large uncertainties and address negative contact resistances found using conventional TLM, Xu et al. [109] proposed a modified-TLM (M-TLM) to improve extraction accuracy. In this approach, both sides of Equation (4.1) are divided by the channel length L. The linear regression is then performed on a plot of $R_{tot}W/L$ against inverse channel length $1/L$. The gradient of the fit is then determined by the contact resistance rather than the channel resistance. As the contact resistance generally shows less device to device variation than the channel resistance, linear fits can be made with less associated uncertainty. The contact resistances $R_c^{M\text{-}TLM}$ found using this method are shown in Table 4.1. ZnPc and F_4ZnPc show values of similar magnitude for their contact resistance, although the method still gives negative

resistances. A similar trend to conventional TLM of decreasing contact resistance is observed from F_8ZnPc to $F_{16}ZnPc$.

4.2.2 Structural characterisation

The barriers hindering charge transport may arise in the bulk semiconductor itself, as well as at the contacts. Trap states can be introduced through structural inhomogeneities, such as grain boundaries, which result in band bending and barriers [156, 157]. Interestingly, OFET mobility measurements, on surface-treated SiO_2 substrates with gold contacts, in single crystals of these materials show a different trend of decreasing mobility from ZnPc to F_4ZnPc, then increasing from F_8ZnPc to $F_{16}ZnPc$ [119]. As compared to the single crystals, the mobilities in the polycrystalline films presented here are roughly three orders of magnitude lower. A similar drop in mobility was observed by Bolognesi et al. as the grain size in pentacene thin films decreased [158].

Grazing incidence wide angle scattering (GIWAXS) measurements are presented to investigate the crystalline structure of the samples.[1] Figure 4.6 shows the 2D reciprocal space maps of ZnPc, F_4ZnPc, F_8ZnPc and $F_{16}ZnPc$, deposited on SiO_2, the same surface as the OFETs. The films display two preferred grain orientations, either fully in-plane or out-of-plane, as seen by the (200) reflections. The out-of-plane peak is more intense, indicating a preference for edge-on orientation as opposed to face on [159]. This preferential ordering is greatest for ZnPc, with the fluorinated films appearing more powder-like, which suggests a broader distribution of grain orientations. Poorly orientated domains can result in high-angle grain boundaries, which are detrimental to charge transport [135, 160]. Thus, a decrease in mobility may be expected with the addition of fluorine atoms to ZnPc.

Line cuts are made in the near out-of-plane direction through the (200) Bragg peak using a simple sector integration between $7°$ and $8°$ from the out-of-plane axial orientation. The location of the peaks and corresponding d-spacing values are shown

---

[1]GIWAXS measurements were performed by Dr Josue F. Martinez Hardigree and Mr Andreas E. Lauritzen (University of Oxford, UK).
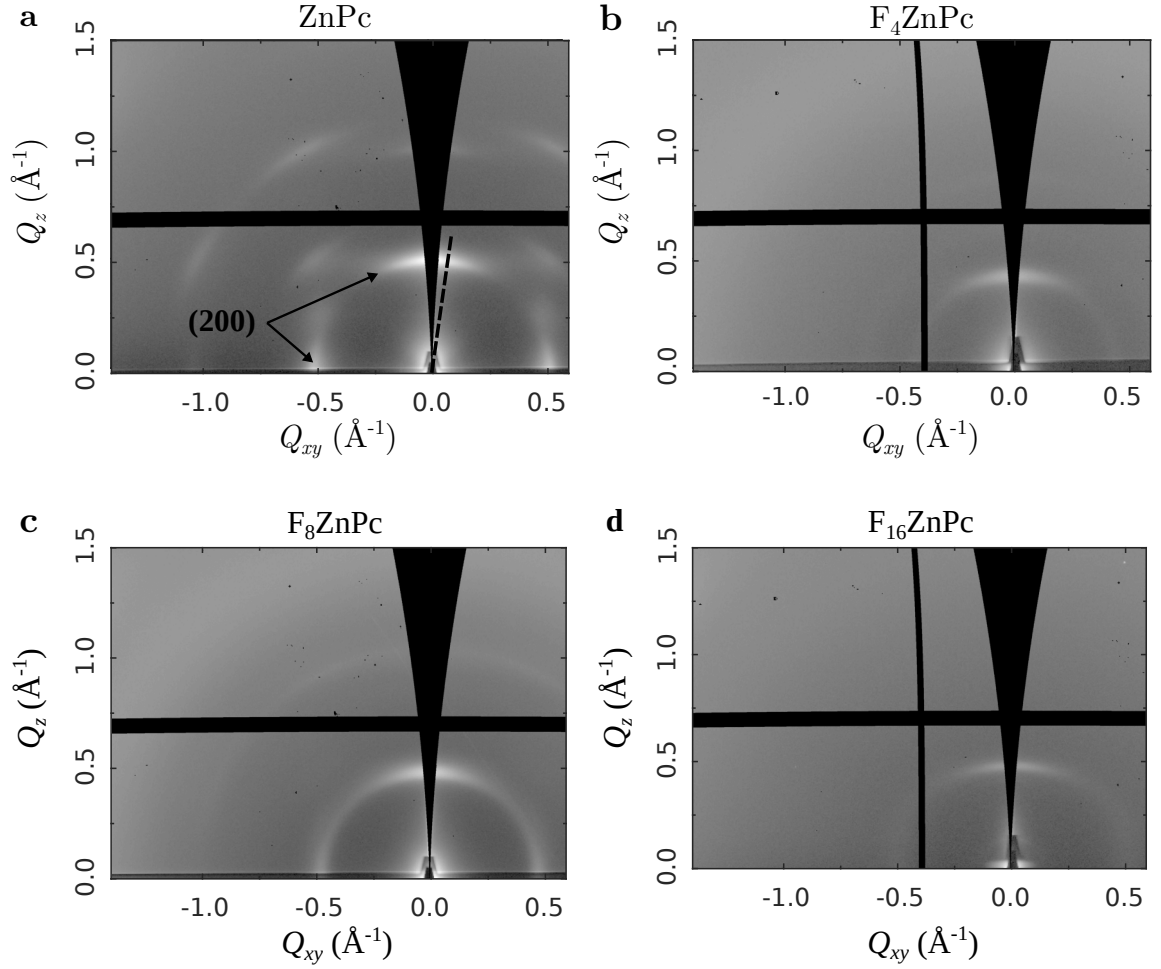
Figure 4.6: GIWAXS images of pristine films. **(a)** ZnPc **(b)** F_4ZnPc **(c)** F_8ZnPc and **(d)** F_{16}ZnPc evaporated on SiO_2, like the OFETs. For ZnPc in **(a)**, the (200) peaks are indicated. Line cuts are made in the near out-of-plane direction through the (200) Bragg peak using a simple sector integration between 7° and 8° from the out-of-plane axial orientation. Because of time constraints leading to alignment issues at the beam line, the images for F_4ZnPc and F_{16}ZnPc images are of lower quality.

	Q (Å^{-1})	d_{200}-spacing (Å)
ZnPc	0.503	12.5
F$_4$ZnPc	0.427	14.7
F$_8$ZnPc	0.476	13.2
F$_{16}$ZnPc	0.475	13.2

Table 4.2: GIWAXS peak fits and d-spacing of the pristine films. Q-values derived from fitted line cuts through 2D GIWAXS images (Figure 4.6) in the near out-of-plane direction through the (200) Bragg peak using a simple sector integration between 7° and 8° from the out-of-plane axial orientation.

in Table 4.2. ZnPc has the smallest d-spacing of 12.5 Å, consistent with previously reported values for thermally evaporated thin films [161], while F$_4$ZnPc has the largest of 14.7 Å. F$_8$ZnPc and F$_{16}$ZnPc have similar d-spacings of 13.2 Å. The d-spacings do not correlate directly with the degree of fluorination, although the fluorinated species all having a larger d-spacing is in agreement with literature [10, 118].

From Equation (2.16), the mobility is directly dependent on the square of the hopping distance between the intermolecular sites. Therefore, the larger d-spacing may relate to a reduction in the charge mobility in the out-of-plane direction. Taking the ratio of the squares of the d-spacing for ZnPc and F$_{16}$ZnPc, the mobility of F$_{16}$ZnPc would be 90 % that of the ZnPc, which is a significant underestimation of the measured change. There are several reasons leading to this underestimation. Firstly, there are multiple terms in Equation (2.16) which also have a spatial dependence, particularly the electronic coupling term [162, 163], and the reorganisation energy [164]. Secondly, this oversimplified calculation does not account for the distribution of grain orientations observed in the GIWAXS images. Finally, it should be noted that GIWAXS diffraction provides information on the bulk material rather than at the conductive channel along the semiconductor/dielectric interface. To clarify the structure at the interface, further measurements such as *in-situ* GIWAXS are required.
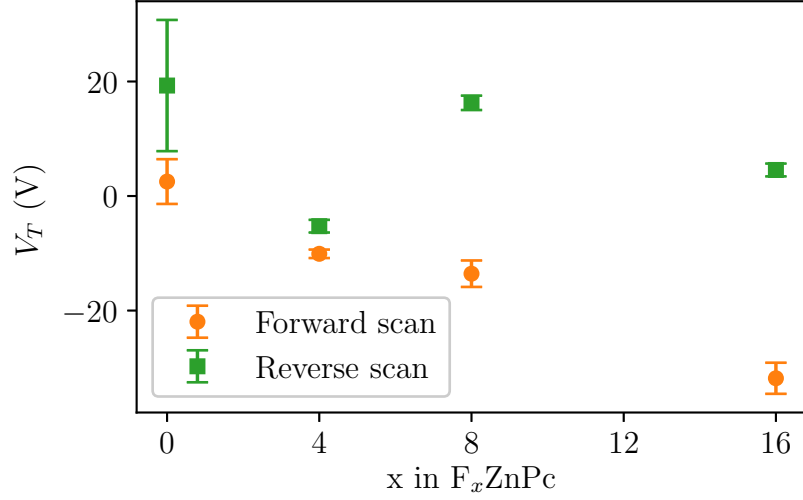
Figure 4.7: Threshold voltages against degree of fluorination. threshold voltage V_T of the OFETs measured in a forward (orange circles) and reverse scan (green squares). Error bars given represent the standard deviation measured over four devices from the same deposition run.

4.2.3 Threshold voltage

Figure 4.7 shows the the threshold voltage V_T measured in a forward and reverse scan direction, against the number of fluorine atoms on the phthalocyanine molecular structure. There appears a general trend of decreasing V_T as the degree of fluorination increases. As V_T is proportional to the number of immobile trap states within the gradual channel approximation (Equation (2.36)), the trend in the forward scan suggests that the number of trap states increases with fluorination. In combination with the GIWAXS images in Figure 4.6, this could point towards an increase of trap states at the interface between poorly aligned grains.

4.2.4 Device hysteresis

Figure 4.8 shows the dependence on scan direction of the OFET transfer characteristics, when scanned at a rate of $5\,\mathrm{V/s}$. During a scan, each measurement point depends on the previous data point, such that the forward scans produce different results to the reverse scans. OFET hysteresis has been widely reported in the literature [165, 166], with possible origins including the thermalisation of trap states at the semicon-
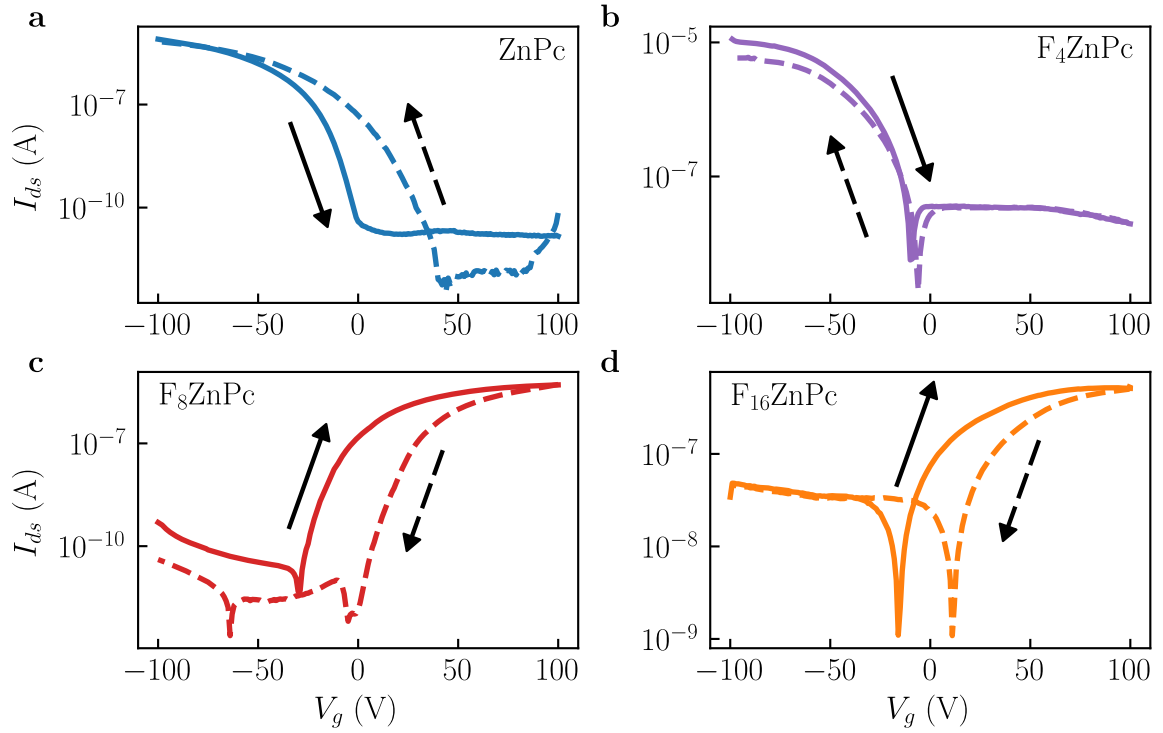
Figure 4.8: Device hysteresis in the transfer characteristics. Transfer sweeps scanned from negative to positive (solid lines) and positive to negative (dashed lines) for pristine OFETs of **(a)** ZnPc, **(b)** F_4ZnPc, **(c)** F_8ZnPc and **(d)** F_{16}ZnPc. All devices have a channel length of $10\,\mu m$ and the scan rate is $5\,V/s$. The hysteresis loops are stable over multiple successive sweeps.

ductor/dielectric interface [167, 168], and the movement of ions in the gate dielectric [169].

For p-type ZnPc, the hysteresis turns counterclockwise, such that the sweep from the on-to-off state (back sweep) shows a lower current than the forward sweep. For F_4ZnPc, it is difficult to resolve the hysteresis, whereas for F_8ZnPc and $F_{16}ZnPc$, the hysteresis direction is clockwise. Because F_8ZnPc and $F_{16}ZnPc$ show n-type behaviour, this means that the back sweep (on-to-off state) current is again lower than the forward sweep current. Lower back sweep currents have been linked to traps located in the semiconductor, close to the dielectric interface [170], whereas higher back sweep currents have been attributed to the dielectric itself, either from the movement of ions or from ferroelectric polarisation [168, 169]. Further time-dependent measurements (e.g. varying the scan rate) are necessary in order to clarify the depth and origin of these traps.

Finally, it should be noted that the peculiar shape seen in the back sweep direction in the F_8ZnPc device in Figure 4.8c is a result of the electron current switching off at around $0\,V$ and a hole current switching on at around $-60\,V$, an effect which has been observed commonly in OFETs [103, 171]. Between these two points, the measured current through the conductive channel is below the resolution of the source-measurement unit. With greater resolution, one would expect to see these two points converge and the transfer curve to have a similar shape as the rest of the devices.

4.2.5 Summary

In this section, the hole and electron mobilities in OFETs of ZnPc and its fluorinated derivatives F_xZnPc (with $x = 4, 8, 16$) were investigated. It was found that as the number of fluorine atoms in the molecule increases, the behaviour of the OFET shifts from unipolar p-type, that is charge transport via holes, to unipolar n-type, with electrons as the majority carrier. The charge carrier mobility in the films tended to decrease with increasing fluorination, with ZnPc showing a hole mobility of $(1.5 \pm 0.3) \times 10^{-4}\,cm^2V^{-1}s^{-1}$, and $F_{16}ZnPc$ showing an electron mobility one order of magnitude smaller, at $(1.3 \pm 0.4) \times 10^{-5}\,cm^2V^{-1}s^{-1}$. This decrease was partly

attributed to changes in morphology, and to contact effects at the source and drain electrodes. A broader distribution of grain orientations, for films of the fluorinated molecules, as observed via GIWAXS experiments, along with shifting threshold voltages and large device hysteresis, points to the presence of traps in the semiconducting films.

4.3 ZnPc:F$_8$ZnPc OFETs

Having established that ZnPc and F$_4$ZnPc show p-type behaviour while F$_8$ZnPc and F$_{16}$ZnPc show n-type behaviour, the question emerges - what happens when we blend these semiconductors? As the electron mobility for F$_8$ZnPc is greater than F$_{16}$ZnPc, we investigate blends of ZnPc:F$_8$ZnPc.

Figure 4.9 shows the output and transfer characteristics of OFETs fabricated with blends of ZnPc:F$_8$ZnPc of weight ratios of 1:0 (pristine ZnPc), 1:1, 1:1.5 and 0:1 (pristine F$_8$ZnPc). Recapping from the previous section, ZnPc shows unipolar p-type behaviour whereas F$_8$ZnPc shows unipolar n-type behaviour. The current on/off ratio for each of these single-component devices is $\approx 10^5$.

For the blended films we observe conduction of both holes and electrons. With negative gate bias, V_g, holes accumulate at the semiconductor/SiO$_2$ interface and the device works as a p-type OFET. Whereas for positive V_g, electrons accumulate at the interface and the device operates as an n-type OFET. For the 1:1.5 blend, the output curves for $V_g = 0\,\text{V}$ and $-10\,\text{V}$ show a marked increase of the source-drain current I_{ds} with increasingly negative V_{ds} which is typical of ambipolar devices due to the contribution of drain-induced holes [118, 172]. The transfer curves shows a reduced I_{ds} for only a narrow range of V_g, giving an on/off ratio in the range of 10^3.

The field-effect mobilities for the devices as a function of blend ratio are shown in Figure 4.10. The mobilities are calculated in the linear and saturation regime from the gradient of the straight line fit of $\sqrt{I_{ds}}$ vs V_g. At a blend ratio 1:1.5, ambipolar behaviour is observed and the hole and electron mobility are found to be $(8.3 \pm 0.2) \times 10^{-7}\,\text{cm}^2\text{V}^{-1}\text{s}^{-1}$ and $(5.5 \pm 0.1) \times 10^{-7}\,\text{cm}^2\text{V}^{-1}\text{s}^{-1}$, respectively. The linear regime mobilities follow a similar trend to that observed for the saturation regime mobilities.

The mobilities and the measurement reliability factors r are summarised in Table 4.3 and Table 4.4 for holes and electrons, respectively. The measurement reliability factor aims to assess how well the OFETs follow the ideal field-effect equations, those
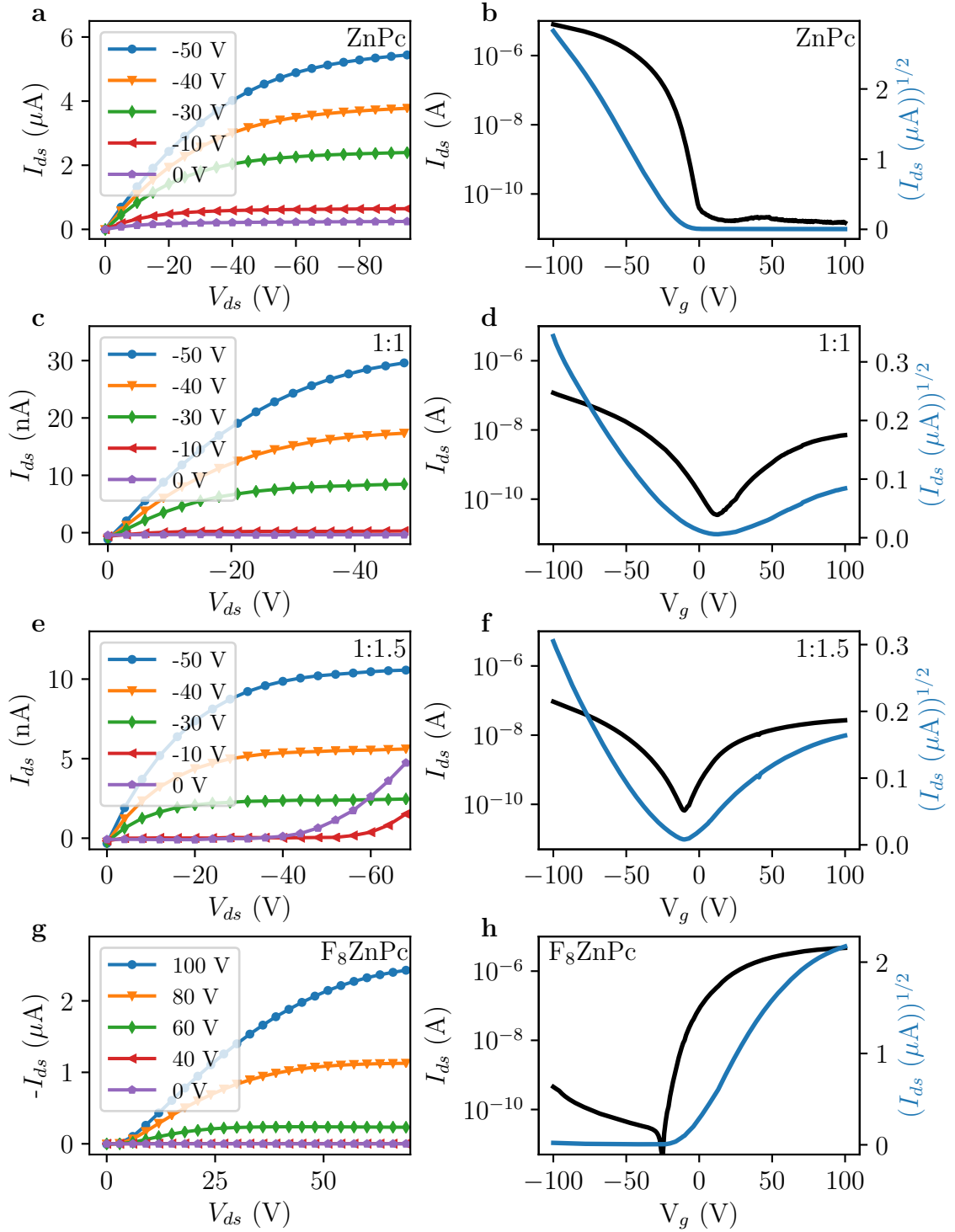
Figure 4.9: Output and transfer sweeps of ZnPc:F$_8$ZnPc blends. (a, c, e, g) Output (I_{ds} against V_{ds}) for a range of gate voltages V_g and **(b, d, f, h)** transfer characteristics (I_{ds} and $\sqrt{I_{ds}}$ against V_g, with $V_{ds} = -50\,\text{V}$) of **(a, b)** pristine ZnPc, **(c, d)** mixed-film ambipolar OFETs with weight ratio 1:1, and **(e, f)** 1:1.5 ZnPc:F$_8$ZnPc, and **(g, h)** pristine F$_8$ZnPc, all with channel length 10 μm.
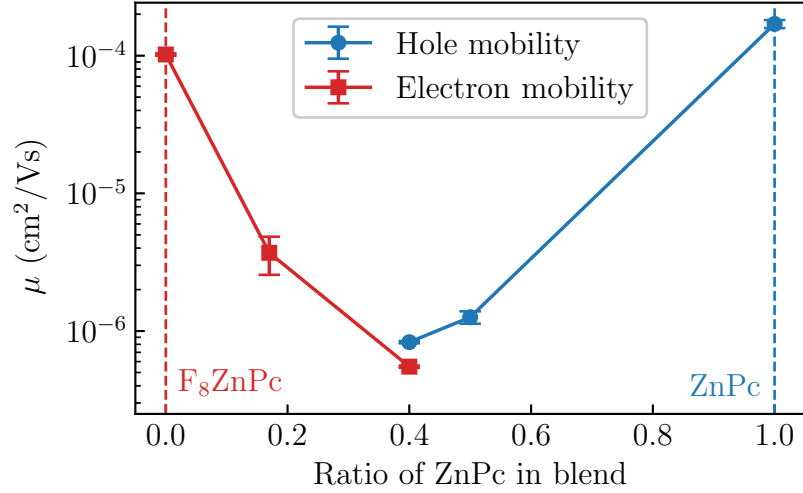
Figure 4.10: Field-effect mobility of ZnPc:F$_8$ZnPc blends. Field-effect mobility μ extracted in the OFET saturation regime with channel length of 10 µm. The content of ZnPc in the blend of ZnPc:F$_8$ZnPc is expressed as a weight ratio with 0 representing neat F$_8$ZnPc, marked as a dashed red line, and 1 representing ZnPc, marked as a dashed blue line. The electron mobility is shown as red squares and the hole mobility is shown as blue circles. Error bars given represent the standard deviation of mobilities measured over four devices from the same deposition run.

outlined in Section 2.3.2. It is defined as the ratio of the maximum channel conductivity measured experimentally over the maximum conductivity expected in an equivalent ideal OFET (which assumes linear transconductance and zero threshold voltage) that has the claimed carrier mobility: $r = \sigma_{exp}^{max}/\sigma_{ideal}^{max}$ [101]. In this analysis, an ideal OFET corresponds to $r = 100\%$, allowing for the most unambiguous mobility extraction.

Judging by the reliability factors, the OFETs are far from ideal. Most measurements show a reliability factor $r < 100\%$, which may be expected for OFETs with a non-zero threshold voltage and a nonlinear transconductance. The hole mobility in the saturation regime for the 1:1 and 1:1.5 blend show $r > 100\%$, which reflects a specific hump-like nonlinearity in the transfer curve and a possible overestimation of the mobility. In Figure 4.9d and Figure 4.9f, this hump nonlinearity is apparent as a constant curvature in the transconductance. In these cases, defining a region for extracting the mobility is ambiguous, and therefore reporting the measurement reliability factor has value conveying this uncertainty. In the orginal report outling

the use of the reliability factor, the behaviour of very few real OFETs obeys the oversimplified physics [173].

Following a similar argument to that outlined in Section 4.2, the decrease in mobility in the blends of ZnPc:F_8ZnPc of over two orders of magnitude can be partly attributed to increasing injection barriers for both holes and electrons as the IE and EA of the blended semiconductor shift away from the work function of the gold source-drain electrodes [150, 174]. As for the pristine films, these barriers could also be embedded in the semiconductor blend itself, as well as at the contacts. Furthermore, the distribution of transport states in the blended films is expected to be broader than that of the single component films, due to the offset between the highest occupied molecular orbitals of the ZnPc and F_8ZnPc [10]. This increases energetic disorder in the blend which, as was shown for C_{60} OFETs, can lead to a reduction of the charge carrier mobility [175].

4.3.1 Structural characterisation

Figure 4.11 shows the 2D reciprocal space maps of the ZnPc, blends of 1:1 and 1:1.5 ZnPc:F_8ZnPc weight ratio, and F_8ZnPc films.[2] As before, the peaks indicated by arrows in Figure 4.11a are ascribed to the (200) peak of the herring-bone like α-phase of ZnPc [118, 159]. All films display two preferred orientations indicated by the position of the (200) peak, either fully out-of-plane or fully in-plane. For each configuration,

[2]GIWAXS measurements were performed by Dr Josue F. Martinez Hardigree and Mr Andreas E. Lauritzen (University of Oxford, UK).

	μ_h^{sat} (cm^{2}V^{-1}s^{-1})	r$_h^{sat}$ (%)	μ_h^{lin} (cm^{2}V^{-1}s^{-1})	r$_h^{lin}$ (%)
ZnPc	$(1.7\pm0.1) \times 10^{-4}$	53	$(1.9\pm0.1) \times 10^{-4}$	53
1:1	$(1.3\pm0.1) \times 10^{-6}$	120	$(2.8\pm0.2) \times 10^{-6}$	67
1:1.5	$(8.3\pm0.2) \times 10^{-7}$	126	$(2.5\pm0.1) \times 10^{-6}$	47

Table 4.3: Hole mobilities in the ZnPc:F_8ZnPc films. Table summarising the hole mobilities μ_h as measured in the linear and saturation regime, alongside the measurement reliability factor r, indicating how well the reported mobilities compare to the ideal Shockley equations.

	μ_e^{sat} (cm^{2}V^{-1}s^{-1})	r$_e^{sat}$ (%)	μ_e^{lin} (cm^{2}V^{-1}s^{-1})	r$_e^{lin}$ (%)
1:1.5	$(5.5\pm0.1) \times 10^{-7}$	68	$(3.6\pm0.2) \times 10^{-7}$	82
1:5	$(3.7\pm1.1) \times 10^{-6}$	86	$(4.5\pm0.6) \times 10^{-6}$	69
F$_8$ZnPc	$(1.0\pm0.2) \times 10^{-4}$	68	$(7.6\pm0.3) \times 10^{-5}$	72

Table 4.4: Electron mobilities in the ZnPc:F$_8$ZnPc films. Table summarising the electron mobilities μ_e as measured in the linear and saturation regime, alongside the measurement reliability factor r, indicating how well the reported mobilities compare to the ideal Shockley equations.
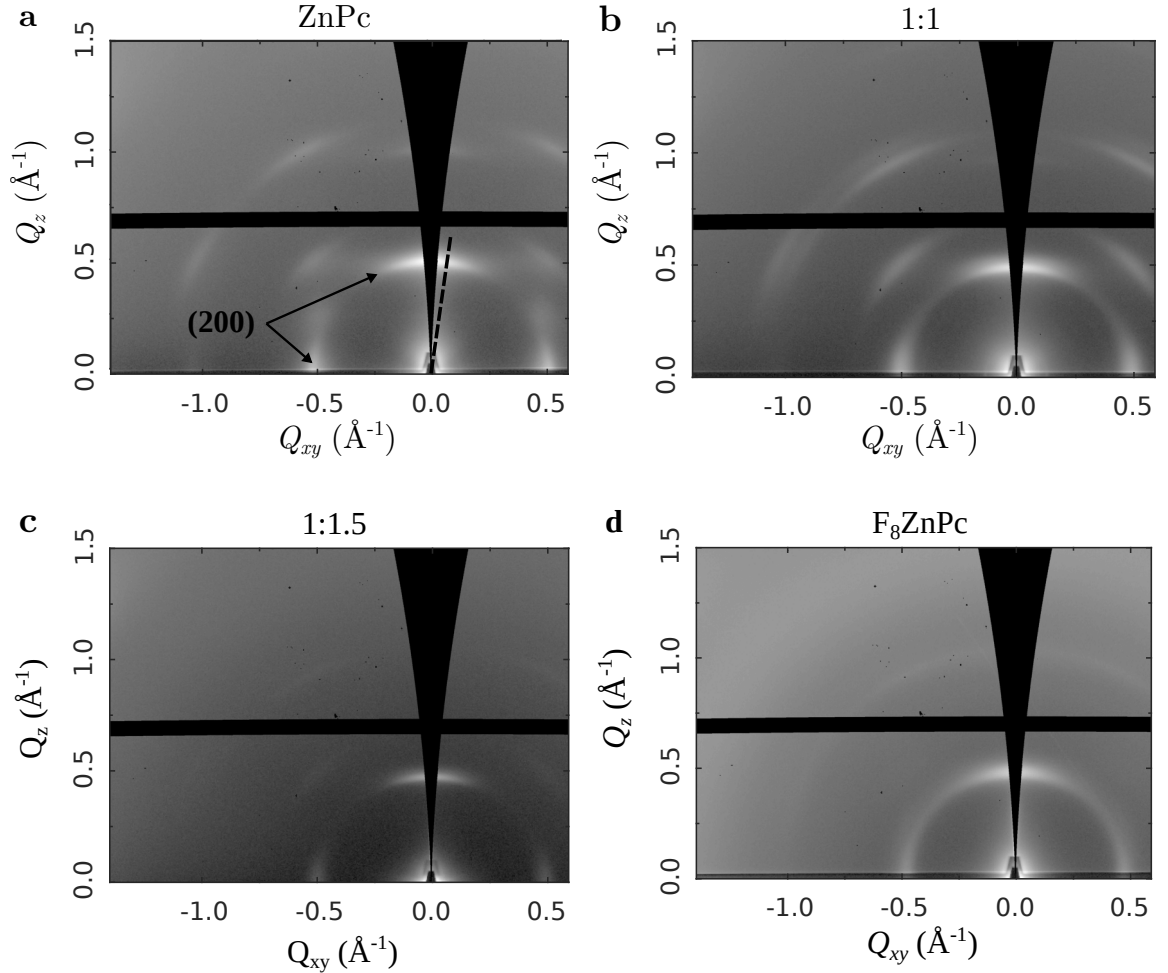
Figure 4.11: GIWAXS images of ZnPc:F$_8$ZnPc blends. of **(a)** ZnPc **(b)** 1:1 and **(c)** 1:1.5 ZnPc:F$_8$ZnPc weight ratio; and **(d)** F$_8$ZnPc evaporated on SiO$_2$. For ZnPc in **(a)**, the (200) peaks are indicated. Line cuts are made in the near out-of-plane direction through the (200) Bragg peak using a simple sector integration between 7° and 8° from the out-of-plane axial orientation.

the out-of-plane peak appears more strongly than the in-plane peaks, indicating that edge-on orientation is preferred over the face-on configuration [159]. Comparing the pristine films first, ZnPc (Figure 4.11a) exhibits greater crystalline ordering than the F_8ZnPc (Figure 4.11d) as indicated by the visible higher order reflections and strong (200) reflections. Furthermore, the F_8ZnPc appears more powder-like suggesting a greater variation of crystallite orientations as compared to the ZnPc. The 1:1.5 $ZnPc:F_8ZnPc$ blend (Figure 4.11c) shows the weakest reflection intensities with the in-plane peaks appearing only faintly, suggesting less crystalline ordering than in the pristine films.

The location of the peaks and the corresponding d-spacing are displayed in table 4.5. The periodicity of the $ZnPc:F_8ZnPc$ blends being closer to the periodicity of the pristine F_8ZnPc could indicate that the scattering signal from the blend arises primarily due to ordered F_8ZnPc within a host matrix of disordered ZnPc. Alternatively, the ZnPc and F_8ZnPc could co-crystallise, with the fluorinated molecules inducing a stacking structure similar to that of pristine F_8ZnPc. Reports of intermixing at a molecular level in systems of copper-phthalocyanine and its fluorinated derivative ($CuPc:F_{16}CuPc$) are consistent with this latter picture [118, 176].

4.3.2 Device hysteresis

Figure 4.12 shows the device hysteresis of the blended ambipolar OFETs, alongside pristine ZnPc and F_8ZnPc for reference. All the devices show a lower back sweep current (that is the sweep from the on state towards the off state). As in the previous section, this indicates that the hysteresis is linked to traps in the semiconductor rather than an effect of the dielectric. Approaches to reduce hysteresis include increasing the capacitance of the dielectric layer [177], and performing surface treatments to reduce traps states at the SiO_2 interface [178].

	Q (Å^{-1})	d_{200}-spacing (Å)
ZnPc	0.503	12.5
1:1	0.486	13.0
1:1.5	0.470	13.4
F_8ZnPc	0.476	13.2

Table 4.5: GIWAXS peak fits and *d*-spacing. Q-values derived from fitted line cuts through 2D GIWAXS images (Figure 4.6) in the near out-of-plane direction through the (200) Bragg peak using a simple sector integration between 7° and 8° from the out-of-plane axial orientation.
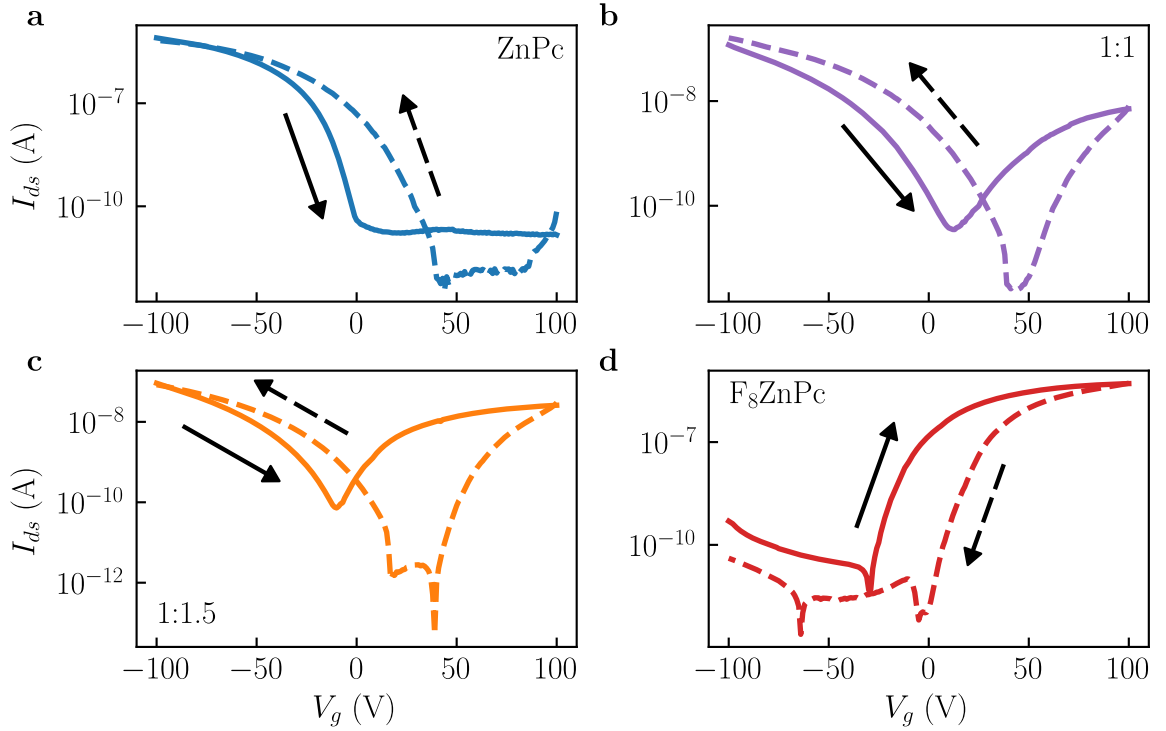
Figure 4.12: Device hysteresis in the transfer characteristics of ZnPc:F_8ZnPc blends. Transfer sweeps scanned from negative to positive (solid lines) and positive to negative (dashed lines) for pristine OFETs of **(a)** ZnPc, **(b)** 1:1 and **(c)** 1:1.5 ZnPc:F_8ZnPc, and **(d)** F_8ZnPc. All devices have a channel length of 10 μm and the scan rate is 5 V/s. The hysteresis loops are stable over multiple successive sweeps.

4.4 Application in voltage inverters

Having achieved ambipolar mobility through the mixing of ZnPc and F_8ZnPc, voltage inverters are realised by placing the OFETs in series, as shown in the inset to Figure 4.13 and Figure 4.14. Figure 4.13 shows a voltage inverter based on complementary logic incorporating a pair of p-type (ZnPc) and n-type (F_8ZnPc) transistors with a supply voltage $V_{dd} = 50\,\text{V}$. At voltages below a threshold of around 44 V, the p-type OFET is on whilst the n-type OFET is off giving an output voltage almost equal to the supply rail. Above 44 V, the p-type OFET switches off and the n-type OFET switches on, resulting in the low state for V_{out}. The threshold voltage (V_T) of an inverter is given by

$$V_T = \frac{(V_{dd} + V_{Tp} + (\mu_n/\mu_p)^{1/2}V_{Tn})}{(1 + (\mu_n/\mu_p)^{1/2})} \tag{4.2}$$

where V_{Tp} and V_{Tn} are the threshold voltages for the p-type and n-type OFETs, respectively [179]. Taking an average of the threshold voltages over four devices for each material, the calculated threshold voltage of the inverter shown here is (38 ± 11) V which is in agreement with the experimental data (summarised in Table 4.6). The inverter has a gain of 5 with a good noise margin.

As the ambipolar OFETs show both n- and p-type behaviour, so-called *complementary-like* voltage inverters based on two ambipolar OFETs in series, are realised. Figure 4.14 shows the transfer characteristics of a voltage inverter driven with V_{dd} = 50 V composed of two ZnPc:F_8ZnPc OFETs with a blend ratio of 1:1.5. A blend ratio of 1:1.5 is used because it shows the best balance between hole and electron mobility. The threshold voltage is calculated as (48 ± 2) V, which appears to be in agreement with the experimental data (Table 4.6). Below the threshold voltage, the output is around 40 V and above falls to 10 V. The dependence of V_{out} on V_{in} at low and high values of V_{in} is attributed to the lower on/off ratio in the blended transistors as compared to the pristine ZnPc and F_8ZnPc devices. Consequently there is always a leakage current flowing through the inverter as neither transistor are fully switched off [150]. Overall, the performance of the complementary-like inverter, in terms of
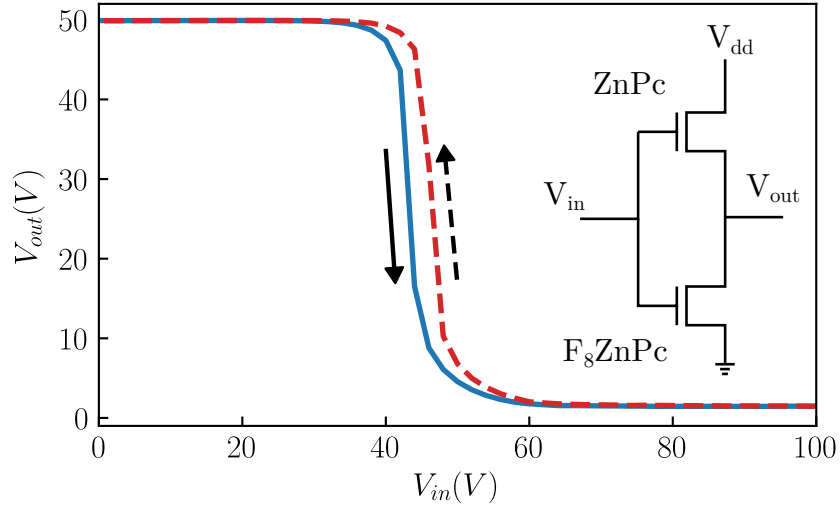
Figure 4.13: Complementary voltage inverter based on an n-type and a p-type OFET. Transfer characteristics of a complementary inverter with ZnPc as the p-type OFET and F_8ZnPc as the n-type OFET. The arrows represent the scan direction. The supply rail was held at $V_{dd} = 50\,\text{V}$. The inset diagram shows the circuit configuration.
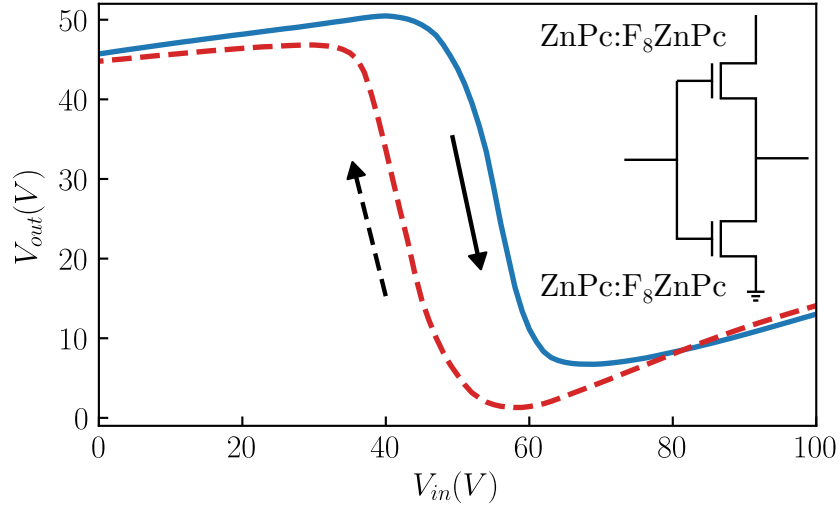

Figure 4.14: Complementary-like voltage inverter based on two ambipolar OFETs. Transfer characteristics of an inverter with two ZnPc:F_8ZnPc OFETs with weight ratio 1:1.5. The supply rail was held at $V_{dd} = 50\,\text{V}$. The arrows represent the scan direction. The inset diagram shows the circuit configuration.

	V_{Tp} (V)	V_{Tn} (V)	Calc. V_T (V)	Meas. V_T (V)
Compl. inverter	16±11	2±22	38±11	42±2
Ambipolar inverter	25±2	15±4	48±2	50±10

Table 4.6: Voltage inverter threshold voltages. Table summarising the calculated and measured threshold voltages for both the complementary and ambipolar (complementary-like) ZnPc:F$_8$ZnPc voltage inverters. V_{Tp} and V_{Tn} are the threshold voltages for the p-type and n-type OFETs, respectively, averaged over four devices scanned in both the forwards and backwards direction. For the ambipolar inverter, V_{Tp} and V_{Tn} are the hole and electron threshold voltages, respectively, for the 1:1.5 ZnPc:F$_8$ZnPc OFETs.

the measured threshold voltage, is very similar to that of the inverter based on the separate p- and n-type OFETs.

The ambipolar voltage inverter shows a considerable hysteresis as compared to the complementary inverter. This hysteresis is observed when measuring the individual OFETs of the blends at a scan rate of 5 V/s (Section 4.3.2). We therefore take averages over forward and backward scans for fitting the mobilities and threshold voltages. Finally, the OFET performance, and therefore voltage inverter performance, could be improved by a number of means. In OFETs of CuPc, the field-effect mobility was found to increase with substrate temperature during deposition, with a maximum for the mobility found around a substrate temperature around 120 °C [180, 181]. Alternatively, a post-deposition annealing step has also been shown to improve the mobility and the current on/off ratio in CuPc OFETs [182].

4.5 Conclusion

In summary, ambipolar OFETs with balanced hole and electron transport were fabricated based on the co-evaporation of ZnPc and its fluorinated derivative F$_8$ZnPc. OFETs of the pristine p-type ZnPc show a mobility of $(1.7 \pm 0.1) \times 10^{-4}\,\mathrm{cm^2V^{-1}s^{-1}}$ measured in the saturation regime. F$_8$ZnPc OFETs show an electron mobility of a similar magnitude around $(1.0 \pm 0.1) \times 10^{-4}\,\mathrm{cm^2V^{-1}s^{-1}}$. The current on/off ratio of the OFETs in both cases is 10^5. By co-evaporating these two p- and n-type

semiconductors, tunable p-type to ambipolar to n-type behaviour dependent on the weight ratio of ZnPc to F_8ZnPc was demonstrated. The optimum balance between the hole and electron mobility was achieved in the blend of 1:1.5 weight ratio. In this blend, the hole and electron mobility were $(8.3 \pm 0.2) \times 10^{-7}\,\mathrm{cm^2V^{-1}s^{-1}}$ and $(5.5 \pm 0.1) \times 10^{-7}\,\mathrm{cm^2V^{-1}s^{-1}}$, respectively. As these transistors show both p- and n-type behaviour, complementary-like voltage inverters were built which show comparable performance to the inverters based on separate p- and n-type OFETs. Obtaining balanced ambipolar transport in OFETs via energy level tuning, as demonstrated here, could be extended to other systems of organic semiconductors, which permit a shift in their energy levels when blended with their halogenated derivatives.

5. Energy level tuning in doped semiconductors

5.1 Introduction

The prevailing practice for selecting host and dopant combinations is based on securing a favourable offset between the host and dopant's energy levels, typically measured independently from one another. For p-doping, this would involve introducing a dopant with an electron affinity (EA) larger than the ionisation energy (IE) of the host semiconductor (Section 2.2). However, as reported for the well-studied case of zinc-phthalocyanine (ZnPc) and molecular p-dopant F_6-TCNNQ[81, 125, 130, 131], this understanding of the doping mechanism is incomplete. Judging from the energy levels of the isolated molecules [10, 75, 128], the doping process is expected to be more efficient than is experimentally observed [81].

In this chapter, the role of energy level offset between the host and dopant on the charge transfer efficiency in the doping process is investigated. The IE of the host semiconductor is varied via the energy level tuning effect using a blend of $ZnPc:F_8ZnPc$, as put into practice in the previous chapter. Thus the vacuum deposited samples comprise a ternary blend of co-evaporated $ZnPc:F_8ZnPc$ (the host blend) with dopant F_6-TCNNQ. The experimental methods and measurement details are described in Chapter 3. Dopant ionisation is first investigated using absorption measurements, which establish that the charge transfer doping efficiency has a dependence on composition of the blend. The trend is confirmed and quantified with electron paramagnetic resonance measurements, which probe the unpaired electronic spins generated upon charge transfer. To better understand these findings, a statistical model based on Fermi-Dirac statistics is developed. The results of parameter

testing the model suggest that the energy level tuning effects that have been observed for the host blend, $ZnPc:F_8ZnPc$, are also applicable to the dopant. Quantum chemical calculations show that the planar dopant has a quadrupole moment in the π-π stacking direction, comparable to that of the F_8ZnPc. With the approximation that the dopants energy levels shift in a similar way to the F_8ZnPc in the ternary blend, the statistical model successfully reproduces the experimental results.

This chapter is published as Warren, R. *et al.* Controlling energy levels and Fermi level en route to fully tailored energetics in organic semiconductors. *Nat Commun* **10,** 5538 (2019).

5.2   Experimental results

5.2.1   Photothermal deflection spectroscopy

Previous experiments have shown that ground-state integer-charge transfer occurs for $ZnPc:F_6$-TCNNQ [81, 128], leading to at least partial polaron pair formation on the host H $\rightarrow$ H$^+$ and dopant D $\rightarrow$ D$^-$. As the absorption coefficients of these sub-gap states are typically very low [183], photothermal deflection spectroscopy (PDS) measurements at room temperature are performed[1].

Figure 5.1a, Figure 5.1b and Figure 5.1c show the absorption coefficient measured by PDS against probe beam energy for films of ZnPc, a 1:1 blend of $ZnPc:F_8ZnPc$, and F_8ZnPc, respectively, undoped and doped with 0.05 molar ratio (MR) of F_6-TCNNQ. For the unmixed (Figure 5.1a and Figure 5.1c) and undoped reference films, only the characteristic Q-band absorption peaks in the red region, at around $1.77\,\mathrm{eV}$ ($700\,\mathrm{nm}$) and $2.03\,\mathrm{eV}$ ($610\,\mathrm{nm}$), of the spectrum are present. This Q-band is a doublet due to Davydov-splitting, an effect of excited state degeneracy by vibronic coupling [129].

Interestingly, the Q-band transition of the F_8ZnPc is blue-shifted by around 20 meV relative to the ZnPc. This shift has also been reported by Brendel et al. and can be attributed to changes in the transition dipole alignment and intermolecular coupling upon fluorination [129]. Furthermore, this blue-shift is pertinent for the

---

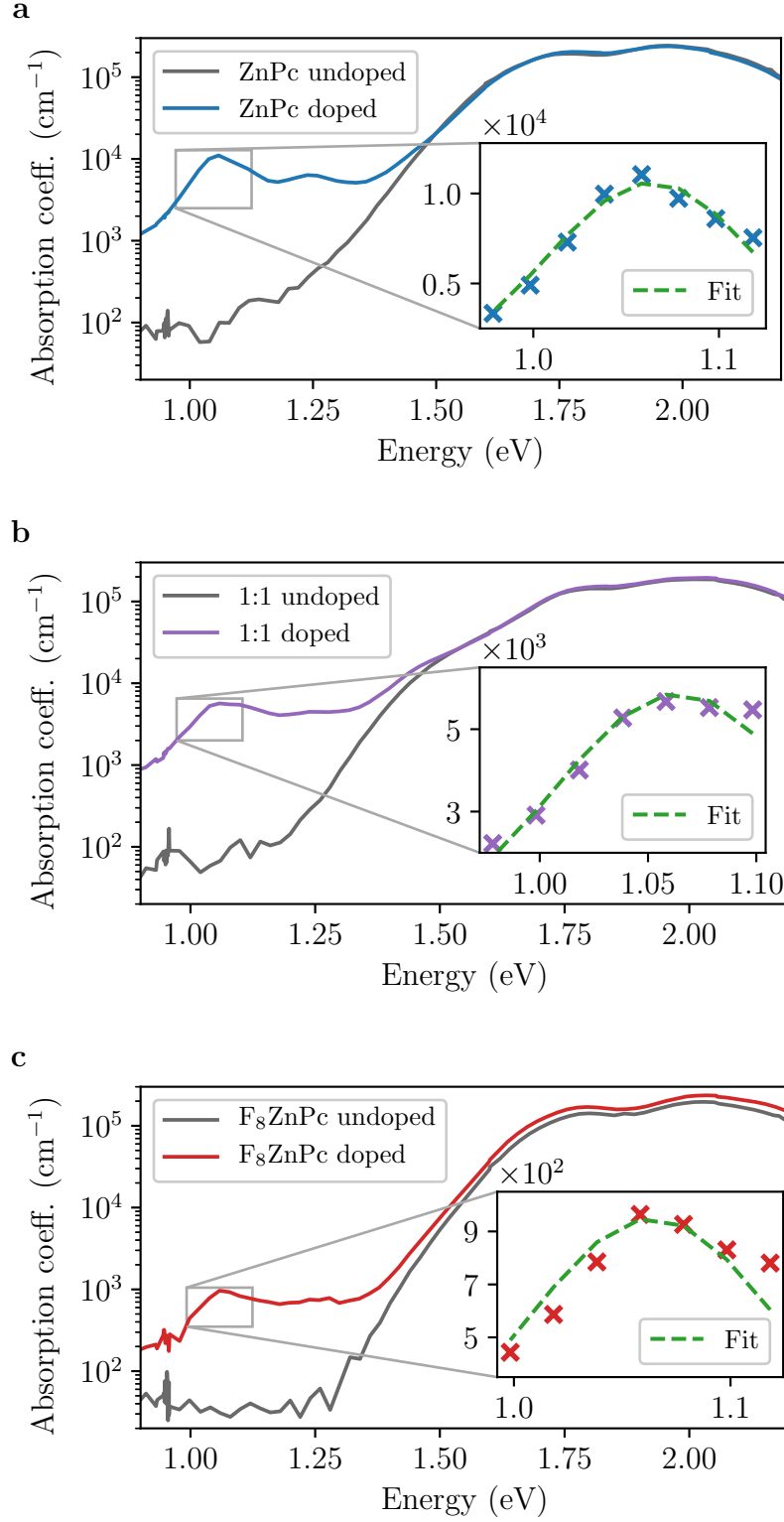[1]PDS measurements are made by Mr Oliver Thimm (Forschungszentrum Jülich, Germany).

Figure 5.1: PDS absorption spectra for the undoped and doped films.
Absorption spectra showing the appearance of the peaks related to the ionisation of the dopant for **(a)** ZnPc, **(b)** a 1:1 blend and **(c)** F_8ZnPc. The insets show the Gaussian fit of the peak at 1.06 eV.

mixed case, suggesting that the blend favours a structure with greater similarity to that of F_8ZnPc over that of the ZnPc. This observation is supported by d-spacing measurements from grazing-incidence wide-angle scattering (GIWAXS) images (see Section 5.2.2).

Along with the Q-band absorption feature, there is also a broad absorption feature present at around $1.50\,eV$ in the film of the 1:1 blend of $ZnPc:F_8ZnPc$ (Figure 5.1b). Similar absorption features have been indicative of ground-state charge-transfer complexes [184], and could represent the $ZnPc^+$ cation, which has been reported to have an absorption feature at $1.48\,eV$ ($840\,nm$) [185]. Upon p-doping in all films, an additional peaks appears around $1.06\,eV$ ($1170\,nm$) and $1.24\,eV$ ($1000\,nm$), which are attributed to the F_6-TCNNQ$^-$ anions, in agreement with reported reflection/transmission measurements on the same system [74, 81]. The inset to each figure demonstrates the Gaussian fits of the dopant peak at $1.06\,eV$ ($1170\,nm$) used later in this analysis.

Moving on to a range of host composition ratios, Figure 5.2a shows the absorption coefficient measured by PDS against probe beam energy for blends of $ZnPc:F_8ZnPc$ p-doped with 0.05 molar ratio (MR) of F_6-TCNNQ. For all cases, the optical absorption coefficient shows a region of low absorption below the $\pi \rightarrow \pi^*$ transitions of the phthalocyanine's Q-band, with the two dopant peaks at $1.06\,eV$ ($1170\,nm$) and $1.24\,eV$ ($1000\,nm$) marked on Figure 5.2a, in the sub-gap region. Although the intensities of the anion peaks are largest for transitions in $ZnPc:F_6$-TCNNQ, there is evidence of charge transfer for all samples, even for $F_8ZnPc:F_6$-TCNNQ. The integer charge transfer occurs from the IE of the host to the EA of the dopant. For the case of pure ZnPc as the host, this energy offset is thought to be favourable and the doping effect is expected. In contrast, the IE of F_8ZnPc exceeds the EA of the dopant. It is therefore surprising that a peak at $1.06\,eV$ of the ionised dopant is present at all with the host of pure F_8ZnPc.

To quantify the dopant absorption features, the peaks in the sub-band gap region are fitted with Gaussian functions with the same standard deviation (examples shown in the inset of Figure 5.1a, Figure 5.1b and Figure 5.1c). The peak height of the fits are normalised to the $\pi \rightarrow \pi^*$ transition at $1.77\,eV$, and are plotted in Figure 5.2b
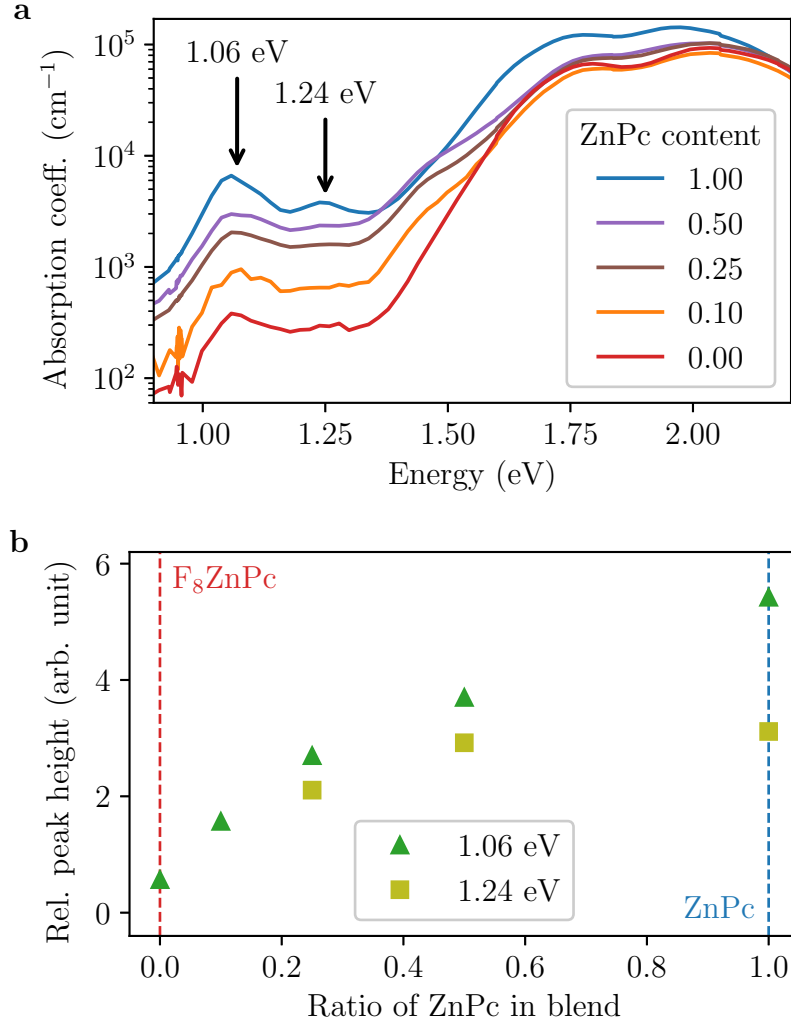
Figure 5.2: Absorption spectra of p-doped films. (a) Absorption spectra for different blend ratios of ZnPc:F_8ZnPc p-doped at 0.05 molar ratio (MR) with F_6-TCNNQ. The unmixed host of ZnPc with the dopant is marked as 1.00 and the unmixed case of F_8ZnPc as host is marked as 0.00. **(b)** Relative peak height of the absorption features at 1.06 eV (1170 nm) and 1.24 eV (1000 nm), against the weight ratio of ZnPc in the host-blend. These features are attributed to the ionised dopant. The peak heights are scaled relative to the intensity of the Q-band absorption peak at 1.77 eV (701 nm).

against the ratio of ZnPc in the host-blend. The absorption coefficient shows a clear monotonic increase as the content of ZnPc in the blend increases. As the doping concentration is fixed, the trend in the absorption coefficient is proportional to the fraction of ionised dopants N_A^-/N_A. This trend indicates that charge transfer from host to dopant is dependent on the blend composition. Specifically, a greater fraction of dopants ionise when the ZnPc content in the blend increases.

5.2.2 GIWAXS

Grazing-incidence wide-angle x-ray scattering (GIWAXS) measurements are performed to investigate the crystalline structure of the samples.[2] Figure 5.3 shows the 2D reciprocal space maps of the films of mixed ZnPc:F$_8$ZnPc with the ratio of ZnPc equal to 1.0, 0.5, 0.4 and 0, all doped at 0.05 molar ratio (MR). The films display two preferred grain orientations, either fully in-plane or out of plane, as seen by the (200) reflections. The out-of-plane peak is more intense, indicating a preference for edge-on orientation as opposed to face on [159]. All configurations show preferential orientations, which is a precondition for the coherent superposition of the quadrupolar fields of the host molecules [10].

Line cuts are made in the near out-of-plane direction through the (200) Bragg peak using a simple sector integration in DAWN between $7°$ and $8°$ from the out-of-plane axial orientation. The fits use a Lorentzian square function of the form:

$$y(x) = A/[1 + (x - pos/a)^2]^2 \tag{5.1}$$

where $FWHM = 2a(\sqrt{2} - 1)$ and $area = \pi a \frac{A}{2}$ and pos is the derived value of Q. The d-spacing values for the doped films are reported in Table 5.1. As compared to the undoped films in the previous chapter, the introduction of the dopant in the cases of ZnPc and the 0.5 ZnPc:F$_8$ZnPc blend results in a peak shift to a lower value in reciprocal space, corresponding to larger d-spacing values. For F$_8$ZnPc, the introduction of the dopant does not appear to affect the d-spacing. A possible

---

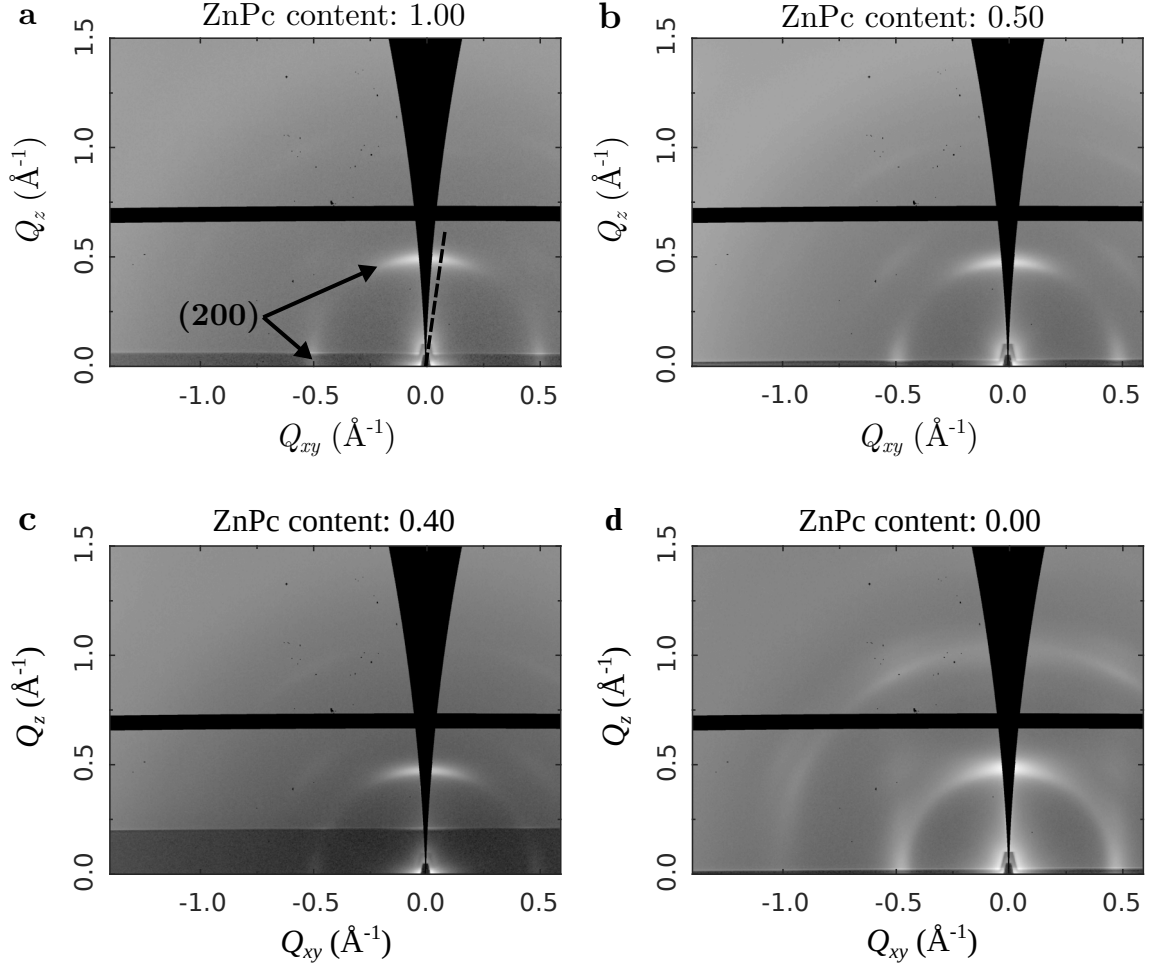[2]GIWAXS experiments and analyses are carried out by Mr Andreas E. Lauritzen (University of Oxford, UK).

Figure 5.3: GIWAXS images of p-doped films. GIWAXS 2D reciprocal space maps of films with **(a)** ZnPc content = 1.00, **(b)** ZnPc content = 0.50, **(c)** ZnPc content = 0.40 and **(d)** ZnPc content = 0.00, with doping concentration 0.05 MR, on SiO$_2$. All films display two preferred orientations either fully in-plane or fully out-of-plane, as seen by the (200) peak, with the out-of-plane orientation being the strongest, indicating a preference for edge-on orientation as compared to face on.

ZnPc content	Q [Å^{-1}]	d_{200}-spacing [Å]
1.0	0.488	12.9
0.5	0.472	13.3
0.4	0.470	13.4
0.0	0.479	13.1

Table 5.1: **GIWAXS peak fits and** d**-spacing.** Q-values derived from fitted line cuts through 2D GIWAXS images (Section 5.2.2) in the near out-of-plane direction through the (200) Bragg peak using a simple sector integration between 7° and 8° from the out-of-plane axial orientation.

explanation is that the inclusion of the dopant may cause greater disruption in more closely-packed lattices.

5.2.3 Electron paramagnetic resonance spectroscopy

The unpaired spins can be studied using electron paramagnetic resonance (EPR) spectroscopy.[3] The ground-state integer-charge transfer between the host and dopant, as observed in the PDS, generates unpaired electron spins. Figure 5.4 shows the continuous wave EPR spectrum, in the dark and at room temperature of ZnPc undoped and doped with 0.05 MR of F_6-TCNNQ. With the addition of the dopant, an EPR signal arises from the Zeeman interaction between the magnetic moments of the unpaired spins with the externally applied magnetic field.

Figure 5.5 shows the continuous wave EPR spectrum, in the dark and at room temperature, on a range of ZnPc:F_8ZnPc blend ratios, all doped with 0.05 MR of F_6-TCNNQ. The total EPR intensity decreases as the content of ZnPc decreases, indicating that there are fewer unpaired spins. The normalised EPR spectra for each blend ratio is presented in Figure 5.6. Taking the ternary blend sample of weight ratio 0.10:0.90 of ZnPc:F_8ZnPc as representative (Figure 5.6d), the EPR spectrum shows a signal with narrow line width and a field position typical of organic radicals [186]. From the spectral simulations, shown as dashed lines, two species are found to contribute to the signal with g-values of $g_A = 2.0023 \pm 0.0005$ and $g_B = 2.0033 \pm 0.0005$.

---

[3]EPR experiments and analyses were conducted by Dr Alberto Privitera (University of Oxford, UK).
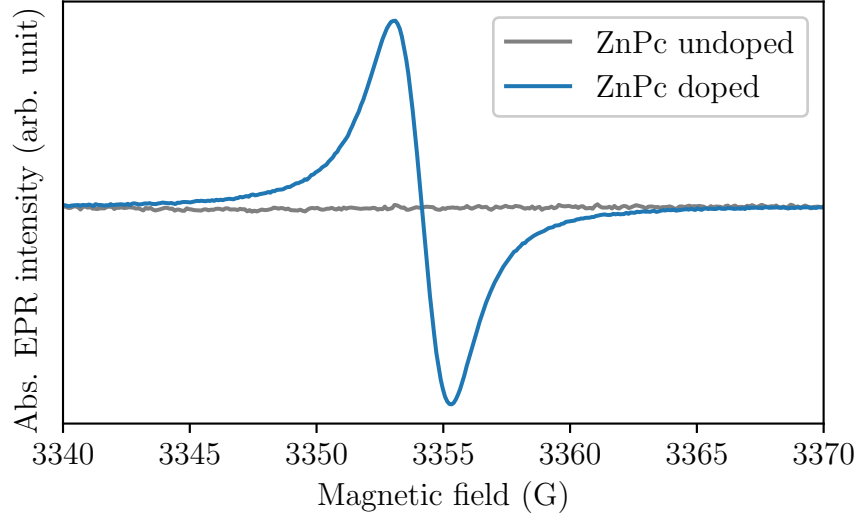
Figure 5.4: EPR spectra of ZnPc undoped and doped. Continuous wave EPR spectra of ZnPc undoped and doped at $0.05\,\text{MR}$ of F_6-TCNNQ. With the addition of the dopant, the spectral signature of the unpaired spins is observed.
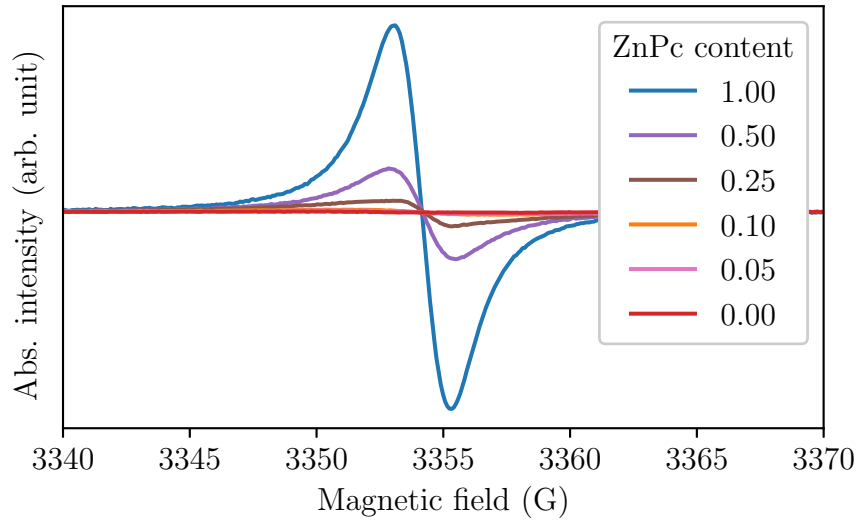

Figure 5.5: Absolute EPR intensity of p-doped samples with varying blend ratio. Continuous wave EPR spectra of a range of mixing ratios between ZnPc:F_8ZnPc, doped at $0.05\,\text{MR}$ of F_6-TCNNQ.

These g-values are similar to those previously reported for positive polarons localised on ZnPc (g_A) and the radical anion of F$_4$-TCNQ, which is assumed comparable to the g-value of F$_6$-TCNNQ (g_B) [187–189]. This suggests that, in agreement with the PDS, there is a ground-state electron transfer from the host-blend to the dopant.

Similar EPR analysis is performed for the range of ZnPc:F$_8$ZnPc composition ratios, with the simulations for each blend reported in Figure 5.6 with the g-values and line widths summarised in Table 5.2. The fits reveal the presence of the same two species as detected in Figure 5.6d, for all blends except that of the pure F$_8$ZnPc as the host. For the case of F$_8$ZnPc, shown in Figure 5.6f, the EPR signal is less intense, which indicates that the sample contains fewer unpaired spins. Although this signal is negligible compared to the ZnPc signal, it confirms that there is charge transfer between the F$_8$ZnPc and the dopant, as observed in the PDS, despite the nominally unfavourable energetic offset. Overall, the ground-state charge transfer from host-blend to dopant is dominated by the interaction between the ZnPc and dopant.

The EPR intensity is proportional to the overall amount of unpaired spins - a sum of contributions from both ground-state integer-charge transfer complexes (ICTCs) and mobile charges on the ZnPc and F$_8$ZnPc in the sample. The absolute number of spins in the samples can be calculated by double integration of the EPR signal (absolute EPR intensity) compared to a reference sample with a known number of

ZnPc Content	g_A	$linewidth_A$	g_B	$linedwidth_B$
1.00	2.0023 ± 0.0005	0.2	2.0033 ± 0.0005	[0.3, 1]
0.50	2.0023 ± 0.0005	0.25	2.0033 ± 0.0005	[0.3, 1]
0.25	2.0023 ± 0.0005	0.35	2.0033 ± 0.0005	[0.3, 1]
0.10	2.0023 ± 0.0005	0.5	2.0034 ± 0.0005	[0.3, 1]
0.05	2.0022 ± 0.0005	0.6	2.0034 ± 0.0005	[0.3, 1]
0.00	2.0032 ± 0.001	0.7	2.0035 ± 0.001	[0.3, 1]

Table 5.2: EPR g-values and line widths. Table showing the g-values and peak-to-peak line widths of the Lorentzian fits. Species A is attributed to the ZnPc positive polaron and species B is the F6-TCNNQ anion, except for the case of F$_8$ZnPc where g_A corresponds to the F$_8$ZnPc positive polaron with a larger g-value (species C).
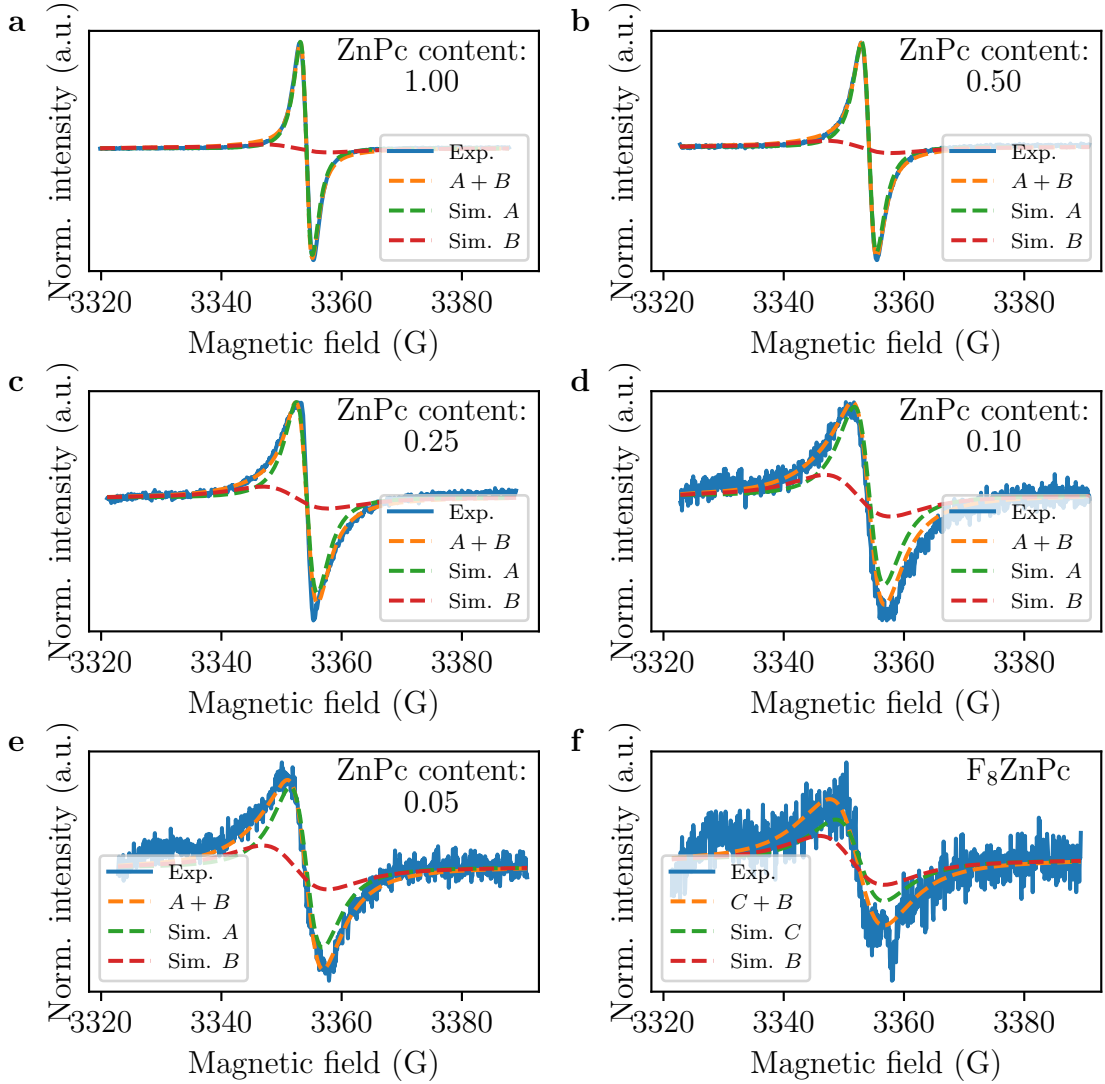
Figure 5.6: EPR spectra and simulations of p-doped blends. Continuous wave EPR spectra of all ratios of ZnPc:F_8ZnPc doped with 0.05 MR of F6-TCNNQ recorded at room temperature. The dashed orange lines represent the spectral simulations of the EPR spectrum obtained as the sum of two contributions from the ZnPc positive polaron (species A, green dashed line) and the F6-TCNNQ anion (species B, red dashed line). For the case of F_8ZnPc, the positive polaron is labelled as species C as it has larger g-value.
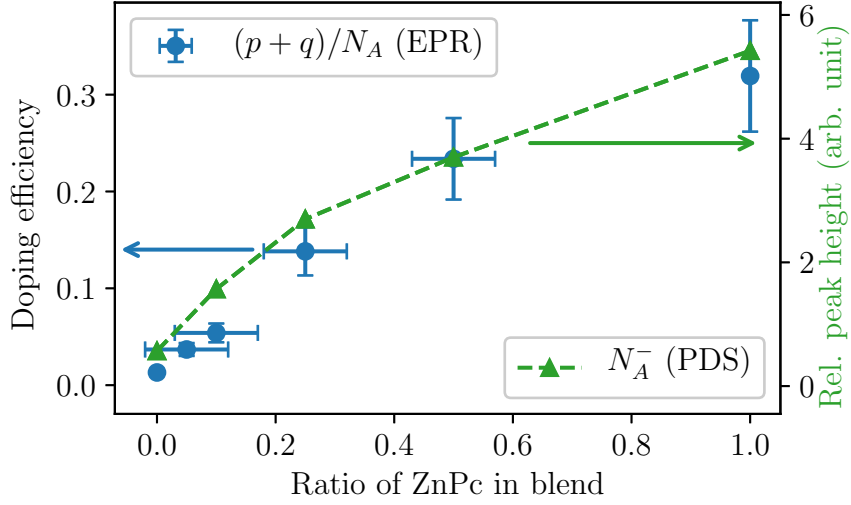
Figure 5.7: Doping efficiency as determined through EPR and PDS. Doping efficiency $(p + q)/N_A$ (blue circles, left axis), as calculated from the EPR signal, plotted against ratio of ZnPc in the blend. The relative peak intensity N_A^- from the PDS measurements are also plotted (right axis, green triangles). The error bars are propagated from the uncertainty in the spectral simulations, EPR calibration, quality factor of the EPR cavity, and material deposition rates.

spins. In the mixed host cases, the EPR line has an even contribution of holes on the ZnPc (p) and F_6-TCNNQ anions (N_A^-) [190], neglecting the small contribution of polarons on F_8ZnPc (q). Therefore, the polaron concentration is the total amount of measured spins divided by twice the sample volume. Finally, the doping efficiency is determined as the measured polaron concentration over the total number of dopants in the film $(p + q/N_A)$, with the number of dopants measured during deposition using a quartz crystal microbalance.

In Figure 5.7, the doping efficiency, as determined from the EPR signal, is plotted against ratio of ZnPc in the host-blend. There is a clear monotonic increase in the doping efficiency as the content of ZnPc increases, with the highest doping efficiency of $(31.9 \pm 5.7)\,\%$, reached for the host of pure ZnPc. A doping efficiency less than unity suggests that the system is in the dopant reserve regime (dopant ionisation has saturated), in agreement with UPS measurements on evaporated films of the same molecules [130]. The contribution from the F_8ZnPc polarons (EPR species C) gives the lowest doping efficiency of $(1.3 \pm 0.2)\,\%$. The overall trend of the doping

efficiency matches that observed in the PDS for the dopant anion peak, as expected due to charge conservation.

5.3   Statistical model

To establish how the trend in doping efficiency is related to the energy levels of the ternary blend system, a statistical description based on classical semiconductor theory is developed. This approach has been used to attribute shifts in the Fermi level of doped organic semiconductors to three regimes - trap filling (at doping concentrations below MR $< 10^{-4}$), dopant saturation and dopant reserve (MR $> 10^{-3}$) [130, 191]. More recently the efficient dissociation of ICTCs was explained by adjusting the energetic disorder in the model. [81] For 0.05 MR, the system is expected to operate in the dopant reserve regime, where trap states intrinsic to organic semiconductors have a negligible impact on doping efficiency [130].

Model details

Our statistical model contains an additional energy level for the third component in the ternary blend. The levels are approximated as Gaussian, all with the same standard deviation of σ. Gaussian approximations for the density of states (DOS) in organic semiconductors are widely-used in literature [39, 64, 90] and can be justified considering the central limit theorem (see Section 2.1.4). Alternative approximations include an exponential distribution, however previous work has shown that similar results are obtained to that of the Gaussian approximation at the doping ratio's considered here [191]. The host-blend comprises two separate DOS: one at higher energy representing the ZnPc and one at lower energy for the F_8ZnPc. The occupation of each of the levels is determined by Fermi-Dirac integrals, with the Fermi level set by numerically solving the neutrality condition

$$p + q = N_A^-, \tag{5.2}$$

where p and q are the number of holes (both mobile and bound) residing on ZnPc and F_8ZnPc, respectively, and N_A^- is the number of ionised dopants. The Fermi-Dirac

integrals for the density of charge carriers p and q are given by

$$p, q = \int_{-\infty}^{\infty} g_{p,q}(E)[1 - f(E)] \ dE \qquad (5.3)$$

where $f(E)$ is the Fermi-Dirac distribution and $g_{p,q}(E)$ are the density of states (DOS) for each host material. The DOS are approximated as Gaussian, centred around $E_{p,q}$ with standard deviation σ and normalised to the number of host molecules N_0

$$g_{p,q}(E) = \frac{N_0}{\sqrt{2\pi}\sigma} \exp\left[-\frac{(E - E_{p,q})^2}{2\sigma^2}\right]. \qquad (5.4)$$

The number of ionised dopants N_A^- is determined by an activation from the Fermi level to the dopant acceptor DOS of the form

$$N_A^- = \int_{-\infty}^{\infty} g_A(E, N_A) f(E) \ dE \qquad (5.5)$$

with the dopant DOS $g_A(E)$ also approximated as a Gaussian, centred around E_A with standard deviation σ,

$$g_A(E, N_A) = \frac{N_A}{\sqrt{2\pi}\sigma} \exp\left[-\frac{(E - E_A)^2}{2\sigma^2}\right]. \qquad (5.6)$$

To model the ternary blend, the effects of the quadrupole interactions between the host semiconductors, ZnPc and F_8ZnPc, are considered. The consequence of this interaction is that: 1) the difference in IE between the two components becomes considerably smaller, as compared to their IE in pristine films; and 2) both IEs shift linearly dependent on blend ratio. The energy levels of the two hosts in the mixed films are taken from the UPS measurements published by Schwarze et al. [10], with the gradient of the shift determined by linear fits, as shown in Figure 5.9. Whether the acceptor level of the dopant is affected by the same mechanism is an open question. Therefore both possibilities for the DOS of the system are investigated - one with a fixed dopant level (Figure 5.8a), and one with the dopant energy level shifting (Figure 5.8b). In Equation (5.6) for the fixed dopant level case, the dopant DOS remains static as compared to the shifting host levels, and is centred around energy E_A defined relative to the unmixed centre of the ZnPc DOS. For the shifting dopant
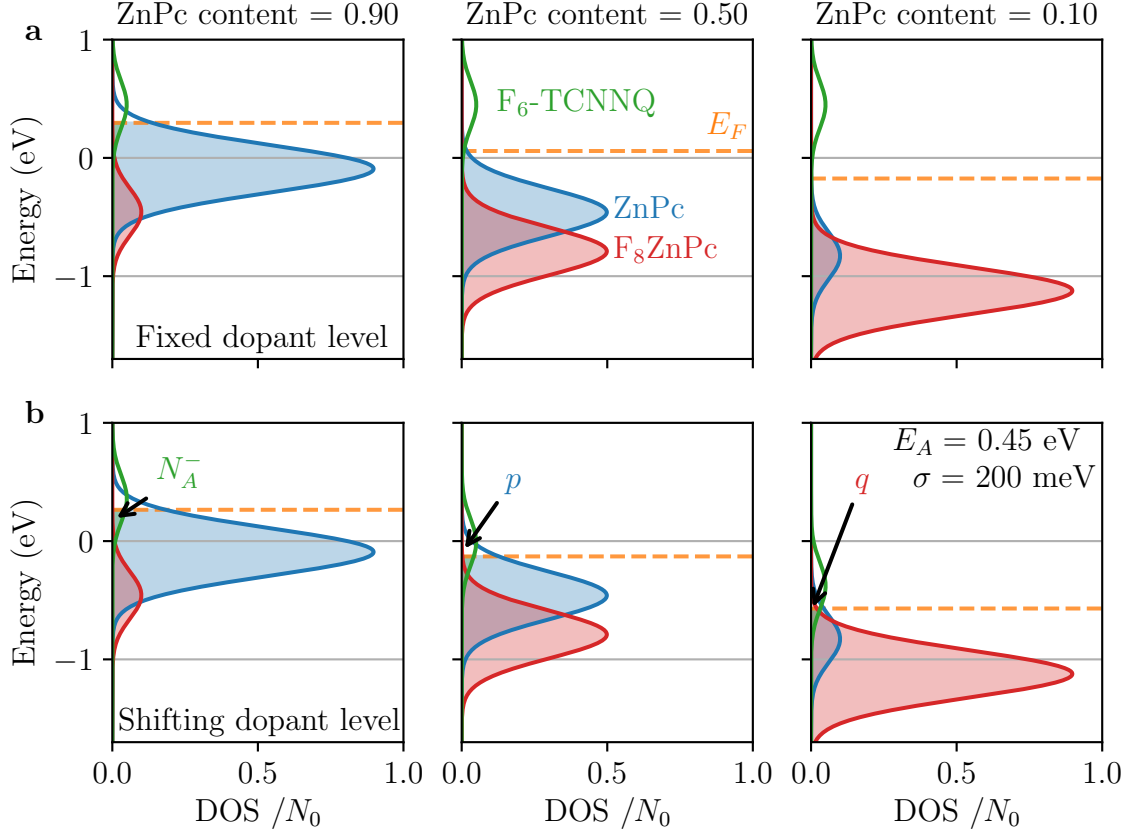
Figure 5.8: Density of states for the statistical model. The density of states (DOS) for the two cases of distributions: **(a)** with the dopant level at fixed energy and **(b)** with a dopant level shifting in energy, for molar ratios 9:1, 1:1, 1:9 of ZnPc:F_8ZnPc (left to right). The Fermi level E_F is calculated via Equation (5.2) and is plotted as a dashed orange line. Below the Fermi level, the dopants are ionised (filled green colour) and the host states are full (filled blue and red). The model parameters are reported inset in the right panel of **(b)**, and are varied in the analysis later.
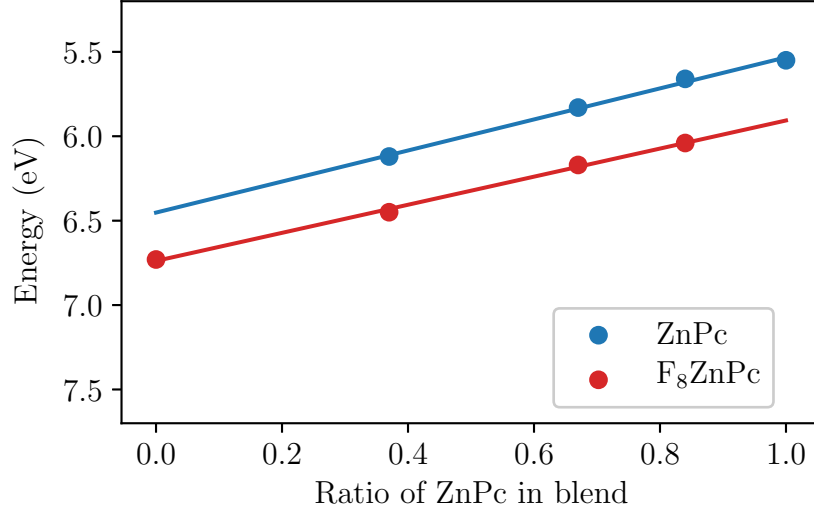
Figure 5.9: Energy level shifts of ZnPc and F$_8$ZnPc Linear fit of the peak maximum from ultraviolet photoelectron spectroscopy data on blends (weight %) of ZnPc:F$_8$ZnPc. The UPS data is from reference [10].

case, E_A is redefined relative to the shifting ZnPc DOS, such that it keeps a constant distance E_A from the centre of the ZnPc DOS.

In Figure 5.8a and Figure 5.8b, the area under each of the host components is proportional to the molar ratio in the host-blend. The area of the dopant DOS is constant, as the doping concentration is fixed. The Fermi level, calculated via Equation (5.2), is marked by a dashed orange line. All states below the Fermi level are occupied (shaded) whilst the states above are unoccupied (unshaded). Figure 5.8a shows the first case with the position of dopant energy level fixed. The Fermi level shifts to lower energy as the content of ZnPc in the host-blend decreases (left to right). Consequently, the proportion of ionised dopants N_A^- decreases with ZnPc content. Figure 5.8b shows the second DOS model, where the impact of electrostatic interactions arising from the quadrupole moments on the dopant's energy levels are considered. The major consequence is that E_A shifts downwards in energy, with respect to the vacuum level, dependent on the blend ratio of ZnPc and F$_8$ZnPc.

	Q_1	Q_2	Q_π
ZnPc	12.35	12.35	-24.69
F_8ZnPc	-14.76	-14.76	29.52
F_6-TCNNQ	-38.91	2.08	36.83

Table 5.3: Eigenvalues of quadrupole tensor. Values in atomic units, ea_0^2. Q_1 and Q_2 refer to the moments in the in-plane molecular directions and Q_π corresponds to the direction out-of-plane, as shown schematically in Figure 5.10. The B3LYP functional and 6-311g+(d,p) basis set were used in all calculations.
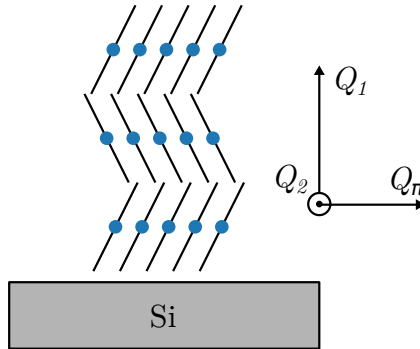
Figure 5.10: Quadrupole orientation. Schematic diagram showing Q_1, Q_2 and Q_π for edge-on molecules.

Justification of quadrupole effects

GIWAXS images of the doped films (Section 5.2.2) indicate a preference for edge-on orientation. Previous investigations have shown that molecular orientation can play a significant role in the electrostatic interactions [5, 36], and determines which component of the quadrupole tensor is dominant [33, 192]. For planar molecules, such as ZnPc, with edge-on orientation, the largest component of the quadrupole interaction is along the π-π stacking direction (Q_π), corresponding to the shortest intermolecular distance [12]. The directions of the quadrupole components for edge-on molecules are illustrated in Figure 5.10. As the addition of the p-dopant at low concentrations does not significantly impact the host packing [193, 194], it is expected that Q_π remains the dominant component in the doped films. Density functional theory (DFT) calculations, reported in Table 5.3, show that the dopant carries a net positive Q_π, comparable to that of the F_8ZnPc. Therefore, a coherent superposition of the dopant's quadrupolar molecular field with the ZnPc will result in a similar effect to

that observed for the F_8ZnPc - a linear shift in the dopant's energy dependent on the content of ZnPc in the host-blend. As the doping concentration is low, little impact of the dopant's quadrupole moment is expected on either of the host molecules. To a first approximation, the gradient of the dopant's shift in energy is set equal to that of the host distributions.

Model results

The two statistical descriptions are compared to the experimentally determined doping efficiency, plotted in Figure 5.11(a-d). The results of parameter testing E_A and σ are shown as solid lines in Figure 5.11(a-d) for both cases of a fixed and shifting dopant level. For parameter testing E_A, σ is kept constant at $160\,meV$ as the disorder in the $ZnPc:F_6TCNNQ$ system has been previously estimated via UPS [81]. For the fixed dopant case in Figure 5.11a and Figure 5.11b, the doping efficiency only begins to increase from zero when more then approximately 50% of the host-blend is ZnPc. Above 50%, the doping efficiency rises quickly with a strong dependence on E_A. Overall, the trends seen in the experimental data are difficult to reproduce with physical parameters for E_A and σ.

In contrast, the doping efficiency for the case with a shifting dopant level in Figure 5.11c and Figure 5.11d, shows a trend in close agreement with the experimental data. Upon introduction of ZnPc into the host-blend, the doping efficiency steeply rises. At high ZnPc content ratios, the efficiency tends toward a saturation value. With larger E_A, the doping efficiency is significantly reduced. In both models, the doping efficiency improves with increasing σ (Figure 5.11b and Figure 5.11d). As noted in recent studies, this highlights the importance of considering not just the energetic offset between host and dopant, but also the energetic disorder of the system as this can severely impact the doping efficiency [81, 131, 195].

The effect of charge transfer binding energy E_{CT}^b

The statistical model can be extended to separate the number of charge carriers into those that are mobile and those that are bound in ICTCs. In this additional
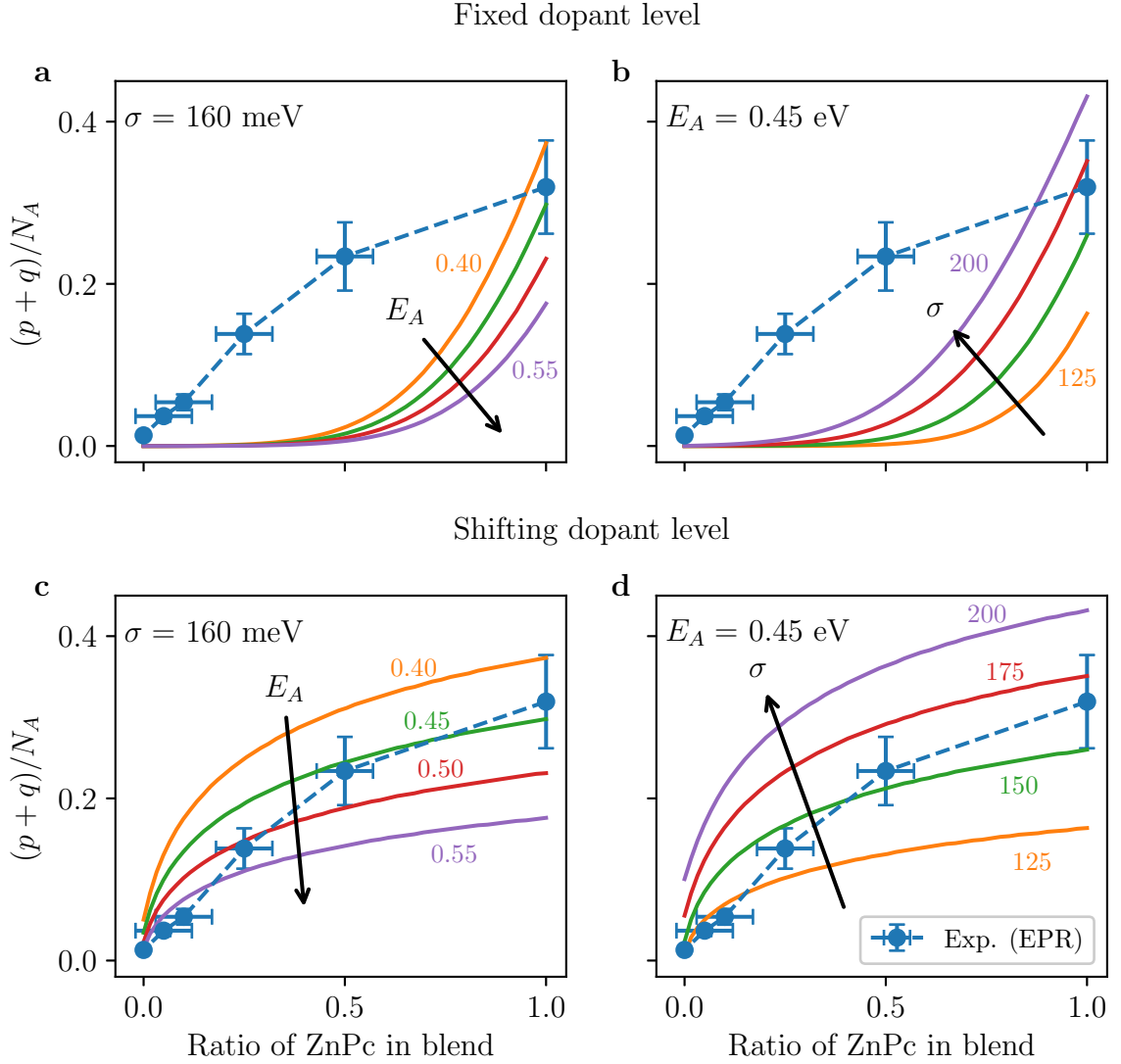
Figure 5.11: Statistical model comparison to EPR. Comparisons of the experimentally measured doping efficiency and the statistical models against weight ratio of ZnPc in the host blend, with the centre of the dopant's DOS E_A and standard deviation σ varied independently For the case where the dopant level is fixed: **(a)** shows variations in E_A with $\sigma = 160$ meV, and **(b)** shows variations in σ, with $E_A = 0.45$ eV. For the case where the dopant energy level shifts: **(c)** shows the variation in E_A, with $\sigma = 160$ meV, and **(d)** variations in σ, with $E_A = 0.45$ eV. The doping efficiency as determined via EPR is shown on all figures as blue circles with a dashed line.
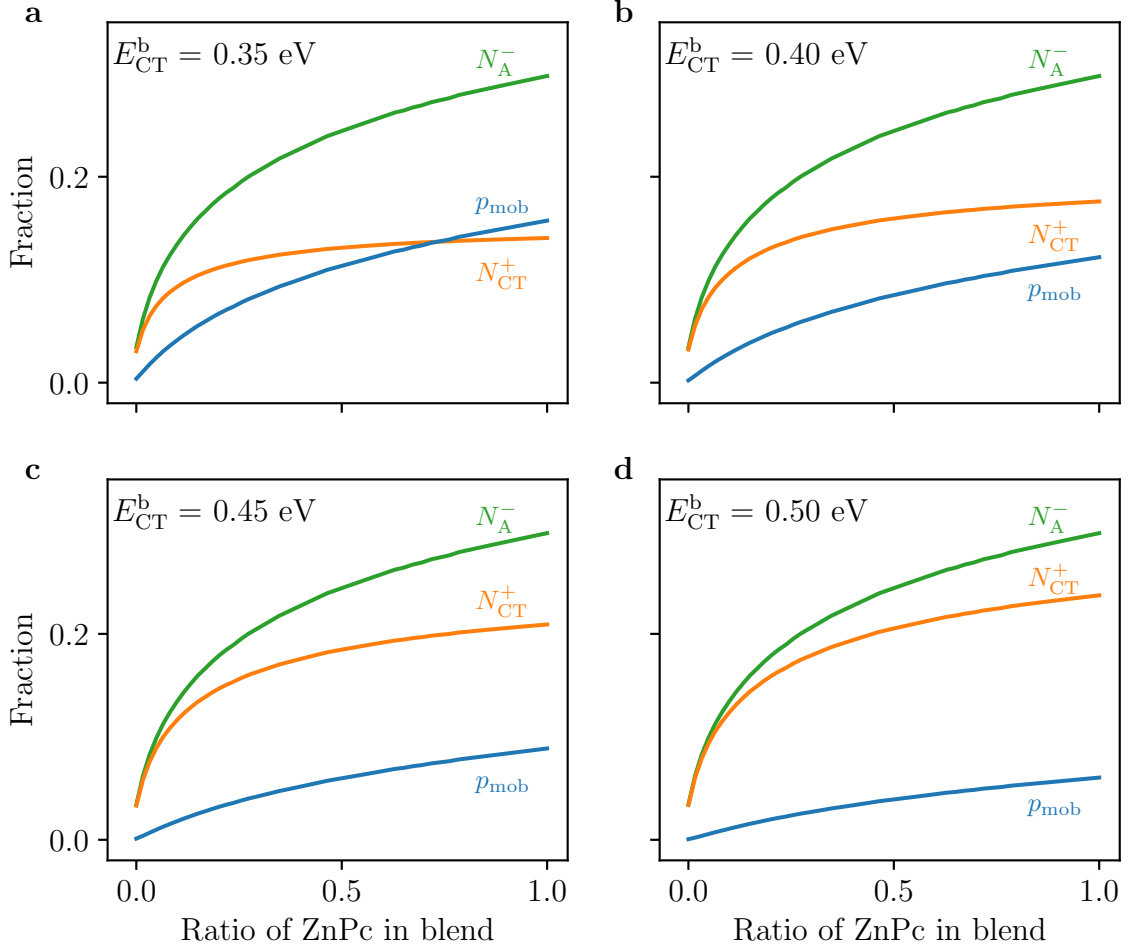
Figure 5.12: Impact of ICTC binding energy E_{CT}^b on charge separation.
The effect of varying ICTC binding energy E_{CT}^b on the contribution of mobile charges p_{mob}, and charges bound in ICTCs N_{CT}^+, in the shifting dopant model with **(a)** $E_{CT}^b = 0.35\,\text{eV}$, **(b)** $E_{CT}^b = 0.40\,\text{eV}$, **(c)** $E_{CT}^b = 0.45\,\text{eV}$, and **(d)** $E_{CT}^b = 0.50\,\text{eV}$. E_{CT}^b also shifts, remaining a fixed distance above the ZnPc DOS. The sum of these contributions is equal to the fraction of ionised dopants $p_{mob} + N_{CT}^+ = N_A^-$, assuming a negligible contribution from q. The parameters for the simulations are $E_A = 0.45\,\text{eV}$ and $\sigma = 160\,\text{meV}$. The standard deviation of the ICTC states is assumed to be equal to the semiconductor blend $\sigma_{ct} = \sigma$.

analysis, the total number of holes, p and q, on each semiconductor is the sum of mobile carriers, p_{mob} and q_{mob}, and the number bound in ground-state integer-charge transfer complex (ICTCs) between the host and dopant, p_{CT} and q_{CT}:

$$p = p_{mob} + p_{CT}, \qquad (5.7)$$

$$q = q_{mob} + q_{CT}. \qquad (5.8)$$

The neutrality equation, Equation (5.2), can then be rewritten as

$$p_{mob} + q_{mob} + N_{CT}^+ = N_A^-, \qquad (5.9)$$

where $N_{CT}^+ = p_{CT} + q_{CT}$ is the total number of bound carriers in ICTCs. Ignoring the small fraction of charges residing on F_8ZnPc, the total fraction of charges bound in ICTCs is given by the Fermi-Dirac integral

$$N_{CT}^+ = \int_{-\infty}^{\infty} g_{CT}(E, N_A^-)[1 - f(E)] \, dE, \qquad (5.10)$$

with the DOS $g_{CT}(E, N_A^-)$ approximated as a single Gaussian, centred around E_{CT}^b (defined with respect to the ZnPc DOS) with standard deviation σ.

Introducing ICTCs with binding energy E_{CT}^b has no impact on dopant ionisation N_A^-, as can be seen in Figure 5.12. Instead with larger E_{CT}^b, the primary effect is that a greater proportion of charge carriers remain bound in ICTCs. With PDS and EPR, the mobile and bound carriers cannot be distinguished. Therfore, testing this extension to the model is beyond the scope of our investigation. Possible future experiments to probe the mobile carriers in the film, include temperature dependent Mott-Schottky analysis or Hall effect measurements.

Justification of the dopant's DOS position E_A

Experimental measurements on unmixed thin films, place the EA of F_6-TCNNQ (5.5 eV) below that of the IE of ZnPc (5.1 eV) [10, 128]. However, to simulate physically realistic doping efficiencies below 100%, the statistical descriptions require that the dopant's DOS is above that of the host's DOS. As the doping mechanism between ZnPc:F_6-TCNNQ is reported as integer-charge transfer [81, 128], the position of E_A

cannot be explained with reference to hybridised antibonding states [85, 130]. Instead, it is proposed that the dopant's energy level shifts above that of the hosts as a consequence of the electrostatic interactions in the mixed films, in accordance with recent calculations [196]. For F_8ZnPc in a mixed film with ZnPc, the IE shifts by 0.86 eV relative to a F_8ZnPc pristine film [10].

A similar shift places the dopant's acceptor level from 0.40 eV below ZnPc (the difference between their pristine IE and EA) to 0.46 eV above the centre of the ZnPc DOS. With the disorder described by a standard deviation σ around 160-180 meV, as measured for $ZnPc:F_6$-TCNNQ by UPS measurements [81], this value for the dopant's acceptor level is in close agreement with our statistical description.

Temperature dependence

Finally, as a further validation our model, EPR measurements are performed at low temperature $T = 80$ K. In Figure 5.13, the low temperature experimental results fit the statistical model well, with E_A and σ kept constant. The doping efficiency decreases at lower temperature because fewer holes possess the required thermal energy to bridge the gap between the host and dopant energy levels. Overall, considering quadrupole interactions between host and dopant thus yields a consistent picture of the doping process in the $ZnPc:F_6$-TCNNQ system.

5.4 Conclusion

To conclude, the long-range Coloumb interactions, that enable the continuous tuning of effective energy levels, profoundly effect the doping process in organic semiconductors. The role of energy levels in the doping process is investigated using a ternary blend system comprised of hosts ZnPc and F_8ZnPc and dopant F_6-TCNNQ. Through PDS and EPR measurements, a non-linear increase in the doping efficiency is demonstrated from (1.3 ± 0.2) % to (31.9 ± 5.7) % as the content of ZnPc in the blend ratio of $ZnPc:F_8ZnPc$ increases. The neutrality equation is numerically solved for the ternary system to find that the trend of the experimental data is reproduced only by
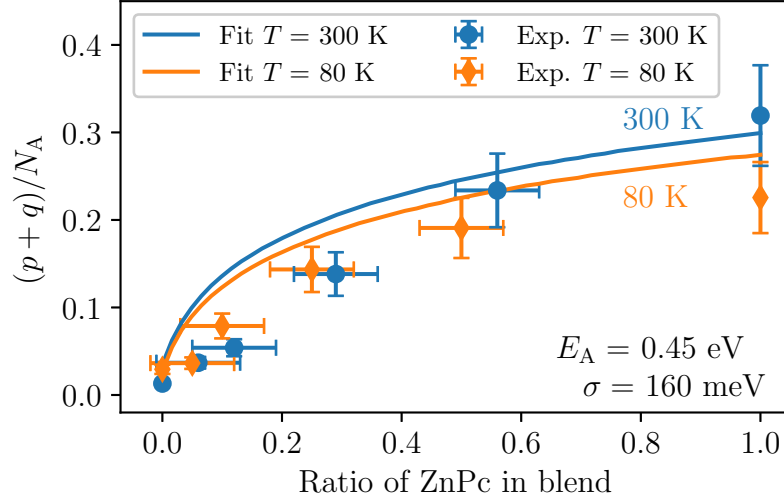
Figure 5.13: Statistical model comparison to EPR with temperature variation. Comparison of experimentally-determined doping efficiency and the statistical model at temperatures $T = 80\,\text{K}$ and $300\,\text{K}$. The model parameters are kept constant at $E_A = 0.45\,\text{eV}$ and $\sigma = 160\,\text{meV}$

considering a shift in the dopant's acceptor level. This shift is attributed to the effect of charge-quadrupole interactions between the hosts and dopant molecules. The simplified picture of selecting hosts and dopants with favourable energy-level offset, as dictated by measurements or calculations of their IE and EA in pristine films, must be extended to include electrostatic effects arising in mixed films, and explains why some host-dopant combinations with unfavourable offset still show the doping effect. Future dopant design should consider the quadrupole moments of both the dopant molecule itself, and the host in which it is to be employed, as important molecular parameters, such that doping efficiency and device performance can be maximised. Finally, it is proposed that ternary blends of organic semiconductors with energy levels subject to the electrostatic shifts observed here, allow for simultaneous control of the molecular energy levels and Fermi level, paving the way for improved performance of organic optoelectronic devices.

6. Summary and outlook

6.1 Summary

This thesis investigated two main topics: the energy level tuning effects in OFETs, and the effect of energy levels on molecular doping. The study of energy level tuning in OFETs began with devices of the pristine materials of ZnPc, F_4ZnPc, F_8ZnPc and F_{16}ZnPc. OFETs of ZnPc and F_4ZnPc showed p-type behaviour, whilst F_8ZnPc and F_{16}ZnPc demonstrated n-type behaviour. The charge carrier mobility in the films tended to decrease with increasing fluorination, which can be partly attributed to changes in morphology, as shown by GIWAXS experiments, and to contact resistances at the source and drain electrodes. Next, OFETs based on blends of ZnPc:F_8ZnPc were fabricated and found to have semiconducting behaviour that could be tuned continuously from unipolar p-type, to ambipolar, and finally to unipolar n-type depending on the blend ratio. At a 1:1.5 weight ratio, ambipolar transistors, with balanced hole and electron mobility, were realised. With the ambipolar devices, a voltage inverter circuit was built with a threshold voltage and gain comparable to an inverter based on separate ZnPc and F_8ZnPc OFETs.

In the second part of this thesis, the p-dopant F_6-TCNNQ was introduced into the blend of ZnPc:F_8ZnPc, with the aim of investigating the role of energy levels on the doping mechanism. The three organic semiconductors were co-evaporated, to fabricate thin films at a fixed doping concentration but with the ratio of the host semiconductors ZnPc:F_8ZnPc varying. The doping efficiency in this ternary blend system was experimentally measured using photothermal deflection spectroscopy, which could resolve peaks characteristic of the ionised dopant, and electron paramagnetic resonance spectroscopy, which allowed for quantitative analysis of the number of charge

carriers residing on the host semiconductors. Through these experimental measurements, a non-linear increase in the doping efficiency was observed, from $(1.3 \pm 0.2)\,\%$ to $(31.9 \pm 5.7)\,\%$ as the content of ZnPc in the blend ratio of ZnPc:F_8ZnPc increased. By numerically solving the neutrality equation for the ternary system, it was found that the trend of the experimental data is reproduced only by considering a shift in the dopant's acceptor level. This shift of $0.86\,\text{eV}$ was found to be in agreement with recent literature pointing toward the role of quadrupole interactions in molecular semiconductors. Overall, considering quadrupole interactions between host and dopant thus yielded a consistent picture of the doping process in the ZnPc:F_6-TCNNQ system.

6.2   Outlook

The first experimental part of this thesis showed that organic electronic devices can benefit from energy level engineering, mediated via the quadrupole interactions. Here, balanced hole and electron mobility in ambipolar field effect transistors was achieved, and subsequently, complementary-like voltage inverters were built. Further logic gates (e.g. AND and OR) could be demonstrated using the same principles with blends of ZnPc:F_8ZnPc, allowing for the fabrication of more complex integrated organic circuits requiring the deposition of only one semiconductor. Additionally, the OFET mobility of the blended devices should be optimised. Several possible routes for improvement include: trying surface treatments or self-assembled monolayers to decrease trapping along the semiconductor-dielectric interface, patterning the semiconductor on OFET chips to avoid fringe currents, and depositing the semiconductor with the substrate held at higher temperature. Finally, it should be noted that the energy level tuning effect is not limited to ZnPc:F_8ZnPc. Other molecular systems have reported similar behaviour, thus could be used for ambipolar OFET and complementary-like logic fabrication.

The second experimental part demonstrated that the energy level tuning effects extend to molecular doping of organic semiconductors. This has implications for

dopant design and, more fundamentally, the way that host and dopants are paired. The prevailing method for pairing hosts and dopants compares their relative ionisation energy and electron affinity, as measured or calculated in pristine films. However, the energy levels in the mixed thin film shift as a consequence of electrostatic interactions and must be accounted for, to achieve efficient doping. Dopant design must consider the quadrupole moments of the host in which it is to be employed, as an important molecular parameters. As a final word, the ternary blend of organic semiconductors with energy levels subject to the electrostatic shifts observed here, allow for control of both the molecular energy levels and Fermi level, which paves the way for improved performance of organic optoelectronic devices.

Bibliography

1. Würfel, U., Cuevas, A. & Würfel, P. Charge carrier separation in solar cells. *IEEE Journal of Photovoltaics* **5,** 461–469 (2014).

2. Liu, C., Xu, Y. & Noh, Y.-Y. Contact engineering in organic field-effect transistors. *Materials Today* **18,** 79–96. doi:10.1016/j.mattod.2014.08.037 (2015).

3. Bredas, J.-L. Mind the gap! *Mater. Horiz.* **1,** 17–19. doi:10.1039/C3MH00098B (2014).

4. Okutsu, S., Onikubo, T., Tamano, M. & Enokida, T. Molecular design of hole transport material with various ionization potential for organic light-emitting diode applications. *IEEE Transactions on Electron Devices* **44,** 1302–1306. doi:10.1109/16.605472 (1997).

5. Duhm, S. *et al.* Orientation-dependent ionization energies and interface dipoles in ordered molecular assemblies. *Nature Mater* **7,** 326–332. doi:10.1038/nmat2119 (2008).

6. Salzmann, I. *et al.* Tuning the Ionization Energy of Organic Semiconductor Films: The Role of Intramolecular Polar Bonds. *J. Am. Chem. Soc.* **130,** 12870–12871. doi:10.1021/ja804793a (2008).

7. Graham, K. R. *et al.* The Roles of Structural Order and Intermolecular Interactions in Determining Ionization Energies and Charge-Transfer State Energies in Organic Semiconductors. *Adv. Energy Mater.* **6,** 1601211. doi:10.1002/aenm.201601211 (2016).

8. Jiang, H. *et al.* Tuning of the degree of charge transfer and the electronic properties in organic binary compounds by crystal engineering: a perspective. *J. Mater. Chem. C* **6,** 1884–1902. doi:10.1039/C7TC04982J (2018).

9. Sahoo, S. R., Sahu, S. & Sharma, S. Charge transport and prototypical optical absorptions in functionalized zinc phthalocyanine compounds: A density functional study. *Journal of Physical Organic Chemistry* **31,** e3785. doi:10.1002/poc.3785 (2018).

10. Schwarze, M. *et al.* Band structure engineering in organic semiconductors. *Science* **352,** 1446–1449. doi:10.1126/science.aaf0590 (2016).

11. Bag, S., Friederich, P., Kondov, I. & Wenzel, W. Concentration dependent energy levels shifts in donor-acceptor mixtures due to intermolecular electrostatic interaction. *Sci Rep* **9,** 12424. doi:10.1038/s41598-019-48877-9 (2019).

12. Schwarze, M. *et al.* Impact of molecular quadrupole moments on the energy levels at organic heterojunctions. *Nat Commun* **10,** 2466. doi:10.1038/s41467-019-10435-2 (2019).

13. Maennig, B. *et al.* Organic p-i-n solar cells. *Appl. Phys. A* **79,** 1–14. doi:10.1007/s00339-003-2494-9 (2004).

14. Blochwitz, J., Pfeiffer, M., Fritz, T. & Leo, K. Low voltage organic light emitting diodes featuring doped phthalocyanine as hole transport material. *Appl. Phys. Lett.* **73,** 729–731. doi:10.1063/1.121982 (1998).

15. Liu, Y. *et al.* High Electron Affinity Molecular Dopant CN6-CP for Efficient Organic Light-Emitting Diodes. *ACS Appl. Mater. Interfaces* **11,** 11660–11666. doi:10.1021/acsami.8b21865 (2019).

16. Walzer, K., Maennig, B., Pfeiffer, M. & Leo, K. Highly Efficient Organic Devices Based on Electrically Doped Transport Layers. *Chem. Rev.* **107,** 1233–1271. doi:10.1021/cr050156n (2007).

17. Lüssem, B. *et al.* Doped Organic Transistors. *Chem. Rev.* **116,** 13714–13751. doi:10.1021/acs.chemrev.6b00329 (2016).

18. Lüssem, B., Riede, M. & Leo, K. Doping of organic semiconductors. *Phys. Status Solidi A* **210,** 9–43. doi:10.1002/pssa.201228310 (2013).

19. Moulé, A. & Meerholz, K. Minimizing optical losses in bulk heterojunction polymer solar cells. *Appl. Phys. B* **86,** 721–727. doi:10.1007/s00340-006-2542-1 (2007).

20. Riede, M., Mueller, T., Tress, W., Schueppel, R. & Leo, K. Small-molecule solar cells—status and perspectives. *Nanotechnology* **19,** 424001. doi:10.1088/0957-4484/19/42/424001 (2008).

21. Maennig, B. *et al.* Controlled p-type doping of polycrystalline and amorphous organic layers: Self-consistent description of conductivity and field-effect mobility by a microscopic percolation model. *Physical Review B* **64,** 195208. doi:10.1103/PhysRevB.64.195208 (2001).

22. Köhler, A. & Bässler, H. *Electronic processes in organic semiconductors: An introduction* (John Wiley & Sons, 2015).

23. Zhang, Y., de Boer, B. & Blom, P. W. M. Controllable Molecular Doping and Charge Transport in Solution-Processed Polymer Semiconducting Layers. *Adv. Funct. Mater.* **19,** 1901–1905. doi:10.1002/adfm.200801761 (2009).

24. Krebs, F. C. Fabrication and processing of polymer solar cells: A review of printing and coating techniques. *Solar Energy Materials and Solar Cells* **93,** 394–412. doi:10.1016/j.solmat.2008.10.004 (2009).

25. Kahn, A. Fermi level, work function and vacuum level. *Mater. Horiz.* **3,** 7–10. doi:10.1039/C5MH00160A (2016).

26. Costa, J. C., Taveira, R. J., Lima, C. F., Mendes, A. & Santos, L. M. Optical band gaps of organic semiconductor materials. *Optical Materials* **58,** 51–60. doi:10.1016/j.optmat.2016.03.041 (2016).

27. Koopmans, T. Über die Zuordnung von Wellenfunktionen und Eigenwerten zu den einzelnen Elektronen eines Atoms. *Physica* **1,** 104–113 (1934).

28. Isaacs, E. B., Sharifzadeh, S., Ma, B. & Neaton, J. B. Relating Trends in First-Principles Electronic Structure and Open-Circuit Voltage in Organic Photovoltaics. *J. Phys. Chem. Lett.* **2,** 2531–2537. doi:`10.1021/jz201148k` (2011).

29. Sato, N., Seki, K. & Inokuchi, H. Polarization energies of organic solids determined by ultraviolet photoelectron spectroscopy. *J. Chem. Soc., Faraday Trans. 2* **77,** 1621. doi:`10.1039/f29817701621` (1981).

30. Chen, W. *et al.* Molecular Orientation-Dependent Ionization Potential of Organic Thin Films. *Chem. Mater.* **20,** 7017–7021. doi:`10.1021/cm8016352` (2008).

31. Maitland, G. C., Rigby, M., Smith, E. B. & Wakeham, W. A. *Intermolecular forces: their origin and determination* (Clarendon Press Oxford, 1981).

32. Heimel, G., Salzmann, I., Duhm, S. & Koch, N. Design of Organic Semiconductors from Molecular Electrostatics. *Chem. Mater.* **23,** 359–377. doi:`10.1021/cm1021257` (2011).

33. Yoshida, H., Yamada, K., Tsutsumi, J. & Sato, N. Complete description of ionization energy and electron affinity in organic solids: Determining contributions from electronic polarization, energy band dispersion, and molecular orientation. *Phys. Rev. B* **92,** 075145. doi:`10.1103/PhysRevB.92.075145` (2015).

34. D'Avino, G. *et al.* Electrostatic phenomena in organic semiconductors: fundamentals and implications for photovoltaics. *J. Phys.: Condens. Matter* **28,** 433002. doi:`10.1088/0953-8984/28/43/433002` (2016).

35. Poelking, C. *et al.* Impact of mesoscale order on open-circuit voltage in organic solar cells. *Nature Mater* **14,** 434–439. doi:`10.1038/nmat4167` (2015).

36. Topham, B. J. & Soos, Z. G. Ionization in organic thin films: Electrostatic potential, electronic polarization, and dopants in pentacene films. *Phys. Rev. B* **84,** 165405. doi:`10.1103/PhysRevB.84.165405` (2011).

37. Bounds, P. & Munn, R. Polarization energy of a localized charge in a molecular crystal. *Chemical Physics* **44,** 103–112 (1979).

38. Benduhn, J. *et al.* Intrinsic non-radiative voltage losses in fullerene-based organic solar cells. *Nat Energy* **2,** 17053. doi:`10.1038/nenergy.2017.53` (2017).

39. Arkhipov, V. I., Heremans, P., Emelianova, E. V. & Bässler, H. Effect of doping on the density-of-states distribution and carrier hopping in disordered organic semiconductors. *Phys. Rev. B* **71,** 045214. doi:`10.1103/PhysRevB.71.045214` (2005).

40. Noriega, R. *et al.* A general relationship between disorder, aggregation and charge transport in conjugated polymers. *Nature Mater* **12,** 1038–1044. doi:`10.1038/nmat3722` (2013).

41. Tummala, N. R., Zheng, Z., Aziz, S. G., Coropceanu, V. & Brédas, J.-L. Static and Dynamic Energetic Disorders in the C_{60}, $PC_{61}BM$, C_{70}, and $PC_{71}BM$ Fullerenes. *J. Phys. Chem. Lett.* **6,** 3657–3662. doi:`10.1021/acs.jpclett.5b01709` (2015).

42. Karl, N. *et al.* Fast electronic transport in organic molecular solids? *Journal of Vacuum Science & Technology A: Vacuum, Surfaces, and Films* **17,** 2318–2328. doi:`10.1116/1.581767` (1999).

43. Karl, N. Charge carrier transport in organic semiconductors. *Synthetic Metals* **133-134,** 649–657. doi:`10.1016/S0379-6779(02)00398-3` (2003).

44. Nelson, J. *Molecular optoelectronic processes: Topic 2: Charge transfer* PE-CDT Lecture Series 2015. Imperial College London, 2015.

45. Marcus, R. A. On the theory of oxidation-reduction reactions involving electron transfer. I. *The Journal of Chemical Physics* **24,** 966–978 (1956).

46. Marcus, R. A. Electron transfer reactions in chemistry. Theory and experiment. *Rev. Mod. Phys.* **65,** 599–610. doi:`10.1103/RevModPhys.65.599` (1993).

47. Gelinck, G., Heremans, P., Nomoto, K. & Anthopoulos, T. D. Organic transistors in optical displays and microelectronic applications. *Advanced materials* **22,** 3778–3798 (2010).

48. Kokil, A., Yang, K. & Kumar, J. Techniques for characterization of charge carrier mobility in organic semiconductors. *Journal of polymer science part b: polymer physics* **50,** 1130–1144 (2012).

49. Tiwari, S. & Greenham, N. Charge mobility measurement techniques in organic semiconductors. *Optical and quantum electronics* **41,** 69–89 (2009).

50. Bao, Z., Lovinger, A. J. & Dodabalapur, A. Organic field-effect transistors with high mobility based on copper phthalocyanine. *Appl. Phys. Lett.* **69,** 3066–3068. doi:`10.1063/1.116841` (1996).

51. Blakesley, J. C. *et al.* Towards reliable charge-mobility benchmark measurements for organic semiconductors. *Organic Electronics* **15,** 1263–1272. doi:`10.1016/j.orgel.2014.02.008` (2014).

52. Tress, W. in *Organic Solar Cells* 67–214 (Springer, 2014).

53. Nelson, J. *The physics of solar cells* (World Scientific Publishing Company, 2003).

54. Salzmann, I., Heimel, G., Oehzelt, M., Winkler, S. & Koch, N. Molecular Electrical Doping of Organic Semiconductors: Fundamental Mechanisms and Emerging Dopant Design Rules. *Acc. Chem. Res.* **49,** 370–378. doi:`10.1021/acs.accounts.5b00438` (2016).

55. Naab, B. D. *et al.* Mechanistic Study on the Solution-Phase n-Doping of 1,3-Dimethyl- 2-aryl-2,3-dihydro-1H-benzoimidazole Derivatives. *J. Am. Chem. Soc.,* 8 (2013).

56. Tietze, M. L. *et al.* Passivation of Molecular n-Doping: Exploring the Limits of Air Stability. *Adv. Funct. Mater.*, 8 (2016).

57. Schwarze, M. *et al.* Analyzing the n-Doping Mechanism of an Air-Stable Small-Molecule Precursor. *ACS Appl. Mater. Interfaces,* 7 (2018).

58. Akamatu, H., Inokuchi, H. & Matsunaga, Y. Electrical conductivity of the perylene–bromine complex. *Nature* **173,** 168 (1954).

59. Curry, J. & Cassidy, E. P. Effect of Halogens on the Resistance of Single Crystals of Copper Phthalocyanine. *The Journal of Chemical Physics* **37,** 2154–2155. doi:10.1063/1.1733442 (1962).

60. Petersen, J. L., Schramm, C. S., Stojakovic, D. R., Hoffman, B. M. & Marks, T. J. A new class of highly conductive molecular solids: the partially oxidized phthalocyanines. *Journal of the American Chemical Society,* 3 (1977).

61. Orr, W. A. & Dahlberg, S. C. Effect of iodine incorporation on the electrical conductivity of films of nickel phthalocyanine. *J. Am. Chem. Soc.* **101,** 2875–2877. doi:10.1021/ja00505a012 (1979).

62. Lee, J.-H., Leem, D.-S. & Kim, J.-J. High performance top-emitting organic light-emitting diodes with copper iodide-doped hole injection layer. *Organic Electronics* **9,** 805–808. doi:10.1016/j.orgel.2008.05.011 (2008).

63. Endo, J., Matsumoto, T. & Kido, J. Organic Electroluminescent Devices with a Vacuum-Deposited Lewis-Acid-Doped Hole-Injecting Layer. *Jpn. J. Appl. Phys.* **41,** L358–L360. doi:10.1143/JJAP.41.L358 (Part 2, No. 3B 2002).

64. Kröger, M. *et al.* P-type doping of organic wide band gap materials by transition metal oxides: A case-study on Molybdenum trioxide. *Organic Electronics* **10,** 932–938. doi:10.1016/j.orgel.2009.05.007 (2009).

65. Chang, C.-C., Hsieh, M.-T., Chen, J.-F., Hwang, S.-W. & Chen, C. H. Highly power efficient organic light-emitting diodes with a p-doping layer. *Appl. Phys. Lett.* **89,** 253504. doi:10.1063/1.2405856 (2006).

66. Yamamoto, Y., Yoshino, K. & Inuishi, Y. Electrical properties of phthalocyanine-halogen complexes. *Journal of the Physical Society of Japan* **47,** 1887–1891 (1979).

67. Olthof, S., Tress, W., Meerheim, R., Lüssem, B. & Leo, K. Photoelectron spectroscopy study of systematically varied doping concentrations in an organic semiconductor layer using a molecular p-dopant. *Journal of Applied Physics* **106,** 103711. doi:10.1063/1.3259436 (2009).

68. Kido, J. & Matsumoto, T. Bright organic electroluminescent devices having a metal-doped electron-injecting layer. *Appl. Phys. Lett.* **73,** 2866–2868. doi:10.1063/1.122612 (1998).

69. Dibb, G. F. A. *et al.* Influence of doping on charge carrier collection in normal and inverted geometry polymer:fullerene solar cells. *Sci Rep* **3,** 3335. doi:10.1038/srep03335 (2013).

70. Deledalle, F. *et al.* Understanding the Effect of Unintentional Doping on Transport Optimization and Analysis in Efficient Organic Bulk-Heterojunction Solar Cells. *Phys. Rev. X* **5,** 011032. doi:`10.1103/PhysRevX.5.011032` (2015).

71. Gao, W. & Kahn, A. Controlled p-doping of zinc phthalocyanine by coevaporation with tetrafluorotetracyanoquinodimethane: A direct and inverse photoemission study. *Appl. Phys. Lett.* **79,** 4040–4042. doi:`10.1063/1.1424067` (2001).

72. Meerheim, R. *et al.* Investigation of C60F36 as low-volatility p-dopant in organic optoelectronic devices. *Journal of Applied Physics* **109,** 103102. doi:`10.1063/1.3590142` (2011).

73. Li, J. *et al.* Measurement of Small Molecular Dopant F4TCNQ and C60F36 Diffusion in Organic Bilayer Architectures. *ACS Appl. Mater. Interfaces* **7,** 28420–28428. doi:`10.1021/acsami.5b09216` (2015).

74. Koech, P. K. *et al.* Synthesis and Application of 1,3,4,5,7,8--Hexafluorotetracyanonaphthoquinodimethane (F6-TNAP): A Conductivity Dopant for Organic Light-Emitting Devices. *Chem. Mater.* **22,** 3926–3932. doi:`10.1021/cm1002737` (2010).

75. Zhang, F. & Kahn, A. Investigation of the High Electron Affinity Molecular Dopant F6-TCNNQ for Hole-Transport Materials. *Adv. Funct. Mater.* **28,** 1703780. doi:`10.1002/adfm.201703780` (2018).

76. Kiefer, D. *et al.* Double doping of conjugated polymers with monomer molecular dopants. *Nature Mater* **18,** 149–155. doi:`10.1038/s41563-018-0263-6` (2019).

77. Qi, Y. *et al.* Use of a High Electron-Affinity Molybdenum Dithiolene Complex to p-Dope Hole-Transport Layers. *J. Am. Chem. Soc.* **131,** 12530–12531. doi:`10.1021/ja904939g` (2009).

78. Karpov, Y. *et al.* High Conductivity in Molecularly p-Doped Diketopyrrolopyrrole-Based Polymer: The Impact of a High Dopant Strength and Good Structural Order. *Adv. Mater.* **28,** 6003–6010. doi:`10.1002/adma.201506295` (2016).

79. Pingel, P. & Neher, D. Comprehensive picture of p -type doping of P3HT with the molecular acceptor F 4 TCNQ. *Phys. Rev. B* **87,** 115209. doi:`10.1103/PhysRevB.87.115209` (2013).

80. Méndez, H. *et al.* Doping of Organic Semiconductors: Impact of Dopant Strength and Electronic Coupling. *Angew. Chem. Int. Ed.* **52,** 7751–7755. doi:`10.1002/anie.201302396` (2013).

81. Tietze, M. L. *et al.* Elementary steps in electrical doping of organic semiconductors. *Nat Commun* **9,** 1182. doi:`10.1038/s41467-018-03302-z` (2018).

82. Kanai, K. *et al.* Determination of electron affinity of electron accepting molecules. *Appl. Phys. A* **95,** 309–313. doi:`10.1007/s00339-008-5021-1` (2009).

83. Salzmann, I. *et al.* Intermolecular Hybridization Governs Molecular Electrical Doping. *Phys. Rev. Lett.* **108,** 035502. doi:`10.1103/PhysRevLett.108.035502` (2012).

84. Aziz, E. *et al.* Localized Charge Transfer in a Molecularly Doped Conducting Polymer. *Adv. Mater.* **19,** 3257–3260. doi:10.1002/adma.200700926 (2007).

85. Méndez, H. *et al.* Charge-transfer crystallites as molecular electrical dopants. *Nat Commun* **6,** 8560. doi:10.1038/ncomms9560 (2015).

86. Lee, J.-H. *et al.* Homogeneous dispersion of organic p-dopants in an organic semiconductor as an origin of high charge generation efficiency. *Applied Physics Letters* **98,** 81 (2011).

87. Duong, D. T., Wang, C., Antono, E., Toney, M. F. & Salleo, A. The chemical and structural origin of efficient p-type doping in P3HT. *Organic Electronics* **14,** 1330–1336 (2013).

88. Knupfer, M. Exciton binding energies in organic semiconductors. *Applied Physics A* **77.** Publisher: Springer, 623–626. doi:10.1007/s00339-003-2182-9 (2003).

89. Mityashin, A. *et al.* Unraveling the Mechanism of Molecular Doping in Organic Semiconductors. *Adv. Mater.* **24,** 1535–1539. doi:10.1002/adma.201104269 (2012).

90. Arkhipov, V. I., Emelianova, E. V. & Adriaenssens, G. J. Effective transport energy versus the energy of most probable jumps in disordered hopping systems. *Phys. Rev. B* **64,** 125125. doi:10.1103/PhysRevB.64.125125 (2001).

91. Kalb, W. L., Haas, S., Krellner, C., Mathis, T. & Batlogg, B. Trap density of states in small-molecule organic semiconductors: A quantitative comparison of thin-film transistors with single crystals. *Phys. Rev. B* **81,** 155315. doi:10.1103/PhysRevB.81.155315 (2010).

92. Olthof, S. *et al.* Ultralow Doping in Organic Semiconductors: Evidence of Trap Filling. *Phys. Rev. Lett.* **109,** 176601. doi:10.1103/PhysRevLett.109.176601 (2012).

93. Tietze, M. L., Leo, K. & Lüssem, B. Quantification of deep hole-trap filling by molecular p-doping: Dependence on the host material purity. *Organic Electronics* **14,** 2348–2352 (2013).

94. Nicolai, H. T. *et al.* Unification of trap-limited electron transport in semiconducting polymers. *Nature Mater* **11,** 882–887. doi:10.1038/nmat3384 (2012).

95. Hiramoto, M., Kikuchi, M. & Izawa, S. Parts-per-Million-Level Doping Effects in Organic Semiconductor Films and Organic Single Crystals. *Adv. Mater.* **31,** 1801236. doi:10.1002/adma.201801236 (2019).

96. Sze, S. M. & Ng, K. K. *Physics of semiconductor devices* (John wiley & sons, 2006).

97. Streetman, B. G., Banerjee, S., *et al. Solid state electronic devices* (Prentice hall Englewood Cliffs, NJ, 1995).

98. Zhou, L. *et al.* All-organic active matrix flexible display. *Appl. Phys. Lett.* **88,** 083502. doi:10.1063/1.2178213 (2006).

99. Eder, F. *et al.* Organic electronics on paper. *Appl. Phys. Lett.* **84,** 2673–2675. doi:10.1063/1.1690870 (2004).

100. Stallinga, P. *Electrical characterization of organic electronic materials and devices* OCLC: ocn424555633. 303 pp. (John Wiley & Sons, Chichester, U.K, 2009).

101. Choi, H. H., Cho, K., Frisbie, C. D., Sirringhaus, H. & Podzorov, V. Critical assessment of charge mobility extraction in FETs. *Nature Mater* **17,** 2–7. doi:10.1038/nmat5035 (2018).

102. Bürgi, L., Richards, T. J., Friend, R. H. & Sirringhaus, H. Close look at charge carrier injection in polymer field-effect transistors. *Journal of Applied Physics* **94,** 6129–6137. doi:10.1063/1.1613369 (2003).

103. Yasuda, T., Goto, T., Fujita, K. & Tsutsui, T. Ambipolar pentacene field-effect transistors with calcium source-drain electrodes. *Applied Physics Letters* **85.** Publisher: American Institute of Physics, 2098–2100. doi:10.1063/1.1794375 (2004).

104. Stallinga, P. & Gomes, H. Metal contacts in thin-film transistors. *Organic Electronics* **8,** 300–304. doi:10.1016/j.orgel.2006.11.004 (2007).

105. Stallinga, P. & Gomes, H. Modeling electrical characteristics of thin-film field-effect transistors. *Synthetic Metals* **156,** 1305–1315. doi:10.1016/j.synthmet.2006.09.015 (2006).

106. Dinelli, F., Murgia, M., Biscarini, F. & De Leeuw, D. Thermal annealing effects on morphology and electrical response in ultrathin film organic transistors. *Synthetic Metals* **146,** 373–376. doi:10.1016/j.synthmet.2004.08.016 (2004).

107. Luan, S. & Neudeck, G. W. An experimental study of the source/drain parasitic resistance effects in amorphous silicon thin film transistors. *Journal of Applied Physics* **72,** 766–772. doi:10.1063/1.351809 (1992).

108. Klauk, H. *et al.* Contact resistance in organic thin film transistors. *Solid-State Electronics* **47,** 297–301 (2003).

109. Xu, Y. *et al.* Modified transmission-line method for contact resistance extraction in organic field-effect transistors. *Appl. Phys. Lett.* **97,** 063302. doi:10.1063/1.3479476 (2010).

110. Sirringhaus, H. Device Physics of Solution-Processed Organic Field-Effect Transistors. *Adv. Mater.* **17,** 2411–2425. doi:10.1002/adma.200501152 (2005).

111. Lüssem, B. *et al.* Doped organic transistors operating in the inversion and depletion regime. *Nat Commun* **4,** 2775. doi:10.1038/ncomms3775 (2013).

112. Häusermann, R. & Batlogg, B. Gate bias stress in pentacene field-effect-transistors: Charge trapping in the dielectric or semiconductor. *Appl. Phys. Lett.* **99,** 083303. doi:10.1063/1.3628297 (2011).

113. Wang, A., Kymissis, I., Bulovic, V. & Akinwande, A. Engineering density of semiconductor-dielectric interface states to modulate threshold voltage in OFETs. *IEEE Trans. Electron Devices* **53,** 9–13. doi:10.1109/TED.2005.860633 (2006).

114. Horowitz, P. & Hill, W. *The art of electronics* (Cambridge Univ. Press, 1989).

115. Bronner, M., Opitz, A. & Brütting, W. Ambipolar charge carrier transport in organic semiconductor blends of phthalocyanine and fullerene. *phys. stat. sol. (a)* **205,** 549–563. doi:10.1002/pssa.200723405 (2008).

116. Katz, H. E. *et al.* A soluble and air-stable organic semiconductor with high electron mobility. *Nature* **404,** 478–481. doi:10.1038/35006603 (2000).

117. Bao, Z., Lovinger, A. J. & Brown, J. New Air-Stable *n* -Channel Organic Thin Film Transistors. *J. Am. Chem. Soc.* **120,** 207–208. doi:10.1021/ja9727629 (1998).

118. Nénon, S., Kanehira, D., Yoshimoto, N., Fages, F. & Videlot-Ackermann, C. Ambipolar organic field-effect transistors based on CuPc and F16CuPc: Impact of the fine microstructure at organic–organic interface. *Synthetic Metals* **161,** 1915–1920. doi:10.1016/j.synthmet.2011.06.035 (2011).

119. Jiang, H. *et al.* Molecular Crystal Engineering: Tuning Organic Semiconductor from p-type to n-type by Adjusting Their Substitutional Symmetry. *Adv. Mater.,* 10 (2017).

120. Pfuetzner, S. *et al.* The influence of substrate heating on morphology and layer growth in C60:ZnPc bulk heterojunction solar cells. *Organic Electronics* **12,** 435–441. doi:10.1016/j.orgel.2010.12.007 (2011).

121. Tietze, M. L. *et al.* Correlation of open-circuit voltage and energy levels in zinc-phthalocyanine: C 60 bulk heterojunction solar cells with varied mixing ratio. *Phys. Rev. B* **88,** 085119. doi:10.1103/PhysRevB.88.085119 (2013).

122. Sánchez-Diaz, A., Burtone, L., Riede, M. & Palomares, E. Measurements of Efficiency Losses in Blend and Bilayer-Type Zinc Phthalocyanine/C 60 High-Vacuum-Processed Organic Solar Cells. *J. Phys. Chem. C* **116,** 16384–16390. doi:10.1021/jp3054422 (2012).

123. Tress, W., Leo, K. & Riede, M. Dominating recombination mechanisms in organic solar cells based on ZnPc and C 60. *Appl. Phys. Lett.* **102,** 163901. doi:10.1063/1.4802276 (2013).

124. Tietze, M. *Molecular Doping Processes in Organic Semiconductors investigated by Photoelectron Spectroscopy* PhD thesis (Technische Universität Dresden, Dresden, 2014).

125. Maennig, B. *et al.* Controlled p-type doping of polycrystalline and amorphous organic layers: Self-consistent description of conductivity and field-effect mobility by a microscopic percolation model. *Phys. Rev. B* **64,** 195208. doi:10.1103/PhysRevB.64.195208 (2001).

126. Riede, M. *et al.* Efficient Organic Tandem Solar Cells based on Small Molecules. *Adv. Funct. Mater.* **21,** 3019–3028. doi:10.1002/adfm.201002760 (2011).

127. Meiss, J. *et al.* Fluorinated Zinc Phthalocyanine as Donor for Efficient Vacuum-Deposited Organic Solar Cells. *Advanced Functional Materials* **22,** 405–414 (2012).

128. Waas, D., Rückerl, F. & Knupfer, M. Charge Transfer at the Interface Between MnPc and F $_6$ TCNNQ. *Phys. Status Solidi B* **256,** 1800245. doi:10.1002/pssb.201800245 (2019).

129. Brendel, M. *et al.* The Effect of Gradual Fluorination on the Properties of FnZnPc Thin Films and FnZnPc/C60 Bilayer Photovoltaic Cells. *Advanced Functional Materials* **25,** 1565–1573. doi:10.1002/adfm.201404434 (2015).

130. Tietze, M. L., Pahner, P., Schmidt, K., Leo, K. & Lüssem, B. Doped Organic Semiconductors: Trap-Filling, Impurity Saturation, and Reserve Regimes. *Adv. Funct. Mater.* **25,** 2701–2707. doi:10.1002/adfm.201404549 (2015).

131. Schwarze, M. *et al.* Molecular parameters responsible for thermally activated transport in doped organic semiconductors. *Nature Mater* **18,** 242–248. doi:10.1038/s41563-018-0277-0 (2019).

132. Menke, T. *Molecular Doping of Organic Semiconductors - A Conductivity and Seebeck Study* PhD thesis (Technische Universität Dresden, 2013).

133. Sauerbrey, G. Verwendung von Schwingquarzen zur Wägung dünner Schichten und zur Mikrowägung. *Zeitschrift für physik* **155,** 206–222 (1959).

134. Warren, R. *Keithley-2636* https://github.com/AFMD/keithley-2636.

135. Rivnay, J., Mannsfeld, S. C. B., Miller, C. E., Salleo, A. & Toney, M. F. Quantitative Determination of Organic Semiconductor Microstructure from the Molecular to Device Scale. *Chem. Rev.* **112,** 5488–5519. doi:10.1021/cr3001109 (2012).

136. Nicklin, C. *et al.* MINERVA: A facility to study Microstructure and INterface Evolution in Realtime under VAcuum. *Review of Scientific Instruments* **88,** 103901. doi:10.1063/1.4989761 (2017).

137. Filik, J. *et al.* Processing two-dimensional X-ray diffraction and small-angle scattering data in ıt DAWN 2. *Journal of Applied Crystallography* **50,** 959–966. doi:10.1107/S1600576717004708 (2017).

138. Privitera, A. *Development and Characterization of Nanaostructured Materials for Organic and Hybrid Solar Cells* PhD thesis (Universita degli Studi di Padova, 2018).

139. Stoll, S. & Schweiger, A. EasySpin, a comprehensive software package for spectral simulation and analysis in EPR. *Journal of magnetic resonance* **178,** 42–55 (2006).

140. *Advanced characterization techniques for thin film solar cells* (eds Abou-Ras, D., Kirchartz, T. & Rau, U.) 2nd, extended edition (Wiley-VCH Verlag, Weinheim, 2016).

141. Frisch, M. J. *et al.* Gaussian 09, Revision D. 01, Gaussian. *Inc.: Wallingford, CT* (2009).

142. Becke, A. D. Density-functional thermochemistry. III. The role of exact exchange. *The Journal of Chemical Physics* **98,** 5648–5652. doi:`10.1063/1.464913` (1993).

143. Becke, A. D. Density-functional exchange-energy approximation with correct asymptotic behavior. *Phys. Rev. A* **38,** 3098–3100. doi:`10.1103/PhysRevA.38.3098` (1988).

144. Vosko, S. H., Wilk, L. & Nusair, M. Accurate spin-dependent electron liquid correlation energies for local spin density calculations: a critical analysis. *Canadian Journal of physics* **58,** 1200–1211 (1980).

145. Stephens, P. J., Devlin, F., Chabalowski, C. & Frisch, M. J. Ab initio calculation of vibrational absorption and circular dichroism spectra using density functional force fields. *The Journal of physical chemistry* **98,** 11623–11627 (1994).

146. Krishnan, R., Binkley, J. S., Seeger, R. & Pople, J. A. Self-consistent molecular orbital methods. XX. A basis set for correlated wave functions. *The Journal of Chemical Physics* **72,** 650–654 (1980).

147. McLean, A. & Chandler, G. Contracted Gaussian basis sets for molecular calculations. I. Second row atoms, Z= 11–18. *The Journal of Chemical Physics* **72,** 5639–5648 (1980).

148. Warren, R. *Statistical Doping Model* `https://github.com/AFMD/dopingModel`.

149. Bai, R.-R. *et al.* Donor Halogenation Effects on Electronic Structures and Electron Process Rates of Donor/C $_{60}$ Heterojunction Interface: A Theoretical Study on F $_n$ ZnPc (¡i¿n¡/i¿ = 0, 4, 8, 16) and Cl ¡i¿ $_n$ ¡/i¿ SubPc (¡i¿n¡/i¿ = 0, 6). *J. Phys. Chem. A* **123,** 4034–4047. doi:`10.1021/acs.jpca.9b01937` (2019).

150. Meijer, E. J. *et al.* Solution-processed ambipolar organic field-effect transistors and inverters. *Nature Mater* **2,** 678–682. doi:`10.1038/nmat978` (2003).

151. Gundlach, D. *et al.* An experimental study of contact effects in organic thin film transistors. *Journal of Applied Physics* **100,** 024509. doi:`10.1063/1.2215132` (2006).

152. Puntambekar, K. P., Pesavento, P. V. & Frisbie, C. D. Surface potential profiling and contact resistance measurements on operating pentacene thin-film transistors by Kelvin probe force microscopy. *Applied Physics Letters* **83,** 5539–5541. doi:`10.1063/1.1637443` (2003).

153. Niu, G., Cressler, J., Mathew, S. & Subbanna, S. A channel resistance derivative method for effective channel length extraction in LDD MOSFETs. *IEEE Trans. Electron Devices* **47,** 648–650. doi:`10.1109/16.824743` (2000).

154. Yuan Taur. MOSFET channel length: extraction and interpretation. *IEEE Trans. Electron Devices* **47,** 160–170. doi:`10.1109/16.817582` (2000).

155. Ng, K. K. & Brews, J. R. Measuring the effective channel length of MOSFETs. *IEEE Circuits and Devices Magazine* **6,** 33–38 (1990).

156. Dimitrakopoulos, C. D. & Malenfant, P. R. Organic thin film transistors for large area electronics. *Advanced materials* **14,** 99–117 (2002).

157. Horowitz, G. & Hajlaoui, M. Grain size dependent mobility in polycrystalline organic field-effect transistors. *Synthetic Metals* **122,** 185–189 (2001).

158. Bolognesi, A. *et al.* Effects of grain boundaries, field-dependent mobility, and interface trap States on the electrical Characteristics of pentacene TFT. *IEEE Transactions on Electron Devices* **51,** 1997–2003. doi:10.1109/TED.2004.838333 (2004).

159. Kim, J. W. *et al.* High performance organic planar heterojunction solar cells by controlling the molecular orientation. *Current Applied Physics* **13,** 7–11. doi:10.1016/j.cap.2012.06.003 (2013).

160. Rivnay, J. *et al.* Large modulation of carrier transport by grain-boundary molecular packing and microstructure in organic thin films. *Nature Mater* **8,** 952–958. doi:10.1038/nmat2570 (2009).

161. Senthilarasu, S., Hahn, Y. B. & Lee, S.-H. Structural analysis of zinc phthalocyanine (ZnPc) thin films: X-ray diffraction study. *Journal of Applied Physics* **102,** 043512. doi:10.1063/1.2771046 (2007).

162. Deng, W.-Q. & Goddard, W. A. Predictions of Hole Mobilities in Oligoacene Organic Semiconductors from Quantum Mechanical Calculations. *J. Phys. Chem. B* **108,** 8614–8621. doi:10.1021/jp0495848 (2004).

163. Hutchison, G. R., Ratner, M. A. & Marks, T. J. Intermolecular Charge Transfer between Heterocyclic Oligomers. Effects of Heteroatom and Molecular Packing on Hopping Transport in Organic Semiconductors. *J. Am. Chem. Soc.* **127,** 16866–16881. doi:10.1021/ja0533996 (2005).

164. Bromley, S. T., Mas-Torrent, M., Hadley, P. & Rovira, C. Importance of intermolecular interactions in assessing hopping mobilities in organic field effect transistors: Pentacene versus dithiophene-tetrathiafulvalene. *Journal of the American Chemical Society* **126.** Publisher: ACS Publications, 6544–6545. doi:10.1021/ja049762a (2004).

165. Stallinga, P., Gomes, H. L., Biscarini, F., Murgia, M. & de Leeuw, D. M. Electronic transport in field-effect transistors of sexithiophene. *Journal of Applied Physics* **96,** 5277–5283. doi:10.1063/1.1789279 (2004).

166. Gu, G., Kane, M. G., Doty, J. E. & Firester, A. H. Electron traps and hysteresis in pentacene-based organic thin-film transistors. *Appl. Phys. Lett.* **87,** 243512. doi:10.1063/1.2146059 (2005).

167. Ucurum, C., Goebel, H., Yildirim, F. A., Bauhofer, W. & Krautschneider, W. Hole trap related hysteresis in pentacene field-effect transistors. *Journal of Applied Physics* **104,** 084501. doi:10.1063/1.2999643 (2008).

168. Egginger, M., Bauer, S., Schwödiauer, R., Neugebauer, H. & Sariciftci, N. S. Current versus gate voltage hysteresis in organic field effect transistors. *Monatsh Chem* **140,** 735–750. doi:10.1007/s00706-009-0149-z (2009).

169. Egginger, M. *et al.* Mobile Ionic Impurities in Poly(vinyl alcohol) Gate Dielectric: Possible Source of the Hysteresis in Organic Field-Effect Transistors. *Adv. Mater.* **20,** 1018–1022. doi:10.1002/adma.200701479 (2008).

170. Salleo, A. & Street, R. A. Light-induced bias stress reversal in polyfluorene thin-film transistors. *Journal of Applied Physics* **94,** 471–479. doi:10.1063/1.1581352 (2003).

171. Smits, E. C. *et al.* Ambipolar charge transport in organic field-effect transistors. *Physical Review B* **73.** Publisher: APS, 205316 (2006).

172. Chung, K., Neudeck, G. & Bare, H. Analytical modeling of the CMOS-like a-Si:H TFT inverter circuit. *IEEE J. Solid-State Circuits* **23,** 566–572. doi:10.1109/4.1023 (1988).

173. Choi, H. H., Cho, K., Frisbie, C. D., Sirringhaus, H. & Podzorov, V. *The measurement reliability factor, r, in FET publications* 2017.

174. Bolognesi, A., Di Carlo, A. & Lugli, P. Influence of carrier mobility and contact barrier height on the electrical characteristics of organic transistors. *Appl. Phys. Lett.* **81,** 4646–4648. doi:10.1063/1.1527983 (2002).

175. Ullah, M. *et al.* Dependence of Meyer–Neldel energy on energetic disorder in organic field effect transistors. *Appl. Phys. Lett.* **96,** 213306. doi:10.1063/1.3435477 (2010).

176. Opitz, A. *et al.* Mixed crystalline films of co-evaporated hydrogen- and fluorine-terminated phthalocyanines and their application in photovoltaic devices. *Organic Electronics* **10,** 1259–1267. doi:10.1016/j.orgel.2009.07.004 (2009).

177. Kawaguchi, H., Taniguchi, M. & Kawai, T. Control of threshold voltage and hysteresis in organic field-effect transistors. *Appl. Phys. Lett.* **94,** 093305. doi:10.1063/1.3095501 (2009).

178. Todescato, F. *et al.* Correlation between Dielectric/Organic Interface Properties and Key Electrical Parameters in PPV-based OFETs. *J. Phys. Chem. B* **112,** 10130–10136. doi:10.1021/jp8012255 (2008).

179. Inoue, Y. *et al.* Organic Thin-Film Transistors with High Electron Mobility Based on Perfluoropentacene. *Jpn. J. Appl. Phys.* **44,** 3663–3668. doi:10.1143/JJAP.44.3663 (2005).

180. Xiao, K., Liu, Y., Yu, G. & Zhu, D. Influence of the substrate temperature during deposition on film characteristics of copper phthalocyanine and field-effect transistor properties. *Appl Phys A* **77,** 367–370. doi:10.1007/s00339-003-2169-6 (2003).

181. Korodi, I. G., Lehmann, D., Hietschold, M. & Zahn, D. R. T. Improving the mobility of CuPc OFETs by varying the preparation conditions. *Appl. Phys. A* **111,** 767–773. doi:10.1007/s00339-013-7678-3 (2013).

182. Padma, N., Sawant, S. N., Sen, S. & Gupta, S. K. *Effect of post deposition annealing on the performance of copper phthalocyanine based organic thin film transistor* in. SOLID STATE PHYSICS: PROCEEDINGS OF THE 57TH DAE SOLID STATE PHYSICS SYMPOSIUM 2012 (Indian Institute of Technology, Bombay, Mumbai, India, 2013), 786–787. doi:10.1063/1.4791273.

183. Goris, L. *et al.* Absorption phenomena in organic thin films for solar cell applications investigated by photothermal deflection spectroscopy. *Journal of Materials Science* **40,** 1413–1418. doi:10.1007/s10853-005-0576-0 (2005).

184. Benson-Smith, J. J. *et al.* Formation of a Ground-State Charge-Transfer Complex in Polyfluorene//[6,6]-Phenyl-C61 Butyric Acid Methyl Ester (PCBM) Blend Films and Its Role in the Function of Polymer/PCBM Solar Cells. *Advanced Functional Materials* **17,** 451–457. doi:10.1002/adfm.200600484 (2007).

185. Nyokong, T., Gasyna, Z. & Stillman, M. J. Phthalocyanine .pi.-cation-radical species: photochemical and electrochemical preparation of [ZnPc(-1).+ in solution. *Inorg. Chem.* **26,** 548–553. doi:10.1021/ic00251a012 (1987).

186. Niklas, J. & Poluektov, O. G. Charge transfer processes in OPV materials as revealed by EPR spectroscopy. *Advanced Energy Materials* **7,** 1602226 (2017).

187. Schaefer, S. *Spin-dependent processes in organic devices* PhD thesis (2010).

188. Sutton, A. L. *et al.* Structural and optical investigations of charge transfer complexes involving the radical anions of TCNQ and F $_4$ TCNQ. *CrystEngComm* **18,** 8906–8914. doi:10.1039/C6CE02015A (2016).

189. Karpov, Y. *et al.* Molecular Doping of a High Mobility -Diketopyrrolopyrrole–Dithienylthieno[3,2- *b*]thiophene Donor–Acceptor Copolymer with F6TCNNQ. *Macromolecules* **50,** 914–926. doi:10.1021/acs.macromol.6b02452 (2017).

190. Schneider, T. *et al.* p-Doping of polystyrene polymers with attached functional side-groups from solution. *J. Mater. Chem. C* **5,** 770–776. doi:10.1039/C6TC02346K (2017).

191. Tietze, M. L., Burtone, L., Riede, M., Lüssem, B. & Leo, K. Fermi level shift and doping efficiency in p -doped small molecule organic semiconductors: A photoelectron spectroscopy and theoretical study. *Phys. Rev. B* **86,** 035320. doi:10.1103/PhysRevB.86.035320 (2012).

192. Yamada, K. *et al.* Impact of the molecular quadrupole moment on ionization energy and electron affinity of organic thin films: Experimental determination of electrostatic potential and electronic polarization energies. *Phys. Rev. B* **97,** 245206. doi:10.1103/PhysRevB.97.245206 (2018).

193. Kleemann, H. *et al.* Structural phase transition in pentacene caused by molecular doping and its effect on charge carrier mobility. *Organic Electronics* **13,** 58–65. doi:10.1016/j.orgel.2011.09.027 (2012).

194. Warren, P. R., Hardigree, J. F. M., Lauritzen, A. E., Nelson, J. & Riede, M. Tuning the ambipolar behaviour of organic field effect transistors via band engineering. *AIP Advances* **9,** 035202. doi:10.1063/1.5080505 (2019).

195. Li, P., Ingram, G., Lee, J.-J., Zhao, Y. & Lu, Z.-H. Energy disorder and energy level alignment between host and dopant in organic semiconductors. *Communications Physics* **2,** 2 (2019).

196. Li, J. *et al.* Host dependence of the electron affinity of molecular dopants. *Mater. Horiz.* **6,** 107–114. doi:10.1039/C8MH00921J (2019).